UNIVERSITY OF CALIFORNIA

Los Angeles

Water Quality Mitigation Strategy Analysis of the Salton Sea, California Using the Delft-3D Modeling Suite

A dissertation submitted in partial satisfaction of the requirements for the degree Doctor of Philosophy in Civil Engineering

by

Meng-Chen Lee

2021

ABSTRACT OF THE DISSERTATION

Water Quality Mitigation Strategy Analysis of the

Salton Sea, California

Using the Delft-3D Modeling Suite

by

Meng-Chen Lee

Doctor of Philosophy in Civil Engineering

University of California, Los Angeles, 2021

Professor Michael K. Stenstrom, Chair

The Salton Sea is the largest lake in California and is an endorheic, shallow, hypersaline lake. The surface water elevation of the Sea is currently 238 feet below sea level, and has been maintained by agricultural return flows from Imperial Valley farming, and two rivers- the New River and Alamo River- which originate in Mexicali, Mexico. The current salinity is at 74 ppt and is expected to increase due to the Quantification Settlement Agreement that was signed in 2003, stipulating the transfer of 500,000 acre-ft of Colorado River water to urban areas until 2075. This results in less flow to the Salton Sea and the declining water level has exposed 220 square miles of dried up playa, creating dust storms that have become the highest risk factor for asthma and cardiovascular diseases to the population around the Sea. Massive fish and bird kills

began in the 1980s and continue to occur periodically. The Sea that was once the main Pacific flyway is now named as “IBA in Danger” by BirdLife International.

In this study, the Delft3D numerical modeling suite- FLOW, WAVE and WAQ- was utilized to investigate transport and cycling of nutrients under the influence of wind-induced sediment resuspension activity. The three-dimensional hydrodynamic and water quality combined model was applied to simulate mitigation scenarios to assess long-term effects on salinity and water quality of 1) emerged islands, 2) seawater import/export, and 3) seawater import/export in addition to treating tributary rivers to remove nutrients treatment.

Overall, this study supports the findings from previous studies and showed that sediment resuspension is an important factor that influences orthophosphate concentration in the water column, and that emerged islands have long term potential on enhancing burial activity for pollutants removal in the Salton Sea. Furthermore, the seawater import/export mitigation scenario showed promising results of reducing salinity level from 46 ppt to 38-39 ppt in two years. The three-dimensional hydrodynamic/water quality model developed in this work is the latest numerical model tailored to the Salton Sea’s system, and has the potential to improve understanding of biogeochemical processes of chemical substances that lead to detrimental effects, and facilitate future restoration plans for the Salton Sea.

The dissertation of Meng-Chen Lee is approved.

Jennifer Ayla Jay

Irwin H. Suffet

Timu Gallien

Mihyun Park

Michael K. Stenstrom, Committee Chair

University of California, Los Angeles

2021

ACKNOWLEDGMENTS

I begin by thanking Dr. Michael Stenstrom for seeing my potentials, giving me trust and leading me into a new realm in which I acquire new skills and find new sense of purpose. To be able to learn from a true scholar and nature enthusiast like Dr. Stenstrom has been and will always be a blessing and a great inspiration. I would like to thank Dr. Gallien for her guidance in the field of numerical hydrodynamic modeling and shedding light on my research study when I most needed. I would also like to thank Dr. Suffet and Dr. Jay for providing critical suggestions that help shape my analysis and broaden my point of views on this massive topic of the Salton Sea. I would like to extend my gratitude to my first employer and former academic advisors from the Department of Microbiology and from the Department of Civil & Environmental Engineering at the University of Iowa and at Carnegie Mellon University. Thank you for the opportunities and trainings you've given me so that I am able to reach to this goal today.

I am full of gratitude and forever indebted to my grandparents and parents, it is your unconditional love, wonderful examples as passionate educators/life-long learners, and your dedication in devoting yourselves into creating a better world, that I no matter how difficult everything seemed and felt like at the moment, always know that I am on the right path, and I can do it.

This journey would be half joyful without my pets, friends, and family. I truly appreciate all the wonderful moments we have shared together; it is you who lift me up and filled my life with laughter. Special appreciation goes to Sandra, Jennifer, Camille, Charlie, Lyla and Walter. It is your companions and support every step of the way that I am able to complete this PhD journey.

Table of Contents

List of Tables

List of Figures

VITA/BIOGRAPHICAL SKETCH

EDUCATION	
Carnegie Mellon University M.S. in Environmental Management and Science	Pittsburgh, PA Summer 2016
The University of Pittsburgh Master of Public Health (M.P.H.) Environmental and Occupational Health	Pittsburgh, PA Spring 2014
The University of Iowa M.S. Environmental Science B.S. Microbiology, minor in Environmental Science	Iowa City, IA Spring 2012 Spring 2010
PROFESSIONAL EXPERIENCE	
Internship Environmental Health and Safety Department (University of Pittsburgh)	Pittsburgh, PA Spring 2014
Student Researcher Department of Occupational and Environmental Health & University of Pittsburgh/The Southwest PA-Environmental Health Project Project title: *Assessing Unconventional Natural Gas Drilling-related Exposures in the Home* Collected indoor air ($PM_{2.5}$, volatile organic compounds, NO_2, ozone) and water sample (methane, ethane, ethylene, metals) in residential houses Conducted survey (demographic/health, stress, and post-sampling questionnaires) to residents who live in the proximity of shale gas drilling sites. Performed statistic data analysis to quantify chemical hazards and evaluate the potential for risks	Pittsburgh, PA Summer 2013
Teaching Assistant Department of Civil and Environmental Engineering (University of Iowa) Course title: *53:154 Environmental Microbiology* Course title: *53:156 Physical-Chemical Process Fundamentals*	Iowa City, IA Fall 2011 Spring 2011/2012
Laboratory Assistant Department of Microbiology (University of Iowa)	Iowa City, IA July 2008- August2010
RESEARCH EXPERIENCE	
Research Assistant Department of Civil and Environmental Engineering (Carnegie Mellon University) Research topic: *The Role of Natural Voltage Gradients in Horizontal Gene Transfer in Marine Microbial Communities*. Utilized adapted MicroPulser to apply a range of voltages to seawater samples which contained marine microbial communities. Utilized molecular methods to detect horizontal gene transfer activities and genetic effects of marine microorganisms.	Fall 2014-Summer 2016 Pittsburgh, PA
Research Assistant Department of Civil and Environmental Engineering (University of Iowa) Research topic: *Lightning Induced Horizontal Gene Transfer among marine microorganisms* Cultured three bacteria species simultaneously in different concentrations of methane and ethene gases to assess interactions between each microorganism. Monitored and analyzed methane, ethene, and vinyl chloride cometabolism activities by two pure culture methane-oxidizing and ethene-oxidizing bacteria.	Fall 2010- Spring 2012 Iowa City, IA
AWARDS	
UCLA Graduate Division Award recipient Fellowship based on academic achievement and promise.	Fall 2017, Winter 2019, Fall 2019 Los Angeles, CA

CHAPTER 1. Introduction

Southeastern of the famous desert resort city-Palm Springs sits the largest inland lake in California, also known as the Salton Sea. The terminal lake's succession has been determined by the change of course of the Colorado River over the past several thousand years, until in 1905, an irrigation canal failure in the Imperial Valley had caused the river to intermittently overflow the Salon Sink for two years, and thus created the waterbody of the modern Salton Sea.

Historically, what existed before the Salton Sea was Lake Cahuilla that was created periodically through flooding and subsequent drying during Holocene when the Colorado River was diverted into the Salton Trough. Lake Cahuilla was one of the largest freshwater lake of the past, 2,000 square miles in size and more than 300 feet in depth. The ancient lake existed since before 1200, and eventually evaporated completely by 1600. The rich soil of the Imperial and lower Coachella Valleys was the built up from river silt in the old lake after long period of deposition (Singer n.d.).

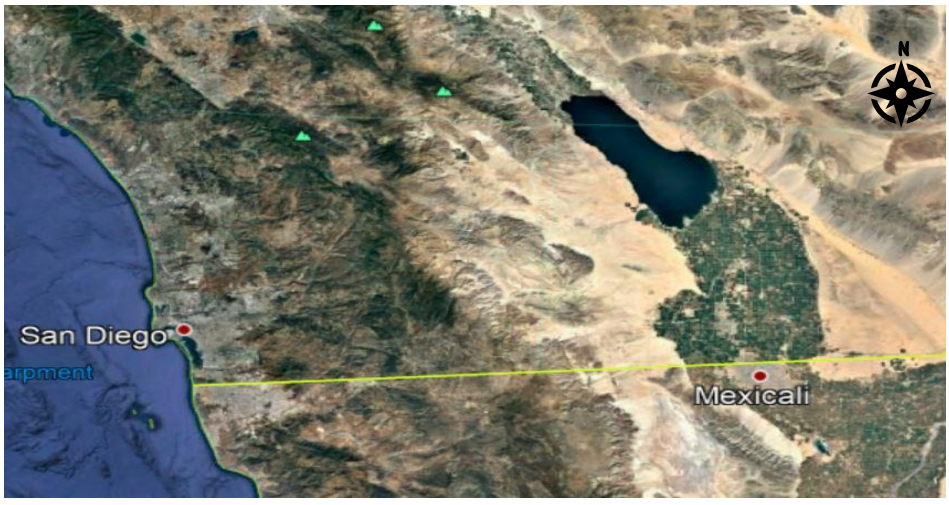

Figure 1. The Salton Sea Transboundary Watershed (photo obtained from Google Earth in December 2005)

The current Salton Sea is an endorheic, shallow, saline lake that is approximately 350 square miles with its surface 236 feet below sea level, and has been maintained not by additional Colorado River flooding, which is now controlled by a series of dams, but by agricultural return flows from Imperial Valley farming, and two small rivers-New River and Alamo River- from the Mexicali (Figure 1).

Massive fish and bird kills began to take place since the 80s due toxic algae contaminations. Moreover, the ecological crisis has exacerbated since the Quantification Settlement Agreement (QSA) was signed in October 2003, stipulating transferring 500,000 afy of agricultural runoff to the City of San Diego. As of 2018, 38.4 % annual reduction of inflow water has led to rapidly falling of Salton Sea's water level, exposing land previously underwater. This new land, called playa, dries up and creates dust storms which affect the health of the population around the Sea.

The Sea is currently endangered by water diversions to urban areas that began in 2018. These waters previously entered the Sea and maintained its level. The level has decreased approximately two feet since 2018 and the salinity has increased from approximately 46 g/L in 2005 to approximately 74 g/L in 2021. It is important to preserve the Sea as a natural resource for several reasons. The Salton Sea has previously functioned as a bird flyway for more 400 species of birds, and has been designated an Audubon Important Bird Area of global significance (Barnum et al. 2017). The increase in salinity has nearly eliminated the Tilapia and its two prey species, Pupfish and Sailfin Mollies which are the main food source for most of the birds that visit the Sea (Little Hoover Commission 2015). Also, the declining level exposes playa which becomes a source of fine dust, and it is believed that the dust periodically transported

off the exposed Salton Sea lakebed is the main reason for Coachella and Imperial County's high asthma and cardiovascular disease rate. The asthma emergency department visit records in 2014 showed that the visiting rate of children in the Imperial County was among the highest in California, and about 1.8 times the state average (California epartment of Public Health n.d.). After numerous severe fish and birds die-offs since the 80s, the Sea now is named as "IBA in Danger" (Important Bird & Biodiversity Area) by BirdLife International. As the results, maintaining the level of the Sea is essential for both purposes.

Previous studies have shown that eutrophication occurs in the Salton Sea was heavily influenced by the internal loading, rather than external loading of phosphorous within the water column, and sediment resuspension caused by wind-induced wave activity is the dominant mechanism for the Salton Sea's nutrient cycling (Chung et al., 2008). In addition, Marti-Cardona et al. (2008) showed that wind-driven upwellings of hypolimnetic water in the Salton Sea during periods of thermal stratification are directly linked to the occurrence of fish kills (Marti-cardona et al. 2008).

The most recent hydrodynamic/water quality simulations of the Salton Sea were conducted a decade ago including, RMA10 (Christopher B. Cook, Orlob, and Huston 2002), Dynamic lake model-water quality, DLM-WQ (Chung et al., 2008, 2009) and three-dimensional numerical model (Si3D) (Rueda et al., 2009). The models were utilized to demonstrate the effects of formerly proposed restoration configurations of the Salton Sea on its nutrient dynamics and stratification. The simulation results showed that nutrient concentration would increase due to higher sediment resuspension events, and the Sea would have stronger stratification for longer periods. However, all models

were developed and calibrated based on only one year of complete temperature and water quality data in 1997. Among which, the water quality simulation was based on one-dimensional assumption that was not built to simulate in salinity higher than 44 ppt (Chung et al., 2008).

In my research study, the Delft3D modeling suite is chosen to be the numerical model for conducting hydrodynamic and water quality/sediment resuspension simulations in the Salton Sea. The three models that are most relevant to my study within the Delta Shell framework include Delft3D-FlOW, Delft3D-Waves and Delft3D-WAQ. Each module has its own conceptual design and numerical implementations; therefore, Delta Shell serves as a mutual interface where multiple modules can be integrated and carry out 3D simulation for non-steady flow and transport phenomena/water quality processes resulting from meteorological forcing.

In early 2000s, two three-dimensional hydrodynamics numerical models (RMA10 and Si3D) were utilized to characterize circulation and thermal stratification of the Salton Sea by Cook et al. (2000) and Rueda et al.(2009), respectively. Chung et al. (2009) made the first attempt combining sediment resuspension models with a process-based, Lagragian layer schemed, one-dimensional hydrodynamic/water quality model (DLM-WQ) to investigate the effect of sediment resuspension on nutrient cycling in the Salton Sea. In the recent ten years, this study made the first attempt to utilize a three-dimensional, numerical hydrodynamic coupled with a water quality model to characterize Salton Sea's hydrodynamic and the effects on the nutrient cycles in the water column and sediment layers. In addition, the model was calibrated and validated using the datasets measured on August 8 to September 17 2005 by Chung et al.

(2009). The validation period of 9/1/2005 to 8/8/2007 is the longest simulation on the hydrodynamics and water quality of the Salton Sea existed so far. The validated models are used to simulate three water quality mitigation scenarios including building emerged islands, seawater import/export canals implementation, and seawater canals construction in addition to treated tributary rivers (90% nutrient reduction).

Overall, this study confirmed that sediment resuspension is the main factor that influence orthophosphate concentration in the water column. Based on this principle, emerged islands that serve to reduce wind-induced bottom shear stress were designed and evaluated. The simulation indicated that the area covered by the emerged islands were shielded from bottom shear stress exceeding above the critical level, which in the long term could enhance burial effects that lead to larger orthophosphate decrease in the water column. Furthermore, the seawater import/export mitigation scenario showed promising results of reducing salinity level from 46 ppt to 38-39 ppt in two years.

1.1Research Objective

Recently an approach of constructing a smaller but sustainable lake concept has emerged. The putative Salton Sea Management Plan would take place around the perimeter of the Sea, where the perimeter lake is surrounded by other projects planned by the State and the Imperial Irrigation District (IID), including geothermal energy development by the Salton Sea Restoration and Renewable Energy Initiative (SSRREI) (Imperial Irrigation District 2015), shallow habitat as an air quality mitigation plan, and other pilot projects such as Red Hill Bay and Species Conservation Habitat (SCH) project (Salton Sea Authority 2016).

Those pilot projects were proposed to solve the immediate issues to cover up approximately one-half of the more than 60,000 acres of dry playa that is projected to be exposed over the next 10 years. However, evaluation has suggested that Salton Sea would shrink and become more saline whether or not the habitats are implemented. As the results, this work aims to provide mitigation strategies on improving the water quality within the water body of the Salton Sea.

Previous research has demonstrated that wind-driven sediment resuspension events are critical in influencing the short-term/seasonal nutrient and phytoplankton concentration variations in the water column. As the results, this thesis research aimed to characterize Salton Sea's hydrodynamic and biogeochemical processes using the Delft3D numerical modeling suite created by Deltares. There are three main objectives of my research: 1) to characterize the effect of nutrients being reintroduced to the euphotic zone by sediment resuspension activity, 2) to investigate the nutrient dynamics affected by reduced wind fetches in the presence of emerged islands in the Sea, and 3) to assess long-term effects of seawater import/export implementation on nutrients/ salinity reduction.

1.2Background

1.2.1 Historical Background

Old time glory of the Salton Sea-fishing and boating mecca

The annual average of monthly precipitation at the Salton Sea is less than 0.5 inches per month. The main water source of the Sea is the agricultural runoff from farms in the Imperial Valley where two rivers run through: The New River and The Alamo River. The only way water leaving the Sea is evaporation. In 1951, local residents brought fish from San Felipe Beach into Salt Creek, an ephemeral creek on the east

side of the Sea, augmenting the fresh-water fish population derived from the original Colorado floods. The fish population once expanded to approximately 200 million but now only Tilapia exist.

In the late 50s, environmental conditions peaked at the Salton Sea and it became a popular spot for millions of migratory birds of more than 400 species. The alluring combination of the desert and the sea had attracted developers, including M. Penn Phillips, to invest in the development of the Salton City for a new concept of Southern California living. The low altitude and the accompanying water density had made Salton Sea's water ideal for beach recreation activities in the middle of a desert. Therefore, a big-time gambler, Ray Ryan spent more than two million dollars on building lavishing resorts: one on the north east side of the sea called North Shore Beach and the Yacht Club in Salton City (Lorey 2002).

Depressed Communities

The local environment started to degrade when the fluctuation of the Sea elevation challenged the lives and businesses reside on the shores of the Salton Sea. In the late 70s consecutive storms in California occurred and flooded the commercial areas. In 2003, the Quantification Settlement Agreement (QSA) stipulated a reduced water allocation in favor of urban usage in San Diego, resulting in a decrease in runoff inputs to the agricultural usage in the Salton Sea Basin. Moreover, the diversion of Colorado River water to the Sea, to mitigate the inflow reductions, had ended at the end of 2017. As more severe decline of water level is expected, and more area of dry playa will be exposed that is highly emissive of particulate matter and particulate toxicity associated with metals and pesticides (Frie et al. 2017) .

Pollution derived from the polluted tributaries: selenium, DDTS, PAHs, insecticides, and diseases

There are two rivers from the south that feed the Salton Sea. The Alamo river is a natural river that originates in Mexicali and is composed of domestic sewage and Colorado River runoff. The New River was recreated with the flood of 1905 and also originates in Mexicali. Both have contained agricultural, chemical, and sewage runoff on the United Sate, Mexico, and Mexicali sides. The Alamo River has been ranked top on the highest organochlorine chemical concentrations in birds and fish by the State of California State Water Resources Control Board. Therefore, the ecosystem at Salton Sea has deteriorated because 75% of the inflow has consisted of the drainage from these two impaired rivers (Xu et al. 2016).

The California's 303(d) lists Salton Sea as impaired waters due to pollution by selenium. The metals consistently above criteria threshold also include copper in water and sediments. Persistent organic contaminants such as dichlorodiphenyltrichloroethane (DDTs), polycyclic aromatic hydrocarbons (PAHs) were found extensively in fish and sediments of the Sea and its two main tributaries. In addition, current-use pyrethroid insecticides and chlorpyrifos were also observed to be causing water and sediment toxicity (Xu et al. 2016).

Furthermore, the consequence of serving as an agricultural sump under high southern California temperature is eutrophication where massive microalgae blooms deteriorate Sea water followed by massive fish die-offs and associated bird kills. Various factors can lead to lethal effects to fish population as summarized by Glenn et al., “deoxygenation of the water column in summer; chilling-injury in winter; infection of fish by *Vibrio spp*.; and parasitism by a dinoflagellate, *Amyloodinium ocellatum* which

attaches to the gills of the fish". Epizootics involving migratory birds at Salton Sea has increased dramatically within the 1990s as more infectious diseases get harbored and spread to birds by the detritus-fish-bird food chain (Glenn et al. 1999). For instance, avian botulism, avian cholera, and avian salmonellosis have reoccurred and continued to kill substantial numbers of birds in spectrum of species (Friend 2002).

Byron et al. (2007) conducted a study regarding the diffusive flux of selenium between lake sediment and overlying water at the Salton Sea. The results have indicated highly saline and anoxic conditions promote the sequestration of selenium in the sediment (Byron and Ohlendorf 2007).

Grebes prey on the fish that consume selenium contaminated pile worms, as the results toxicity of selenium was another suspected factor to cause massive eared grebe die-off on the shore at the Sea in 1992 and 1994. A biologist of the U.S. Fish and Wildlife Services, Bill Radke found out that some of the tissues of the dead birds contained three times more selenium than what he tested of the same species three years earlier. Another biologist, Joseph Skorupa, believed that exposure of above background concentration of selenium would increase bird's susceptibility to diseases (Lorey 2002).

Pollution resulting from inflow water reduction: salinity increase, elevation decline

Salton Sea's salinity levels are directly related to the Sea's surface elevation, and consequently its major aquatic biota. The Sea has served as the Imperial Valley's catch basin since the 1920s, receiving agricultural wastewater that contained various nutrients, pesticides, heavy metals, as well as 5.2 million tons of salt each year (Cohn 2000). The Sea started out as the largest freshwater lake in California, then from the

1940s, the salinity levels has reached to the same as the Pacific Ocean, and exceeded it from the 1960s. Today, the salinity level is 75% more saline than the Pacific Ocean, and is expected to continue to rise (Barnum et al. 2017).

Because of the sale of incoming water rights to the San Diego County Water authority, as well as the termination of the supplemented water due to elimination of mitigation water sanctioned by the QSA, it is projected that by 2023, the elevation will drop to approximately -242 feet (below sea level), the salinity will reach 70 ppt, and Tilapia and its two prey species, Pupfish and Sailfin Mollies will die out (Little Hoover Commission 2015).

1.2.2 Salton Sea's physical chemical characteristics

Thermal, mixing, and oxygen regimes of the Salton Sea, California, 1997-1999

Watts et.al. (2001) investigated mixing, thermal and dissolved oxygen regimes along with meteorological data of the Salton Sea from 1997 to 1999. The monitoring sites included three mid-lake stations (1997-1999), and two near southern shore stations (1999 only). The frequency of monitoring was every two to five weeks. Meteorological data including solar insolation, air temperature, wind speed and direction for 1997-1999 were obtained from four California Irrigation Management Information System (CIMIS) meteorological stations (Station 127,128, 141 and 151) surrounded the Sea (Watts et al., 2001).

Meteorological data showed that Salton Sea region has large seasonal differences in air temperature, solar radiation, and wind speed. The minimum mean air temperature was 13.5^{o}C in January and maximum mean was 33.5^{o}C occurring in summer (June-August). The similar pattern can be seen from solar insolation data with

a maximum occurring one month earlier than the maximum air temperature. On the other hand, the prevailing winds in the Salton Sea basin were from the north (300^{o}-360^{o}), less frequent wind events were from the south (120^{o}-180^{o}), both winds were roughly paralleled to the long axis of the Sea. Within the three years, spring (March-May) consistently had the highest 7-day running mean wind speeds (Watts et al., 2001).

Thermal and mixing regimes

Their study observed that spring 1998 had the higher 7-day running mean wind speeds than occurred in the spring of 1997 and 1999, and that maximum water temperature occurred two months earlier in 1998 (3 July) than in 1997 (9 September) and 1999 (8 August). They deduced that higher wind speeds in 1998 accelerated seawater heating during May-June 1998 by downward mixing of heat into surface waters. Wind-generated turbulence can serve to diminish heat loss via back radiation, and to increase heat gain via conduction. Furthermore, strong and frequent windy events repeatedly break down incipient thermal stratification, delaying the development of anoxia and sulfide accumulation in bottom waters throughout spring. Thermal stratification and anoxia occurred sooner in the year and persisted for longer intervals when spring wind events were infrequent or weak (Watts et al., 2001).

Between the cooling seasons (September to January), the Sea is presumably mixed daily or nearly daily due to convectional circulation driven by conductive and evaporative cooling of surface waters and infrequent windy conditions during winter season (Watts et al., 2001).

Differential mixing

Wind conditions and bathymetry of the northern and southern basins were deduced to cause differential mixing that were accountable for difference in the temperature and dissolved oxygen regimes among stations throughout the Sea. The phenomenon was exclusively apparent on wind drives mixing during the spring and summer. The maximum width of the southern basin is wider (~25 km) than the northern basin (16.5 km), and Southern basin's maximum depth (12 m) is shallower than northern basin's (14 m). Thus, the southern basin has a greater surface area which allows more complete mixing by lower wind speeds that lead to differences between the two basins in their thermal, dissolved oxygen and sulfide dynamics. The discrepancy between the two basins disappears during periods of high wind speeds due to horizontal advection (Watts et al., 2001).

Vertical salinity gradients were created along a 2-8 km wide strip along the shorelines while freshwater from New River and Alamo River flowing counterclockwise along the southeast shoreline to the northeast and the northwest along the eastern shoreline. It is shown that strong winds and current would accelerate mixing but minimize the spatial extent of the salinity gradients, nonetheless, low winds and low current strength allow vertical salinity gradients to extend well out from the delta areas of the two tributaries in the South basin (Watts et al., 2001).

This study stated that mixing of surface and bottom waters such as movement of heat and oxygen are inhibited when salinity gradients arising from the freshwater inflows. Salton Sea has been receiving approximately 48% of its inflows from Alamo River and 36% of its inflows from New River. The discharge points into the Sea are only

12.5 km apart on a ~150 km shoreline. As a result, the impact of inflows on mixing play significant roles in oxygen regimes of the Sea (Watts et al., 2001).

Oxygen regime comparison between 1954-1956 and 1997-1999

Watts et. al. compared dissolved oxygen concentrations in surface (0-1m) and bottom (12 m) monitored in 1997-1999 to the data collected in 1954-1956 by Carpelan. The results showed that dissolved oxygen concentrations were more variable during mid-day 1997-1999; large variation was observed among years and seasons from 1997 to 1999 whereas only small differences were found in 1954-1956. Surface water were well oxygenated in general at all seasons in 1954-1956, however, surface water in 1997-1999 were hypoxic or anoxic at times in August and September. During the cooling season from September to January when the Sea was mixed daily due to convectional circulation, dissolved oxygen concentrations in surface water were in the similar range (4-10 mg/L) all six years (1954-1956, 1997-1999) (Watts et al., 2001).

In bottom waters, hypoxic and anoxic conditions showed distinct discrepancies within 40 years; during 1997-1999, the hypoxia/anoxia condition occurred early in February and persisted for longer periods whereas in 1954-1956, the bottom waters were usually oxic except a few hypoxia or anoxia days from June to August (Watts et al., 2001).

The increase in rates of primary production, biomass production, decomposition, and increase in sulfate concentration/sulfide production since the 50's are likely the reason for variations in dissolved oxygen concentrations in the 90s' (Watts et al., 2001).

Thicker oxic stratum was observed in nearshore waters during warmer season. In addition, the bottom water was either absent or not significant in the water column,

which reducing mixing that tends to reduce oxygen concentrations, and mixing becomes negligible in nearshore surface waters. Nearshore regions then become potential refuge for fish and benthic macroinvertebrates (Watts et al., 2001).

Overall, the Sea is a wind driven system, the frequency, strength, duration, and timing of wind events causes significant variation in lake dynamics in different years. Generally speaking, deoxygenation effects that are created by the combination of anoxia and sulfide would cause abandonment of the lake center by fish and benthic macroinvertebrates during May to September. Massive mortality of fish and plankton have most often occurred during August and September. Effective recolonization of deep sediments by benthic macroinvertebrates usually begins in September when strong and deep convectional circulation begins. In the spring during April and May, after the strong wind started the first injections of hypoxic and sulfide-bearing bottom waters into surface waters, fish start to migrate to nearshore waters. In addition, the deoxygenation events in spring and summer also lead to the occurrence of 'green tides' that are the optical effect of gypsum crystals in the water column, followed by a period of stratification, the odor of sulfide in the air and fish kills (Watts et al., 2001).

1.2.3 Current Situation

The ecosystem at Salton Sea has been deteriorating without any substantial mitigation action plans for more than three decades. It is expected that the rate of Sea level decline and salinity rise will be more rapid as the addition of mitigation water ends in 2017. As part of the QSA, projects to protect the Salton Sea and avoid the problems

of dry playa dust storms were to have been developed. None of these projects progressed very far because of the great recession of 2007.

Currently the “shovel-ready projects*”* being constructing at the north and south ends of the Sea include *water backbone infrastructures, SSMP air quality and habitat projects, CNRA’s Species Conservation Habitat (SCH) Project, Red Hill Bay Project, and Torres-Martinez Wetland project*. Among which, SCH Project is the first major program developed and operated by the California State (The California Natural Resources Agency and The California Department of Fish and Wildlife) following completion of the environmental planning process. Therefore, potential impacts to Salton Sea under the proposed action of Species Conservation Habitat Projects were evaluated and reported in the Final Environmental Impact Statement/Environmental Impact Report in 2013 (California Department of Water Resources 2013). The comparison of current states of the Salton Sea and potential impacts of SCH Project are presented in Table 1.

Table 1.Comparison of Salton Sea's existing conditions and potential future impacts to the Sea by Species Conservation Habitat Project

Parameter	Salton Sea	Species Conservation Project Impacts on Salton Sea
Water Surface Elevation	-236.8 feet, NAVD 1988 As of 6-Sep-2021 Source: USGS10254005 Salton Sea NR Westmoreland,CA	By 2077, the Sea is expected to decline by 27.2 feet relative to 2014 elevation (-231.0 ft.), and it would decline by 28.2 in the presence of SCH Project
Area	208,900 acres (326 sq. miles) Source: SALSA2	By 2077, the Sea's area size is expected to be 141,723 acres, and would be 139,097 in the presence of SCH Project
Volume	5.0 million acre-feet	By 2077, the Sea is expected to have 1.6 million AF storage of water, and 1.5 million AF in the presence of SCH Project
Salinity	74.25 ppt As of 13-Jan-2020 Source: Bureau of Reclamation	By 2077, salinity is expected to reach 272,000 mg/L, and would reach 298,000 mg/L in the presence of SCH Project
Suspended Particulate/Turbidity Impacts	275 mg/L Whole Sea average On 01/14/ 2020	Reduce Salton Sea's turbidity in the long-term unless berm failures in the pond occur (adverse impacts would be short-term)
Selenium	1.18 µg/g Whole Sea bottom average On 01/14/ 2020	Likely temporary (1-2 years) increase (up to 3.5 µg/L) in total selenium load reaching the Sea in the near future from the SCH ponds. Overall, no significant impact to the Sea
Dissolved Oxygen	7.85 mg/L Whole Sea average at the surface on 01/14/ 2020	A direct short-term, localized impact on DO entering the Sea, but less than significant
Nutrients	Ortho-P: <0.1 mg/L Total P: 0.462 mg/L NO3-NO2-N: 0.177mg/L; NH3-N: <1.4 mg/L TKN-N: 4.38 mg/L Whole Sea average On 01/14/ 2020	SCH Project would not contribute additional concentrations of total phosphorous into the Sea

According to the evaluation presented in the Environmental Impact Report (EIR), it is estimated that by 2077, the Sea is expected to decline by 27.2 feet relative to 2014 elevation (-231.0 ft), and it would decline by 28.2 in the presence of SCH Project. Therefore, SCH Project would not have significant direct impacts on the Salton Sea water surface elevation due to the relatively small pond areas. On the other hand, the presence of SCH Project is expected to increase Salton Sea's salinity approximately

9.5% by 2077; the increase is considered less than significant given the fact that the projected salinity increase of Salton Sea under the status quo is already far beyond the recommended salinity. In order words, the Sea would shrink, and become more saline regardless of whether or not the SCH Project is implemented (California Department of Water Resources 2013).

The EIR suggested that should a berm failure occur due to a seismic event, or flood event, the sediment release into the Sea would only increase its turbidity for short-term before it settles to the bottom of the Sea. However, in the long-term under full build-out of the proposed SCH Project, routine operations of the sedimentation basin would remove and dispose the sediment loads from the New River to the Sea (California Department of Water Resources 2013).

It is known that once the water fills up the constructed saline wetlands, sediment resuspension would facilitate solubilization of oxidized selenium in the pond water, causing increase of selenium by approximately 0.9 µg/L in the overlying water (1 meter deep). Previous research has suggested that there are selenium removal pathways such as volatilization or sequestration that naturally occur within the first one to two years in saline wetlands at the Salton Sea. Thus, comparing to the selenium load that comes from New River (up to 10 µg/L in the future) to the Sea, the amount released from the SCH ponds would be less than significant. EIR believes that the proposed SCH Project would not affect the Sea's selenium loading in general (California Department of Water Resources 2013).

Water quality modeling indicated that SCH ponds would also experience anoxia resulting from diurnal algal biomass respiration (near dawn) and seasonal algal bloom

(in spring and fall). Nonetheless, the low DO pond water discharge to the Sea would be offset by aeration occurring at the external cascade ponds, and would only have localized, temporary impact to the Sea. As far as nutrient loading from the SCH ponds, it is expected that total phosphorus discharge into the Sea would exceed the threshold concentration (0.035 mg/L), but the amount would always be lower than that discharges from New River. Therefore, the impact on nutrients from the constructed habitats would be insignificant (California Department of Water Resources 2013).

Finally, the main purpose of the SCH Projects is to create additional habitats specifically designed for piscivorous birds including American white pelican, Caspian tern, and double-crested cormorant. The habitats would provide forage fish/invertebrates when the salinity exceed the tolerance of most fish population in the future, and the islands within the ponds serve as nesting, resting, protection sites. However, it is expected the amount of fish the SCH is capable of providing would be considerably less than that currently provided by the Sea (California Department of Water Resources 2013).

1.2 Organization

This dissertation is consisted of breaking down, building up and the integrated applications of the three individual modules within the Deflt3D modeling suite-FLOW, WAVE, and WAQ. Chapter one is the literature reviews of historic background, physical/chemical characteristics and critical pollutants/emerging risks of the Salton Sea. In chapter two, previous research on Salton Sea's hydrodynamics modeling using various models were reviewed, followed by introducing governing equations of

FLOW/WAVE, data processing for wind field calculation, and sensitivity analysis. Then, the calibration/validation of current velocity and wave heights results were presented. Chapter three follows the same flow as the previous chapter, where critical water quality processes in WAQ module (and BLOOM submodule) were discussed. The chapter was finished by the calibration/validation outputs for sediment concentrations and bottom shear stress. In Chapter four, validation results of important water quality variables (dissolved oxygen, orthophosphate, unionized ammonia, and chlorophyll *a*) were presented. Based on the validations of all three modules, water quality mitigation scenarios were introduced including implementation of emerged islands in the south basin of the Salton Sea, seawater import/export project, and seawater canals implementation with treated tributary rivers. The long-term effects of the status quo and the three mitigation scenarios on critical water quality variables as well as salinity were analyzed and discussed. In chapter five conclusions and future direction suggestions were made.

Chapter 2. Modeling the hydrodynamics of the Salton Sea

2.1 Abstract

Restoration plans for the Salton Sea's ecological values were proposed in the early 2000s, introducing the need for a better understanding of the hydrodynamic behaviors as well as the subsequential water quality impacts of the Sea. There were a few modeling efforts conducted on the Salton Sea from 2000 to 2009 that provided critical observations and preliminary assessments of the potential effects from various restoration configurations and strategies.

The first three-dimensional numerical modeling was conducted by Cook et al. (2000), which successfully resolved a counterclockwise gyre in the southern basin as observed previously and indicated a strong thermal stratification in the northern basin due to relatively weak circulation. The simulation also suggested that using dikes in the southern basin would generate disproportional increased and decreased local velocities around the diked impoundment areas and formed stagnation zones near the river mouths. A one-dimensional, deterministic model that coupled with sediment resuspension formulations were evaluated by Chung et al. (2008, 2009). The year-long simulation showed that the thermocline appeared from late May to late July in 1999 with anoxia near the bottom, while the rest of the time the water column remained unstratified. In addition, the calibrated model indicated that reducing 90% of external tributary phosphorus load only had small effects on short-term effects of chlorophyll *a* concentration and phytoplankton growth. The study demonstrated that internal loading caused by sediment resuspension plays an important role in contributing to the nutrient budget within the Sea. Finally, the importance of wind field estimations on modeling

proficiency was investigated by Rueda et al. (2009) using another three-dimensional free surface hydrodynamic model with roughness/height correction for various wind boundary conditions. The efforts yielded good agreements of stratification evolutions in the lake at the hourly, daily, and seasonal scales, and concluded that more meteorological stations in closer proximity would increase modeling accuracy and that reducing the lake size would induce a stronger and longer stratification.

2.2 Introduction

Previous research has demonstrated that the biogeochemical processes occur within the shallow Salton Sea's system is predominantly driven by wind (Christopher B. Cook, Orlob, and Huston 2002) (Chung et al. 2008) (Chung, Bombardelli, and Schladow 2009b)(Holdren and Montaño 2002). As the results, meteorological fields as boundary conditions are critical to the models that simulate circulation, transport and mixing processes take place in the Salton Sea. What follows are the review of previous studies that demonstrated physical-based models and numerical models on Salton Sea's hydrodynamic and water quality simulations and their applications on impact assessments.

2.2.1 A three-dimensional numerical model on Salton Sea's hydrodynamic characteristics

Cook et al. (2002) utilized a three-dimensional numerical model, RMA10, to construct a hydrodynamic model for the Salton Sea in order to characterize its circulation and thermal stratification behaviors under the status quo and four proposed alternatives configurations. RMA10 solves for a set of partial differential equations

describing continuous momentum equations (advective acceleration, tractive forces, pressure forces, Coriolis acceleration) and equation of state (change of density in the function of temperature and salinity) under dynamic boundary conditions (Christopher B. Cook, Orlob, and Huston 2002).

Meteorological boundary condition data were obtained from six meteorological stations installed by California Irrigation Management Information System (CIMIS) near the proximity of the Salton Sea (CIMIS 50, 136, 127,128, 41 and SSN). Heat budget was estimated based on hourly data of air temperature, relative humidity, and net radiation, and space, and temporal varying wind fields were calculated based on the six stations around the periphery of the Sea (Christopher B. Cook, Orlob, and Huston 2002).

Cook's study showed that in October higher surface winds observed in the south generated a counterclockwise gyre in the southern basin, and increased local velocity magnitudes in near-shore areas. On the other hand, the circulation in the northern basin was less structure and generally weak. In the May simulation, a strong thermal stratification in the northern basin was characterized from May 20-31, 1997, during which a thermocline was formed and persistent without much storm induced disturbance. Conversely, the southern basin was weakly stratified, and experienced intense mixing during the May simulation period. The model was applied to evaluate circulation changes under the conditions created by four proposed diking alternatives. The results showed that north/south ponds and displacement dike in the Delta areas of the two rivers led to disproportional increased and decreased local velocities around the

diked impoundment areas, and large stagnation zones (Christopher B. Cook, Orlob, and Huston 2002).

2.2.2 Sediment resuspension activities in the Salton Sea using a one-dimensional hydrodynamic/water quality model coupled with sediment resuspension formula

Chung et al. (2008 and 2009) made the first attempt combining sediment resuspension models with a one-dimensional hydrodynamic/water quality model (Dynamic lake model-water quality, DLM-WQ) to investigate the effect of sediment resuspension on nutrient cycling in the Salton Sea. DLM-WQ is a process-based, deterministic model based on a Lagrangian layer scheme. Each horizontal layer has homogenous properties, but layer thickness is varied. The hydrodynamic model is mainly driven by surface heat, mass and momentum exchange. The dynamic of mixed layers are modeled by parameterized turbulent kinetic energy model through meteorological based forcings: wind stirring, convective overturn, interfacial shear production, and Kelvin-Helmholtz billowing. Furthermore, Hypolimnion mixing is parametrized by eddy diffusivity that is calculated based on direct proportional to the dissipation of turbulent kinetic energy, and inversely proportional to the strength of stratification (Chung et al. 2008) (Chung, Bombardelli, and Schladow 2009b).

The temperature data from 1997 (Cook, 2000) and the water quality dataset collected by Bureau of Reclamation in 1999 (Holdren and Montaño 2002) was used for calibration/validation tasks. DLM-WQ simulates the temporal and vertical distribution of the following variables: temperature chlorophyll *a*, dissolved oxygen (DO),ortho-phosphate (OP), particulate phosphorus (PP), nitrate (NO_3), ammonium (NH_4), particulate nitrogen (PN), and total suspended solids (TSS). The input data utilized

included: bathymetric, forcings (meteorological, inflow/outflow), stream inflow water quality data, and initial conditions for all the modeled variables (Chung, Bombardelli, and Schladow 2009b)

The meteorological data (solar shortwave radiation, longwave radiation, air temperature, relative humidity, precipitation, wind speed and direction) in year 1999 was solely obtained from site #128 from California Irrigation Management Information System (CIMIS) in both studies done by Chung et al., (2008 and 2009). The wind speed/direction data was measured on the northern west shore of the lake near the Salton City, and was adjusted from 2 m to 10 m using the semi-logarithmic velocity law (Chung et al. 2008) (Chung, Bombardelli, and Schladow 2009b).

The DLM-WQ model simulation was based on the assumptions that sediment resuspension and orthophosphate-P diffusion from the pore water occurred only above the thermocline, and that the resuspension flux for each Lagrangian layer is the same. The phytoplankton was modeled as one functional group (Chung et al. 2008).

The simulated temperature results agreed well with the measured; thermocline appeared from late May and gradually broke down until reaching near-isothermy (>29 ^{o}C) in late July, 1997, and unstratified water column from January to May, and from August to December. The model confirmed the anoxia near the bottom during summer, and presented fairly good fit for seasonal trend of OP concentrations. However, the rapid changes of SS and OP due to sediment resuspensions did not closely matched with the measured probably due to the 2-to 4- week sampling interval (Chung et al. 2008). In the subsequent study in 2009, the DLM-WQ model coupled with the extended relation of Garcia and Parker sediment model produced NH_4 and PN trends and short-

term variations that agreed with the measured values fairly well with few exceptions. It is also observed that measured TSS at the bottom was rather consistent and lied with the bracket values simulated by the model, the author stated that this could resulted from the fact that sampling usually took place during calm days, thus showing under-represented TSS concentrations in general (Chung, Bombardelli, and Schladow 2009b).

The calibrated model was used to simulate scenario of 90% external tributary phosphorus load reduction. The results indicated the short-term effects on chlorophyll *a* concentration and phytoplankton growth was small, and was therefore deduced that internal loading caused by sediment resuspension plays important role in contributing to the nutrient budget within the Sea. In addition, nutrient limiting effects only affect the phytoplankton growth near the surface, below 3 m from the surface was light-limited. The author further stated that reduction in stream phosphorus in the long term shall eventually impact on productivity due to permanent removal of phosphorus-sequestered sediment source by natural sediment burial processes, though the rate at which this might occur is unknown given the limited sediment data of the Salton Sea (Chung et al. 2008).

2.2.3 Wind field variations on Salton Sea's stratification using a three-dimensional model

Rueda et al. (2009) assessed the uncertainties arise from spatially and temporally varying wind fields, and demonstrated that the numerical, three-dimensional model's capacity (Si3D) in simulating stratification in the Salton Sea. The authors summarized three factors that are the cause of wind field uncertainties, including: interpolation methods, number of available stations, and most significantly, the local roughness

correction assumptions at land-based stations (land measured wind needs to be increased to represent wind speed over water).

The momentum of incompressible fluids, the transport of scalars (temperature, salinity etc.) as well as the equation of state calculated in this 3-D numerical model are based on the Reynolds-averaged form of the Navier-Stoke equations. The Si3D model simulates the circulation, transport and mixing processes using the semi-implicit, leapfrog-trapezoidal finite difference scheme on a staggered Cartesian grid (Rueda, Vidal, and Schladow 2009).

The meteorological data used for validation were obtained from three CIMIS stations 127 (west shore), 128 (southeastern) and 136 (north) in the year of 1997 and 1999. CIMIS stations 141 (northeastern) and 154 (north eastern) in the year of 1999 were also obtained in this study. Wind speed and direction measured by CIMIS stations near the Salton Sea were at 2 m above ground level and on bare earth surfaces. Therefore, wind speed values were subjected to two types of corrections: roughness correction and height correction before spatial interpolation take place (Rueda, Vidal, and Schladow 2009). Spatially varying wind fields were interpolated using an exponential distance weighting function developed by Barnes (1964)(Huston 2000) (Christopher B. Cook, Orlob, and Huston 2002).

Statistical analysis of 50 simulations (each with different sets of roughness correction factors for CIMIS 127, 128 and 136 stations) were conducted, and it shewed that the 3D free surface hydrodynamic model with the roughness/height corrected wind boundary conditions generated stratification evolution in the lake at hourly, daily, and seasonal scales reasonably well

Rueda et al. evaluated the effects of a reduced lake (the North Sea scenario) on thermal stratification, and the results indicated that the number of weather stations used to estimate the wind fields are positively associated with the agreement between the observed and simulated data. However, reducing the lake size would induce a stronger and longer stratification no matter how wind fields were reconstructed by different total numbers or different combinations of stations (Rueda, Vidal, and Schladow 2009).

2.3 Governing Equations for Delft3D

The Salton Sea is a shallow, polymictic, and wind driven lake with water temperature ranged from 13 to 14 ^{o}C in winter season to up to 34- 35 ^{o}C during summer. As the results, during the warming period (January to August), thermal stratification was often sporadically interrupted by mixing, especially during windy seasons. During the cooling months from September to January, the Sea is still subject to daily or nearly daily mixing due to conductive and periodic storm events. A unique wind-driven double gyre circulation pattern was observed in the south basin of the Sea. In addition, mixing events were often associated with large fish kills because it extended the anoxic condition in bottom waters to the entire water column for a period of days (Watts et al., 2001). To address the questions derived from this discontinuous warm polymictic shallow lake systems, a three-dimensional hydrodynamic model like Delft3D that is capable of resolving wind-induced seiching, turbulence and vertical mixing under local meteorological forcing is required.

Several studies have demonstrated the validity of Dleft3D FLOW in reproducing flow fields on enclosed lakes around the world. Delft3D-FLOW was utilized to evaluate

climate effects on deep Lake Constance, Germany (473 km^2, mean depth is 100 m) and showed that the 3D hydrodynamic model was reliable so revolve thermal stratification and vertical transport and mixing that agreed well with the observed data for over half a century simulation (Wahl and Peeters 2014). Dissanayake et al. (2019) conducted further investigation of wind-induced internal seiches and surface currents forced by a horizontally resolved wind field on Lake Constance using two 3D hydrodynamic models, the Estuary Lake and Coastal Ocean Model (ELCOM) and Delft3D-FlOW. The study showed that 3D hydrodynamic models that are capable of coupling the lake surface to wind forcing, estimating surface heat flux as well as resolving baroclinic dynamics were skilled at resolving internal wave and surface currents. In addition, wind field imprecisions are significant in influencing deviations between the measured and the simulated current field and stratification (Dissanayake, Hofmann, and Peeters 2019). McCombs el al. (2014) modeled winter wind-wave processes and winter circulation dynamics of the Kingston Basin of Lake Ontario during storm event, and found that the sharp bathymetric features and large velocity gradients would cause highly complex circulation pattern (McCombs et al. 2014). In addition, Delft3D-FLOW have been applied as a management tool in the following lakes that receive excess nutrients and/or organic matter from the agricultural activities and industrial/domestic wastewater discharge in the catchment: Lake Egirdir (Kaçikoç and Beyhan 2014), Taihu Lake (Li, Chen, and Xu 2015).

The formulations described in the following section are derived from the user manual of the Delft3D-FLOW module (Deltares 2014).

2.3.1 The Shallow Water Equations for Hydrostatic Flow

The principle governing equations to describe the momentum and continuity of free-surface hydrostatic flow is derived from the Navier-Stokes equation:

$$\frac{D\vec{u}}{Dt} = \frac{\rho}{\rho_0}\vec{F} - \frac{1}{\rho_0}\nabla p + \nu\nabla^2\vec{u} \tag{2.3.1}$$

where $\vec{u}$ is the velocity vector that contains place vector ($\overrightarrow{x}$) and time component (t) of the fluid element. The right-hand side of the equation are the forces exert on the fluid element in which $\vec{F}$ are the external forces including gravitational and Coriolis acceleration, p is pressure and ν is the molecular kinematic viscosity. Density variations are neglected when $\frac{\Delta\rho}{\rho_0} \ll 1$ based on the Boussinesq approximation, except the density appears in the gravitational acceleration term, reference density (ρ_0) is used in all other terms. The del operator (∇) is defined as the partial derivatives of a vector along each axis, x, y and z.

The elaborated three-dimensional hydrostatic shallow water equations, Reynolds-Averaged Navier-Stokes equations, given in Cartesian orthogonal curvilinear coordinates in the horizontal and σ-coordinates in the vertical are expressed by:

$$\frac{\partial u}{\partial t} + \frac{u}{\sqrt{G\xi\xi}}\frac{\partial u}{\partial \xi} + \frac{v}{\sqrt{G\eta\eta}}\frac{\partial u}{\partial \eta} + \frac{\omega}{d+\zeta}\frac{\partial u}{\partial \sigma} - \frac{v^2}{\sqrt{G\xi\xi}\sqrt{G\eta\eta}}\frac{\partial\sqrt{G\eta\eta}}{\partial \xi} + \frac{uv}{\sqrt{G\xi\xi}\sqrt{G\eta\eta}}\frac{\partial\sqrt{G\xi\xi}}{\partial \eta} - fv =$$

$$-\frac{1}{\rho_0\sqrt{G\xi\xi}}P_\xi + F_\xi + \frac{1}{(d+\zeta)^2}\frac{\partial}{\partial\sigma}\left(\nu_V\frac{\partial u}{\partial\sigma}\right) + M_\xi \tag{2.3.2}$$

$$\frac{\partial v}{\partial t} + \frac{u}{\sqrt{G\xi\xi}}\frac{\partial v}{\partial \xi} + \frac{v}{\sqrt{G\eta\eta}}\frac{\partial v}{\partial \eta} + \frac{\omega}{d+\zeta}\frac{\partial v}{\partial \sigma} - \frac{uv}{\sqrt{G\xi\xi}\sqrt{G\eta\eta}}\frac{\partial\sqrt{G\eta\eta}}{\partial \xi} - \frac{u^2}{\sqrt{G\xi\xi}\sqrt{G\eta\eta}}\frac{\partial\sqrt{G\xi\xi}}{\partial \eta} + fu =$$

$$-\frac{1}{\rho_0\sqrt{G\eta\eta}}P_\eta + F_\eta + \frac{1}{(d+\zeta)^2}\frac{\partial}{\partial\sigma}\left(\nu_V\frac{\partial v}{\partial\sigma}\right) + M_\eta \tag{2.3.3}$$

where ξ and η are horizontal, curvilinear coordinates, and $\sqrt{G\xi\xi}, \sqrt{G\eta\eta}$ are the coefficients for transforming curvilinear to rectangular coordinates. The three-dimensional velocity vector is denoted as u, v and ω. Overall, Equation 2.3.2 and 2.3.3 show the momentum equations in horizontal direction are consisted of convection terms, Reynolds or turbulent stress (uu, uv, u^2, v^2), Coriolis acceleration (fu, fv), pressure gradients (P_ξ, P_η), forces of the unbalance of horizontal Reynold's stresses (F_ξ, F_η), vertical eddy viscosity coefficient (ν_V), and external sources and sinks of momentum (M_ξ, M_η) (e.g. precipitation, evaporation, discharge or withdraw of water etc.).

The shallow water assumption is based on the condition that the depth length is much smaller than the horizontal length scale, and is further elaborated to assume that vertical acceleration is negligible compared to the horizontal ones. This assumption is valid for problems in which vertical dynamics can be neglected compared to horizontal effects. Therefore, the vertical momentum equation become merely the hydrostatic pressure relation ($\frac{dp}{d\sigma} = -\rho g H$), where g is gravitational acceleration and H is water depth. The gravitational acceleration term is not unaffected by the Boussinesq approximation.

$$\omega = \omega + \frac{1}{\sqrt{G\xi\xi}\sqrt{G\eta\eta}}\left[u\sqrt{G\eta\eta}\left(\sigma\frac{\partial H}{\partial \xi} + \frac{\partial \zeta}{\partial \xi}\right) + v\sqrt{G\xi\xi}\left(\sigma\frac{\partial H}{\partial \eta} + \frac{\partial \zeta}{\partial \eta}\right)\right] + \left(\sigma\frac{\partial H}{\partial t} + \frac{\partial \zeta}{\partial t}\right) \quad (2.3.4)$$

Equation 2.3.4 shows that the vertical velocity is expressed in terms of horizontal velocities, water depth (H), free surface above the reference plane (ζ), and ω-vertical velocity associated with up- or downwelling motions on the σ-plane.

2.3.2 The Transport Equations

In Delft3D-FLOW, dissolved substances, salinity and heat transported by the flow in aqueous systems are computed by an advection-diffusion equation in orthogonal curvilinear coordinates shown in Equation 2.3.5:

$$\frac{\partial(d+\zeta)c}{\partial t}+\frac{1}{\sqrt{G\xi\xi}\sqrt{G\eta\eta}}\left\{\frac{\partial\left[\sqrt{G\eta\eta}(d+\zeta)uc\right]}{\partial\xi}+\frac{\partial\left[\sqrt{G\xi\xi}(d+\zeta)vc\right]}{\partial\eta}\right\}+\frac{\partial\omega c}{\partial\sigma}=$$

$$\frac{d+\zeta}{\sqrt{G\xi\xi}\sqrt{G\eta\eta}}\left\{\frac{\partial}{\partial\xi}\left(D_H\frac{\sqrt{G\eta\eta}}{\sqrt{G\xi\xi}}\frac{\partial c}{\partial\xi}\right)+\frac{\partial}{\partial\eta}\left(D_H\frac{\sqrt{G\xi\xi}}{\sqrt{G\eta\eta}}\frac{\partial c}{\partial\eta}\right)\right\}+\frac{1}{(d+\zeta)}\frac{\partial}{\partial\sigma}\left(D_V\frac{\partial c}{\partial\sigma}\right)-\lambda_d(d+\zeta)c+S \qquad (2.3.5)$$

where c is the scalar quantity such as heat or dissolved matter, D_H is the horizontal diffusion coefficient, D_v is the vertical diffusion coefficient, λ_d is the first order decay process and S stands for source and sink terms per unit area.

2.3.3 The Turbulence Closure Models

The mixing effects are incorporated in the model through internal turbulent stress (or Reynolds stress), and is determined by specifying the eddy viscosity based on the following relation proposed by Boussinesq:

$$\tau_{ij}=-\rho\nu_t\left(\frac{\partial u_i}{\partial x_j}+\frac{\partial u_j}{\partial x_i}\right)-\frac{2}{3}\rho k\delta_{ij} \qquad (2.3.6)$$

where τ_{ij} is the Reynolds stresses, ν_t is the eddy viscosity; x_i and x_j = x, y, z ; k is the turbulent kinetic energy per unit mass. The second term on the right-hand side of (Eq. 2.3.6) involves, δ_{ij}, the Kronecker delta, which is usually neglected in large-scale numerical models.

In Delft3D-FLOW, the superposition that computes the horizontal viscosity coefficient (ν_H) reads:

$$\nu_H = \nu_{SGS} + \nu_{3D} + \nu_H^{back} \quad (2.3.7)$$

in which ν_{SGS} is the sub-grid scale horizontal eddy- viscosity that represents the horizontal turbulent motions and forcing that are not solved by coarse horizontal grid. The three-dimensional turbulence is denoted by ν_{3D}, and is computed by a 3D turbulence closure model. ν_H^{back} is the user-defined background horizontal viscosity that entails those motions removed by solving the Reynolds-Averaged shallow water equations.

The vertical eddy viscosity coefficient ν_V is computed by:

$$\nu_V = \nu_{mol} + \max(\nu_{3D} + \nu_V^{back}) \quad (2.3.8)$$

where ν_{mol} is the kinematic viscosity of water, and the user-defined ν_V^{back} accounts for all other forms of unresolved mixing (e.g. vertical mixing induced by shearing and breaking of internal gravity waves).

In the second-order turbulence closure model, $k-\varepsilon$ model, the turbulent energy (k) and dissipation (ε) are both calculated by transport equations under two assumptions: 1) the equation is dominated by production, buoyancy, and dissipation terms, and 2) the horizonal length scales are larger than vertical length scales. Therefore, the non-conservation form of the transport equation reads:

$$\frac{\partial k}{\partial t} + \frac{u}{\sqrt{G\xi\xi}}\frac{\partial k}{\partial \xi} + \frac{v}{\sqrt{G\eta\eta}}\frac{\partial k}{\partial \eta} + \frac{\omega}{d+\zeta}\frac{\partial k}{\partial \sigma} = \frac{1}{(d+\zeta)^2}\frac{\partial}{\partial \sigma}\left(D_k\frac{\partial k}{\partial \sigma}\right) + P_k + P_{k\omega} + B_k - \varepsilon \quad (2.3.9)$$

$$\frac{\partial \varepsilon}{\partial t} + \frac{u}{\sqrt{G\xi\xi}}\frac{\partial \varepsilon}{\partial \xi} + \frac{v}{\sqrt{G\eta\eta}}\frac{\partial \varepsilon}{\partial \eta} + \frac{\omega}{d+\zeta}\frac{\partial \varepsilon}{\partial \sigma} = \frac{1}{(d+\zeta)^2}\frac{\partial}{\partial \sigma}\left(D_\varepsilon\frac{\partial \varepsilon}{\partial \sigma}\right) + P_\varepsilon + P_{\varepsilon\omega} + B_\varepsilon - c_{2\varepsilon}\frac{\varepsilon^2}{k} \quad (2.3.10)$$

in which D_k, D_ε are eddy diffusivity for the turbulent kinetic energy and energy dissipation, that are defined by:

$$D_k = \frac{\nu_{mol}}{\sigma_{mol}} + \frac{\nu_{3D}}{\sigma_k} \text{ and } D_\varepsilon = \frac{\nu_{3D}}{\sigma_\varepsilon} \quad (2.3.11)$$

The production term for kinetic energy (P_k) and (B_k) are expressed in terms of ν_{3D},vertical gradients of horizontal velocity, and calibration constants ($c_{1\varepsilon}$, $c_{3\varepsilon}$) are used to calculate (P_ε) and (B_ε) from (P_k) and (B_k), respectively.

Wave induced turbulence mainly comes from two sources: wave breaking and bottom friction due to the oscillatory wave motion, and are computed by equation (2.3.12) and equation (2.3.13):

$$P_{k\omega}(z') = \frac{4D_\omega}{\rho_\omega H_{rms}}\left(1 - \frac{2z'}{H_{rms}}\right) \quad for \quad 0 \le z' \le \frac{1}{2}H_{rms} \quad (2.3.12)$$

$$P_{k\omega}(z') = \frac{2D_f}{\rho_0 \delta}\left(1 - \frac{d+\zeta-z'}{\delta}\right) \quad for \quad d + \zeta - \delta \le z' \le d + \zeta \quad (2.3.13)$$

In the turbulent kinetic energy distribution, the total depth-averaged of wave energy (D_w) is linearly distributed over a below mean water surface half wave height ($H_{rms}/2$) (Eq. 2.3.12). On the other hand, the mixing due to bottom friction (D_f) is linearly distributed over the thickness of the wave boundary later (δ) (Eq.2.3.13). The vertical distribution of turbulent kinetic energy due to wave actions is on the z' vertical co-ordinates ranging from below mean water level and above wave boundary layer thickness.

Overall, the vertical eddy viscosity, ν_{3D}, is computed by:

$$\nu_{3D} = c_\mu \frac{k^2}{\varepsilon} \quad (2.3.14)$$

where $c_\mu$is a calibration constant associated with mixing length.

2.3.4 Boundary Conditions

Flow boundary conditions-vertical boundary

Bed boundary conditions

The boundary conditions at the bottom of the waterbody (σ= -1) for the vertical momentum is prescribed by vertical eddy viscosity, (ν_V), water depth (H), and horizontal velocities (*u*,*v*) as shown in equation 2.3.15 and 2.3.16:

$$\left.\frac{\nu_V}{H}\frac{\partial u}{\partial \sigma}\right|_{\sigma=-1} = \frac{1}{\rho_0}\tau_{b\xi} \tag{2.3.15}$$

$$\left.\frac{\nu_V}{H}\frac{\partial v}{\partial \sigma}\right|_{\sigma=-1} = \frac{1}{\rho_0}\tau_{b\eta} \tag{2.3.16}$$

where *u* and *v* component is expressed by bed stress (τ_b) in ξ-, η- direction and reference density (ρ_0), respectively.

In 3D implementation the bottom boundary layer is consisted of combined wave-current bed shear-stress, and is corrected for the Stokes drift (i.e. the wave induced drift velocity):

$$\vec{\tau}_b = \frac{|\overrightarrow{\tau_m}|}{\overrightarrow{U_{2D}}}(\vec{u} - \vec{u}^S) \tag{2.3.17}$$

where $|\overrightarrow{\tau_m}|$ denotes the magnitude of mean bed stress for combined waves and current, and the magnitude of the depth-averaged horizontal velocity, $\left|\overrightarrow{U_{2D}}\right|$, is given by:

$$\vec{U}_{2D} = \frac{1}{d+\zeta}\int_{-d}^{\zeta}\vec{u}\,dz \tag{2.3.18}$$

in which *u* is horizontal velocity, (d+ ζ) is total water depth, and z is vertical co-ordinate. The mean bed stress for combined waves and current is defined in Equation 2.3.19:

$$\vec{\tau}_m = \rho_0\vec{\tilde{u}}_*\left|\vec{\tilde{u}}_*\right| \tag{2.3.19}$$

where $\overrightarrow{\tilde{u}_*}$ is friction (shear-stress) velocity due to current and waves and Stoke drift in ξ-direction, and can be expressed in the horizontal velocity in the first layer just above the bed ($\overrightarrow{u_b}$) and bed roughness height (z_0):

$$\vec{u}_b = \frac{\vec{u}_*}{\kappa} ln\left(1 + \frac{\Delta z_b}{2z_0}\right) \quad (2.3.20)$$

in which, Δz_b is the distance to the computational grid point closest to the bed.

Surface boundary conditions

The boundary conditions at the free surface (σ= 0) for the vertical momentum equations are shown in Equations 2.3.21 and 2.3.22:

$$\frac{\nu_V}{H}\frac{\partial u}{\partial \sigma}\Big|_{\sigma=0} = \frac{1}{\rho_0}|\vec{\tau}_s|\cos(\theta) \quad (2.3.21)$$

$$\frac{\nu_V}{H}\frac{\partial v}{\partial \sigma}\Big|_{\sigma=0} = \frac{1}{\rho_0}|\vec{\tau}_s|\sin(\theta) \quad (2.3.22)$$

where wind shear stress (τ_s) vector, and θ is the constant angle formed by τ_s and the local direction of the grid-line η.

The magnitude of wind shear stress can be computed by Equation 2.3.23:

$$|\vec{\tau}_s| = \rho_a C_d U_{10}^2 \quad (2.3.23)$$

where ρ_a denotes air density, C_d is the wind drag coefficient (U_{10} dependent), and U_{10} is the wind speed at 10 m above the free surface.

Water-water boundary- total discharge

The type of boundary condition chosen is discharge rate from the tributary rivers- Alamo, New and Whitewater River, where the flow is assumed to be perpendicular to the open boundary as time-series. In the vertical direction, the velocity profile is a logarithmic function over the water depth.

The total discharge boundary condition at each time step distributed over the active points of the open boundary is derived from the Chezy equation:

$$q_i = \frac{B_i h_i^{1.5} C_i}{\sum_{j=1}^{N} B_j h_j^{1.5} C_j} Q \quad (2.3.24)$$

where the total discharge (Q) is modified by the ratio of width (B*i*), water depth (h*i*), and roughness (C*i*) of grid cell *i* to the sum of those at each boundary points.

The flow conditions are prescribed as daily total discharge across the cross-section of the river at the entry points.

Transport boundary conditions

The constituents in rivers that are horizontally transported with the flow in the open boundary include dissolved substances, salinity, temperature, and sediment. The transport equation is dominated by advection term shown in Equation 2.3.5, while diffusion terms are of secondary importance. Constituents concentrations at each time breakpoints are specified at both ends of the cross-section river boundary. In this study, the vertical profile of the concentration at the boundary section is prescribed as *uniform* where homogeneous condition is assumed in the whole water depth at the river boundaries.

Vertical boundary conditions for the transport equation

Except for the heat exchange, the vertical diffusive flux of the constituents through the free surface and bed is zero as shown in the Equations 2.3.25 and 2.3.26.

$$\frac{D_V}{H}\frac{\partial c}{\partial \sigma}\Big|_{\sigma=0} = 0 \tag{2.3.25}$$

$$\frac{D_V}{H}\frac{\partial c}{\partial \sigma}\Big|_{\sigma=-1} = 0 \tag{2.3.26}$$

2.3.5 Delft3D-WAVE

The physical processes for wave formation that SWAN (Simulating Waves Nearshore) model solves include the following: 1) wave propagation/ transformation, 2) wave generation by wind, 3) wave dissipation (whitecapping, bottom friction, depth-induced breaking),4) non-linear wave-wave interaction, 5) wave propagation through obstacles, and 6) wave-induced set-up. The formulations described in the following section are derived from the user manual of the Delft3D-WAVE module (Deltares 2019).

The two-dimensional wave action density spectrum that is described by spectral action balance equation is derived from linear wave theory in SWAN:

$$\frac{\partial}{\partial t}N + \frac{\partial}{\partial x}c_x N + \frac{\partial}{\partial y}c_y N + \frac{\partial}{\partial \sigma}c_\sigma N + \frac{\partial}{\partial \theta}c_\theta N = \frac{S}{\sigma} \quad (2.3.27)$$

The left-hand side of Equation 2.3.27 is consisted of wave propagation in time and geographical space, frequency shifting due to currents and non-stationary depth, and depth/current-induced refraction. The source term on the right hand can be denoted as such:

$$S_{tot} = S_{in} + S_{nl3} + S_{nl4} + S_{ds,\omega} + S_{ds,b} + S_{ds,br} \quad (2.3.28)$$

The terms represent the effects of wind-induced waves (S_{in}), three-and four-wave interaction (S_{nl3},S_{nl4}), wave dissipation due to whitecapping ($S_{ds,w}$), bottom friction ($S_{ds,b}$), and depth-induced wave breaking ($S_{ds,br}$) respectively.

Wave generation by wind

Wave growth induced by wind energy is described by the sum of linear growth (A) and exponential growth (BE) term of a wave component:

$$S_{in}(\sigma,\theta) = A + BE(\sigma,\theta) \quad (2.3.29)$$

in which A and B depend on wave frequency in spectral σ-,θ-space, and wind speed (at 10 m elevation), phase speed, and density of air and water (equation not shown).

Whitecapping

The expression of whitecapping process in SWAN is based on a pulse-based model of Hasselmann (1974), and is primarily determined by the steepness of the wave:

$$S_{ds,\omega}(\sigma,\theta) = -\Gamma\tilde{\sigma}\frac{k}{\tilde{k}}E(\sigma,\theta) \quad (2.3.30)$$

where Γ denotes a steepness dependent coefficient, $\tilde{\sigma}$, $\tilde{\kappa}$ are mean frequency and mean wave number, and E is wave energy respectively. In addition, the value of Γ depends on the tunable coefficients (Cds),δ and p that are relevant to the wind input formulation selection (equation not shown).

Bottom friction

The relative strength of wave-bottom interaction is dominated by the bottom friction models, and can be generally described with a conventional bottom friction formulation as such:

$$S_{ds,b}(\sigma,\theta) = -C_{bottom}\frac{\sigma^2}{g^2\sin h^2(kd)}E(\sigma,\theta) \quad (2.3.31)$$

where C_{bottom} denotes a bottom friction coefficient that depends on the bottom orbital motion, and *d* is local water depth. This formulation in SWAN is the simplest form of each of the following three types of friction models: the empirical JONSWAP model of Hasselmann et al. (1973), the drag law model of Collins (1972), and the eddy-viscosity model of Madsen et al. (1988).

Depth-induced wave breaking

The bore-based model of Battjes and Janssen (1978) has been expanded by Eldeberky and Battjes (1995) to a spectral direction version for expressing the energy dissipation in random waves due to wave breaking as shown in Equation 2.3.32:

$$S_{ds,b}(\sigma,\theta) = D_{tot}\frac{E(\sigma,\theta)}{E_{tot}} \quad (2.3.32)$$

in which E_{tot} is the total wave energy, and D_{tot} is the rate of dissipation of the total energy that depends on the breaker parameter (equation not shown).

Quadruplet wave-wave interactions

One of the two methods used for the quadruplet wave-wave interactions at deep water in SWAN is discrete interaction approximation (DIA). The source term computed by DIA proposed by Hasselmann (1985) is as shown:

$$S_{nl4}(\sigma,\theta) = S^{*}_{nl4}(\sigma,\theta) + S^{**}_{nl4}(\sigma,\theta) \quad (2.3.33)$$

where S^{*}_{nl4} is the first quadruplet and S^{**}_{nl4} is the second quadruplet.

$$S^{*}_{nl4}(\sigma,\theta) = 2\delta S^{*}_{nl4}(\alpha_1,\sigma,\theta) - \delta S^{**}_{nl4}(\alpha_2,\sigma,\theta) - \delta S^{**}_{nl4}(\alpha_3,\sigma,\theta) \quad (2.3.34)$$

in which $\alpha_1=1$, $\alpha_2= (1+\lambda)$ and $\alpha_3= (1- \lambda)$, and λ is a constant coefficient.

Triad wave-wave interactions

The triad wave-wave interaction in SWAN is computed by the Lumped Triad Approximation (LTA) method proposed by Eldeberky and Battjes (1996) as shown:

$$S_{nl3}(\sigma,\theta) = S^{-}_{nl3}(\sigma,\theta) + S^{+}_{nl3}(\sigma,\theta) \quad (2.3.35)$$

2.4 Methods

2.4.1 Data Collection

Meteorological Stations

The meteorological information in the Salton Sea area were provided by the following four stations, California Irrigation Management Information Systems (CIMIS 136 and CIMIS 181), Union Pacific Railroad (UP614), and Jet Propulsion Laboratory (SS1). The four stations were selected based on their closest proximity (within 5 miles) to the Salton Sea, and are all currently active (Fig.2). Among which, SS1 station is the

only station where the meteorological data were measured on the water surface of the Sea. Data obtained were from the year 2015 to 2019 from each station.

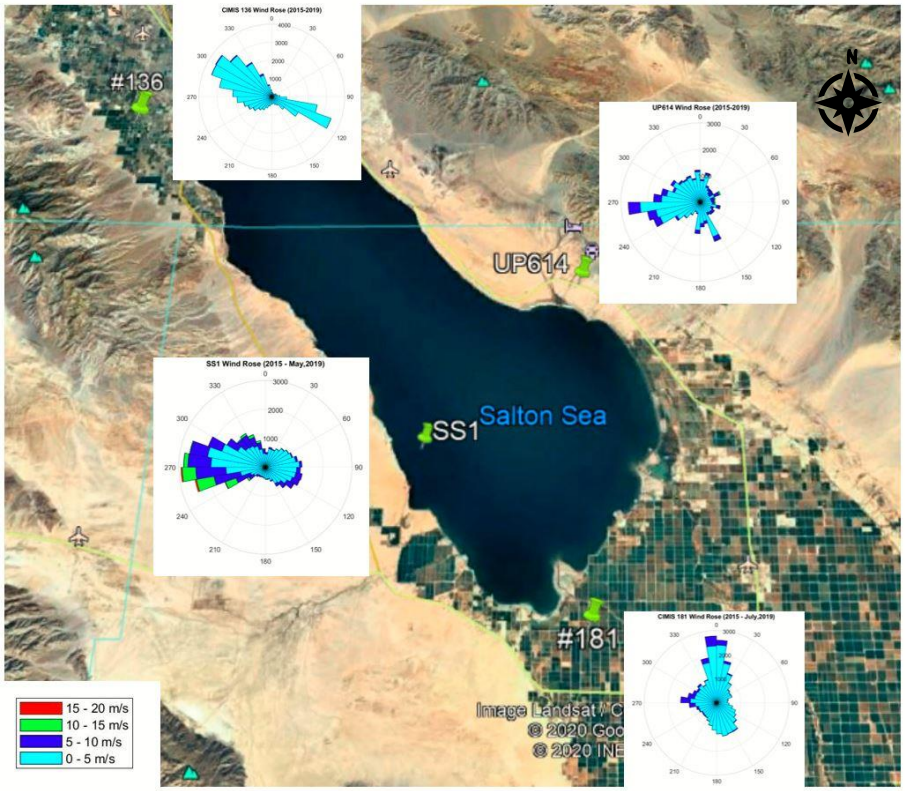

Figure 2. Four meteorological stations around the Salton Sea and the period of records (2015-2019) that are analyzed in this study.

CIMIS provided hourly averaged meteorological data, including evapotranspiration, precipitation, solar radiation, vapor pressure, air temperature, relative humidity, dew point temperature, soil temperature, wind speed, and wind direction. CIMIS 136 (33°31'58.80"N, 116° 9'0.00"W) is located in Thermal, CA, on the north end of the Sea. CIMIS 181 (33° 4'58.80"N, 115°40'1.20"W) is located in Westmoreland, CA, on the south end of the Sea.

Jet Propulsion Laboratory provided hourly averaged meteorological data, such as wind speed, wind direction, air temperature, relative humidity, and pressure. SS1 (33°13'31.15"N, 115°49'27.30"W) instrument is situated on a platform about half a mile off the southwestern coast near the Salton City.

Union Pacific Railroad stations collected hourly averaged data for wind speed, wind direction, and air temperature. UP614 (33°22'18.14"N, 115°40'36.05"W) is located near Bombay Beach, in Frink, CA, on the east shore of the Sea.

2.4.2 Wind Speed Correction

Roughness correction

CIMIS stations are land-based stations, and the wind data were measured at 2 m above ground level on the dry surface in the typical rural southern California land with a surface roughness (z_{0L}) (Tayor and Lee 1984). Therefore, the original land-based wind speed records (U_{2L}) need to be increased to represent wind measured at 2 m over a water surface (U_{2W}) by multiplying by a fixed factor for roughness correction, then further modified to represent wind speed over water at 10 m (U_{10W}) for height correction (Rueda, Vidal, and Schladow 2009).

There are two types of correction factor, f_{OFF} and f_{ON}, depending on whether the wind flows offshore or onshore (Table 2). According to the wind rose diagram for stations CIMIS 136 and 181 (Fig. 3 and Fig.4), it was shown that in the average of five years, offshore wind was blown from mostly the direction from 210^o to 360^o, while onshore wind from 100^o to 150^o at station CIMIS 136. As for station CIMIS 181, offshore wind was blown from mostly the direction from 120^o to 210^o, and onshore wind from

300^{o} to 30^{o} degrees. For station located in the east coast (UP614), onshore wind was blown in the direction from 150^{o} to 300^{o}, the rest of the wind was offshore wind (Fig.5).

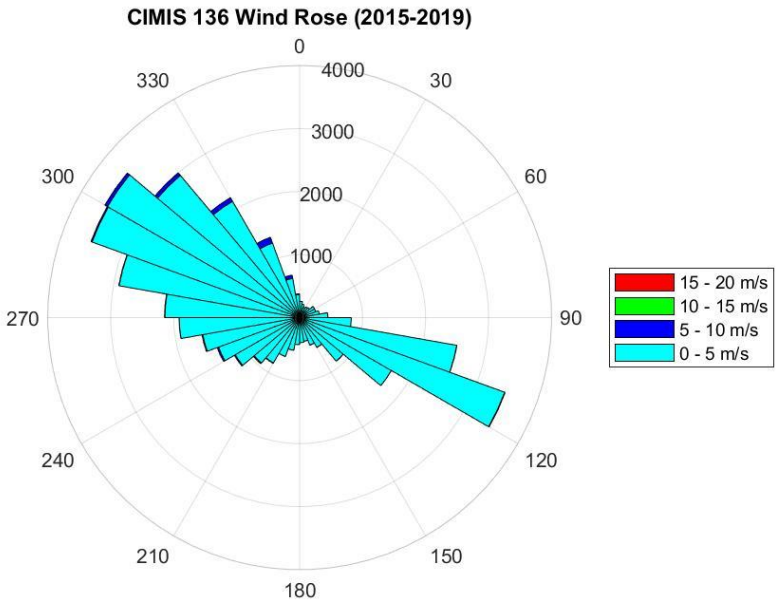

Figure 3. Wind rose diagram for original averaged wind data at station CIMIS 136 (2015-2019)

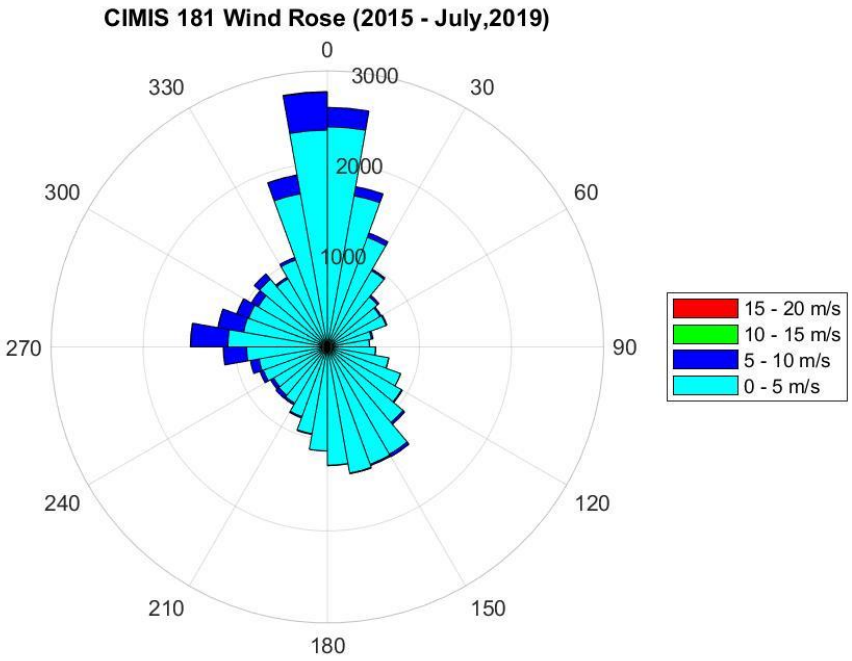

Figure 4.Wind rose diagram for original averaged wind data at station CIMIS 181 (2015-2019)

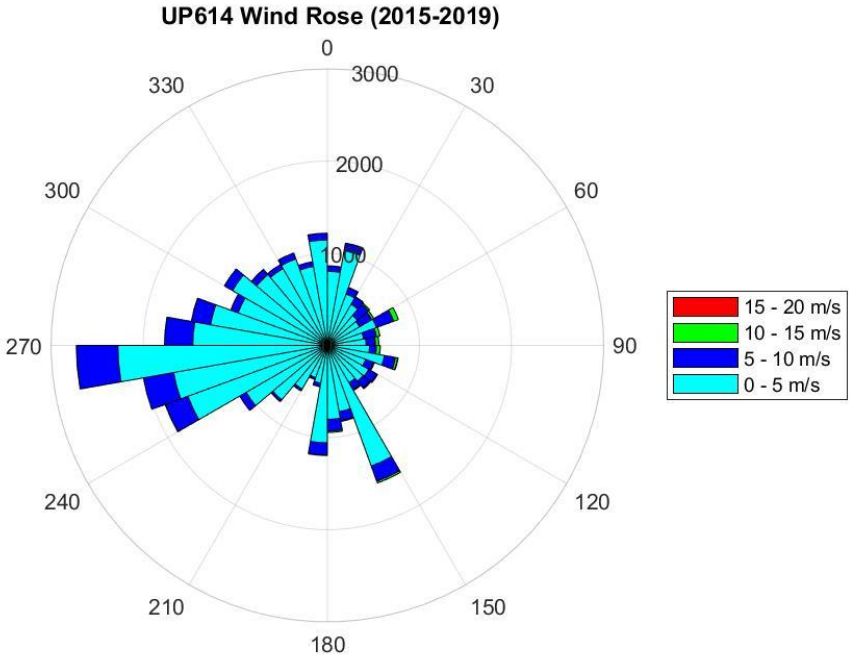

Figure 5. Wind rose diagram for original averaged wind data at station UP614 (2015-2019)

To estimate the desired wind speed over water from the records measured at a land-based station, the correction factors f_{OFF} for offshore winds is calculated as the ratio of downwind and upwind speed (u_{0D}/u_{0U}) in a boundary layer profile from (Eq. 2.4.1), but replacing upwind roughness length (z_{0U}) to the roughness length over land z_{0L} , and downwind roughness length (z_{0D}) to the roughness length over water z_{0w} (Eq. 2.4.2).

Conversely, for onshore wind roughness correction, the corresponding correction factors f_{ON} is the reverse of Equation 2.4.1, except that now $z_{0U} = z_{0w}$, and $z_{0D} = z_{0L}$ (Eq. 2.4.3) as the desired wind speed over water is u_{0U}.

$$u_{0D}(x,z) = \left[1 + \left(ln\frac{z}{z_{0U}} ln\frac{\delta(x)}{z_{0D}}\right) / \left(ln\frac{z}{z_{0D}} ln\frac{\delta(x)}{z_{0U}}\right)\right] \cdot u_{0U}(z) \quad (2.4.1)$$

$$f_{OFF} = \left[1 + \left(ln\frac{z}{z_{0L}} ln\frac{\delta(x)}{z_{0w}}\right) / \left(ln\frac{z}{z_{0w}} ln\frac{\delta(x)}{z_{0L}}\right)\right] \quad (2.4.2)$$

$$f_{ON} = 1/\left[1 + \left(ln\frac{z}{z_{0w}} ln\frac{\delta(x)}{z_{0L}}\right) / \left(ln\frac{z}{z_{0L}} ln\frac{\delta(x)}{z_{0w}}\right)\right] \quad (2.4.3)$$

In summary, the magnitude of correction factors depends on the internal boundary layer thickness as a function of the distance to shoreline x, $\delta(x)$, and land/water surface roughness lengths. Roughness over water (z_{0w}) was presumed to be 10^{-4}m, roughness over land for (z_{0L}) CIMIS 136 and 181 was 0.01 m, and measuring height (z), was 2 m over ground. The correction factors tabulated for each station is summarized in Table 2.

Table 2. Correction factors for each metrological station

	CIMIS 136	CIMIS 181	UP614
Distance to shore (x)	8647 m	3331 m	2627 m
f_{ON}	1	1	1
f_{OFF}	1.27	1.24	1.23

Height correction

The height correction procedure was undertaken according to the rules demonstrated by previous studies(Amorocho and J.J. 1980) (Huston 2000) (Rueda, Vidal, and Schladow 2009). The following set of adjustment is applied to the estimated wind records at 2 m height over water obtained from CIMIS 136 and 181 stations:

$U_{2W} < 6.09\ ms^{-1}$, $U_{10W} \approx 1.15 \times U_{2W}$ (2.4.4)

$6.09\ ms^{-1} < U_{2W} < 15.94\ ms^{-1}$, $U_{10W} \approx 1.32 \times U_{2W} - 1.03$ (2.4.5)

$U_{2W} > 15.94\ ms^{-1}$, $U_{10W} \approx 1.25 \times U_{2W}$ (2.4.6)

The anemometer for UP614 station, in Frink, CA is estimated to be about 15 m height over ground using *GoogleEarth* software. Extrapolation of the wind speed at 10 m height from a reference height (15m) was carried out using the log law in the following from shown in Eq. 2.4.7:

$$\frac{U(z)}{U(z_r)} = ln\left(\frac{z}{z_0}\right) / ln\left(\frac{z_r}{z_0}\right) \quad (2.4.7)$$

where z is the height above ground level for velocity U(z), z_r is the reference height where U(z_r) is known, and z_0 is roughness length of the measuring site.

Figure 6. The change of anemometer height over the surface water from 2015 (a) to October, 2019 (b) (pictures provided by JPL)

The anemometer at site SS1 was installed on the platform by JPL off the coast in southwestern corner of the Salton Sea since 2006. Therefore, no roughness correction is needed for the wind records from this station. However, due to high evaporation rate and reduction of tributary river flow rate since 2018, the height between the platform to water level has increased significantly from 7 feet (2006) to 11 feet (2015) to about 18 feet by May 2019 (Figure 6).

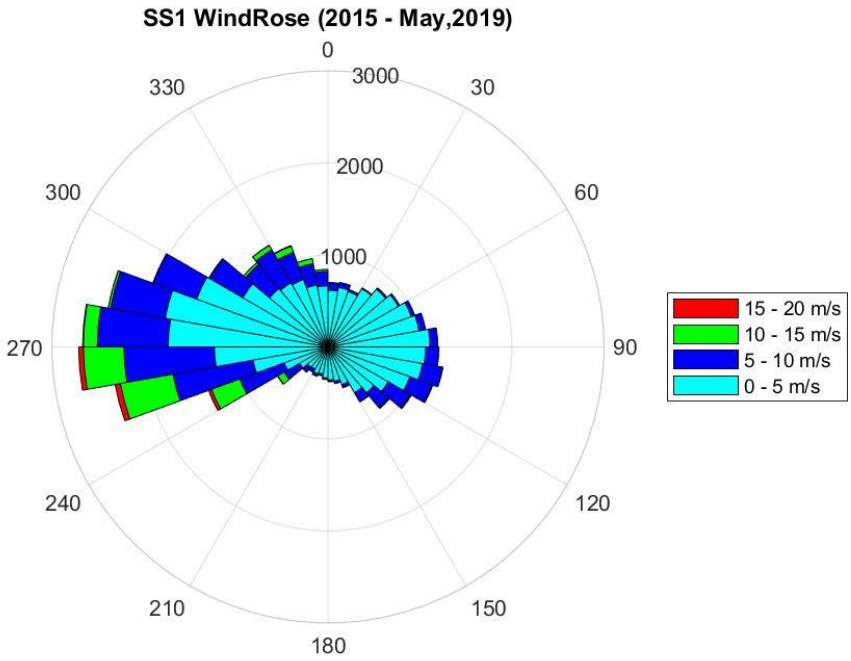

Figure 7. Wind rose diagram for averaged wind data at station SS1 (2015-2019)

Table 3. Summary of surface roughness length and anemometer instruments height at site UP614 and SS1 over the ground or water surface from 2015 to 2019

Anemometer height to the surface (m)	UP614	SS1
Surface roughness (z_0)	10^{-2}	10^{-4}
2015	15	4.8
2016	15	4.95
2017	15	5.1
2018	15	5.25
2019	15	5.4

The anemometer height over the water surface was assumed to increase in the increment of approximately 0.15 m per year (Table 3), and the log law shown in Equation 2.4.7 was applied to the wind speed measured from SS1 station to estimate the wind speed at the reference height of 10 meters over surface water each year.

2.4.3 Heat Budget Calculation

The exchange of heat through the free Salton Sea surface was computed by taking into account the short-wave radiation (solar wave), long wave radiation (atmospheric wave), and heat loss from the surface as shown in Equation 2.4.8. Among the four meteorological stations, records obtained in the following three stations, SS1, CIMIS 136 and CIMIS 181, provided the necessary parameters for the model. *The relative humidity (RH)*, *air temperature*, *and the short-wave solar radiation* are to be prescribed to the model, and the net atmospheric radiation, the heat loss due to evaporation and convection would be computed by the model.

$$Q_{tot} = Q_{sn} + Q_{an} - Q_{br} - Q_{ev} - Q_{co} \quad (2.4.8)$$

Q_{tot} The total heat flux through the air-water surface (J/m^{2}s)

Q_{sn} Net incident solar radiation (short wave) (J/m^{2}s)

Q_{an} Net incident atmospheric radiation (long wave) (J/m^{2}s)

Q_{br} Back radiation (long wave) (J/m^{2}s)

Q_{ev} Evaporative heat flux (latent heat) (J/m^{2}s)

Q_{co} Convective heat flux (sensible heat) (J/m^{2}s)

Once the total heat flux through the free surface is computed, the change in temperature in the top layer reads:

$$\frac{\partial T_s}{\partial t} = \frac{Q_{tot}}{\rho_w c_p \Delta z_s} \quad (2.4.9)$$

T_s The water temperature at the free surface (^{o}C)

ρ_w The specific density of water (kg/m3)

c_p The specific heat capacity of sea water (=3930 J kg^{-1}K)

Δz_s The thickness of the top later (m)

While shortwave radiation values were already provided by the CIMIS stations, the shortwave radiation values at the SS1 site need to be calculated using a series of MATLAB functions written and modified by Steve Margulis and Laurie Huning as part of the “Modular Distributed Watershed Educational Toolbox”.

Solar geometry entailing solar zenith and azimuth angles, hour of sunrise and sunset, solar declination and hour angles at each hour from 1/1/2015 to 5/13/2019 at SS1 station was calculated. Among which, zenith angle is the most critical parameter to compute the top of atmosphere solar incident flux (RsTOA).

Clausius-Clapeyron Equation (Equation 2.4.10) was used to compute hourly saturated vapor pressure (e_s) from the measured hourly air temperature (T), and from the measured relative humidity (%) the hourly vapor pressure was calculated. Then, due point temperature was calculated from the calculated hourly vapor pressure using the inverted Clausius-Clapeyron Equation (Equation 2.4.11). Finally, precipitable water was calculated based on an empirical equation (Equation 2.4.12) by Dingman (2008).

$$e_s(T) = e_{s0} exp\left(\frac{L_v}{R_V}\left[\frac{1}{T_0} - \frac{1}{T}\right]\right) \quad (2.4.10)$$

where L_v is the latent heat of vaporization of water (2.5 x 10^6 J/kg), R_v is the water vapor gas constant (461 J/kg/K), and T_0 and e_{so} are integration constants (273.16 K and 611 Pa, respectively).

$$e = e_s(T = T_d) = e_{s0} exp\left(\frac{L_v}{R_V}\left[\frac{1}{T_0} - \frac{1}{T_d}\right]\right) \quad (2.4.11)$$

where the dew point temperature (Td) is defined as the temperature that air would have to be cooled so that it reached saturation.

$$Wp = 1.12 \exp(0.0614 T_d) \quad (2.4.12)$$

precipitable water is expressed in depth (cm) and T_d in the unit of degree Celsius (C^o).

Having all the necessary parameters calculated and compiled, hourly clear-sky shortwave radiation at the surface of SS1 station was estimated using the following inputs data using the MATLAB code: RsTOA (W/m^2), solar zenith angle (rad), precipitable water (cm), non-dimensional dust coefficient, surface albedo, surface pressure (Pa).

Assuming dust coefficient is 0.1 and surface albedo is 0.25, the Dingman model also required to compute atmospheric attenuation factors that involved computations for direct shortwave transmissivity and diffuse shortwave scattering coefficient. Lastly, the hourly downward flux of shortwave radiation to the surface in the clear-sky condition at SS1 was estimated by multiplying RsTOA with attenuation factors. The hourly incoming shortwave radiation at SS1in 2015 was shown in Figure 8.

The range of shortwave radiation at noon was from approximately 560 W/m^2 to 1050 W/m^2 every year from 2015 to 2019, yielding similar plots as in Figure 8. At CIMIS 136 station, shortwave radiation was at similar range as at SS1, but at CIMIS 181 station in the south end of the Sea, the highest shortwave radiation at noon was 1482 W/m^2.

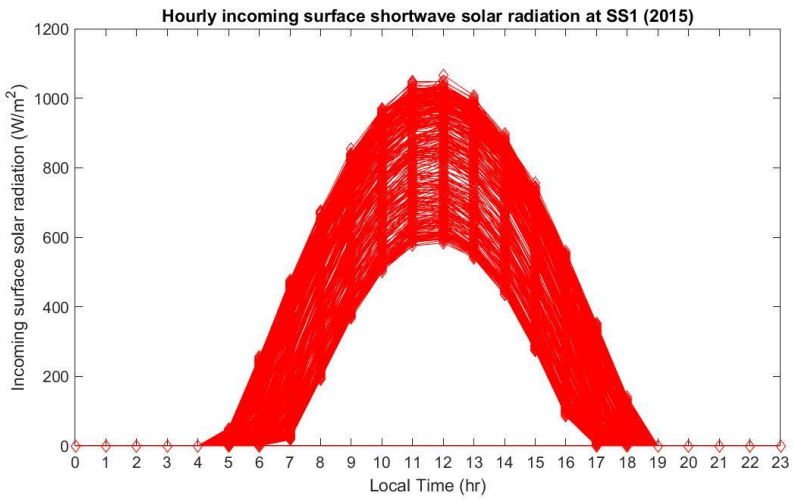

Figure 8. Estimated hourly downward shortwave radiation in clear-sky condition in year 2015

The timeseries records for relative humidity, air temperature and incoming solar radiation for cloudless sky from 2015 to 2019 obtained from the three meteorological stations were compiled, and the average hourly values of each parameter were used to prescribe the heat flux model in the Delft3D-flow.

2.4.5 Calibration and Validation

Water velocity calibration test (10/9/1997 – 10/24/1997)

The first field monitoring program to measure continuous vertical profiles of water velocities and water temperature was conducted by the UC Davis modeling team. The water velocities were measured using acoustic Doppler current profilers (ADCPs), and thermal structure of the Sea was characterized by thermistor strings. Five stations were selected for spot observation throughout the Salton Sea, among which long-term monitoring from 3/24/1997 to 1/5/1998 were deployed at Site 1 (south eastern basin) and Site 5 (northern basin) for water velocities calibration and validation analysis (Christopher Bruce Cook 2000).

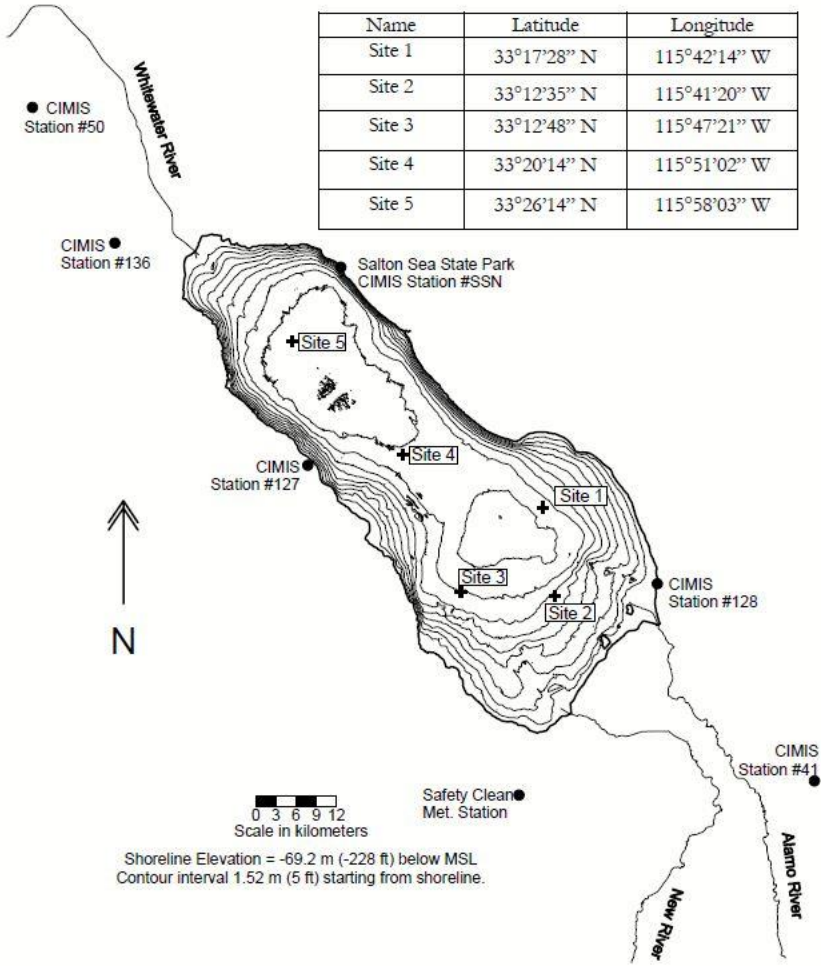

Figure 9. Locations of monitoring sites and CIMIS stations. Figure reprinted from *Internal Dynamics of a Terminal Basin Lake : A Numerical Model for Management of the Salton Sea* (p.49), C. B. Cook, 2000. Copyright 2000 by Christopher B. Cook.

The boundary conditions for Cook's hydrodynamic model were defined by six CIMIS stations around the periphery of the Salton Sea as shown in Figure 9. However, the historical data were available in only five of the stations to generate wind fields in 1997 (#41, #50, #127, #128, #136), where #50 was located in Vista Santa Rosa, 13 miles north from the north end of the Sea. The calibration period is based on the same calibration period carried out in Cook's study. During the field campaign, the October data set was considered the most representative of the water movement in the Salton Sea under non-stratified conditions and nearly complete lateral homogeneity for

temperature and conductivity. The calibration test was conducted by adjusting model parameters including horizontal eddy viscosity, vertical eddy viscosity, and manning's n as roughness coefficients in the following conditions summarized in Table 4.

Note that since measured water velocities for the 1997 field campaign were not available, the calibration task would be carried out by comparing the simulation results of the Delft3D and RMA10, and no validation task could be performed using Delft3D with this dataset.

Table 4.Summary of the two hydrodynamic models' settings for calibration

Model	Delft3D	RMA10
Timeframe	10/9/1997-10/24/1997	10/9/1997-10/24/1997
Timestep	30 mins	60 mins
Girds	1503 curvilinear grids	Finite elements
Layers	16 layers	2 layers
Water level	-69.5 m	-69.5 m
Process :Wind	CIMIS sites (#41, #50, #127, #128,#136)	CIMIS sites (#41, #127, #128, #136, #141, #154)
Process: Temperature	Off	24 ^{o}C, but no vertical temp gradient
Inflow	Off	N/A

Vertical Eddy Viscosity

Four vertical viscosities values were tested to compare with the results simulated using RMA10 finite element numerical model (Fig 10). In this Delft3D model, the second-order turbulence closure model, $k-\varepsilon$ model, was chosen to calculate the vertical viscosity, and the values shown in Figure 10a were user-defined background vertical viscosity (ν_V^{back}), which accounts for all other forms of unresolved mixing (Eq. 2.3.8). On the other hand, Mellor-Yamada Level II boundary layer closure method was used to calculate the vertical viscosities value in Cook's study (Figure 10b).

Comparing the two solution results, the u- velocity of the surface layer during the calibration period resembles that of RMA10's results. Water velocity peaked to about 0.15 m/s during the two storms events occurred on 10/11/1997 and 10/24/1997. Velocities generated by Delft3D were noisier than RMA10's, but followed the similar patterns of Cook's simulation result in general. In addition, the sensitivity tests conducted by model RMA10 were run with two vertical layers of finite elements, and only mid-depth results were shown and compared. Overall, the results showed that background vertical viscosity values did not affect horizontal velocity results. Since values 0.001 to 0.0001 m^2/s (0.103 Pa-sec) was the range recommended by Delft3D, 0.103 Pa-sec was the chosen value for the rest of the simulations.

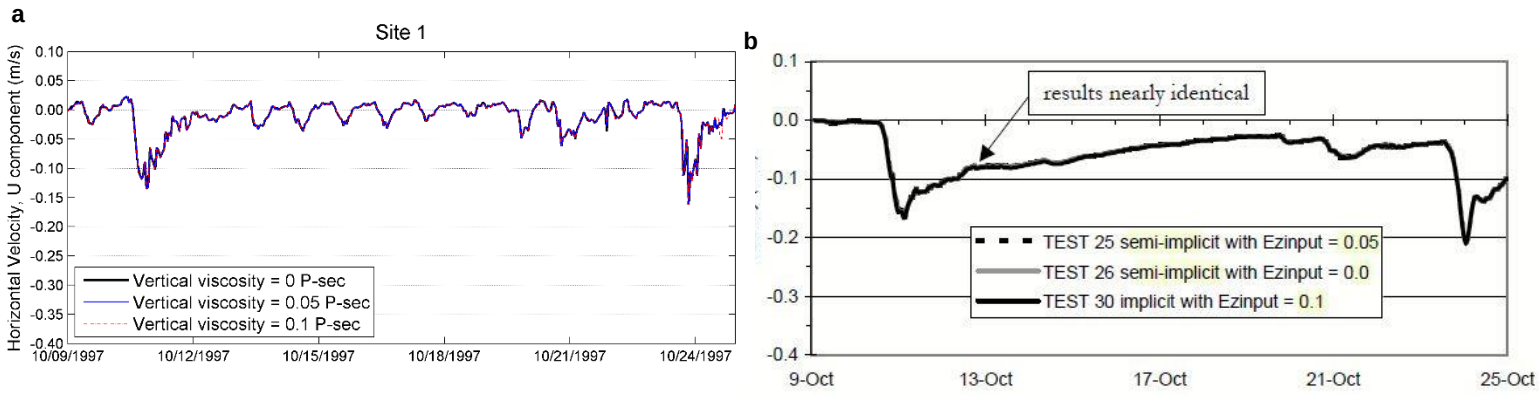

Figure 10. East/West velocity components for vertical viscosity tests by a) Delft3D model and b) RM10 model. Figure b) reprinted from *Internal Dynamics of a Terminal Basin Lake : A Numerical Model for Management of the Salton Sea* (p.89), C. B. Cook, 2000. Copyright 2000 by Christopher B. Cook.

Horizontal Eddy Viscosity

The horizontal eddy viscosities were tested using three different values, 10, 1000, 5000 Pa-sec, that were also tested by Cook (2000). Figure 11 demonstrated that there were no discernable differences between U components of the horizontal velocities. Therefore, the horizontal velocity was set at 1000 Pa-sec for all other simulations.

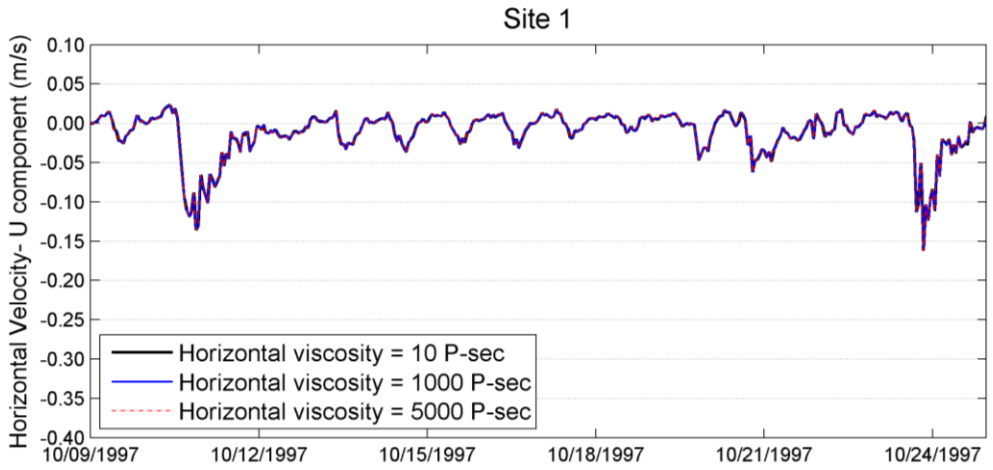

Figure 11. East/West velocity components for horizontal viscosity tests

Manning's n- n increases, reduces velocity

Manning's roughness coefficient (n) was chosen to compare the bottom roughness effects on horizontal velocity. Furthermore, For Manning's n of 0.01 and 0.008, two wave-current interaction models were tested: Fredsoe and Bijker. The results shown in Figure 12 indicated that increasing Manning's n values would decrease water velocity, especially during the period between storms. The simulated result for manning's n = 0.03 in my Delft3D model is similar to RMA10's Test 10 results where n was 0.03 in the south basin, and n was 0.01 in the north basin. When using Bijker model that determines shear-stress at the bottom, peak horizontal velocities increased to 0.2 m/s during the first storm on 10/11/1997, and to 0.15 m/s during the second storm

on 10/23/1997 compared to that of the Fredsoe model. Overall, using the Bijker model (Manning's n= 0.01) yielded the best result because the observed storm peak value for the October 11 storm event was 0.25 m/s, and for the October 23 storm event was 0.15 m/s. However, the u-velocity at Site 5 (North basin site) did not resemble that of RMA10's results due to lacking the wind source coming from the north eastern end of the Sea. The highest wind velocity at Site 5 from the Cook's model was 7 m/s during the storm on 10/11/1997, and less than 3 m/s for rest of the time. On the other hand, the highest wind velocities reached to 13 m/s and 8 m/s during the two storms at the same location in my model, which was about twice the magnitude of Cook's simulations.

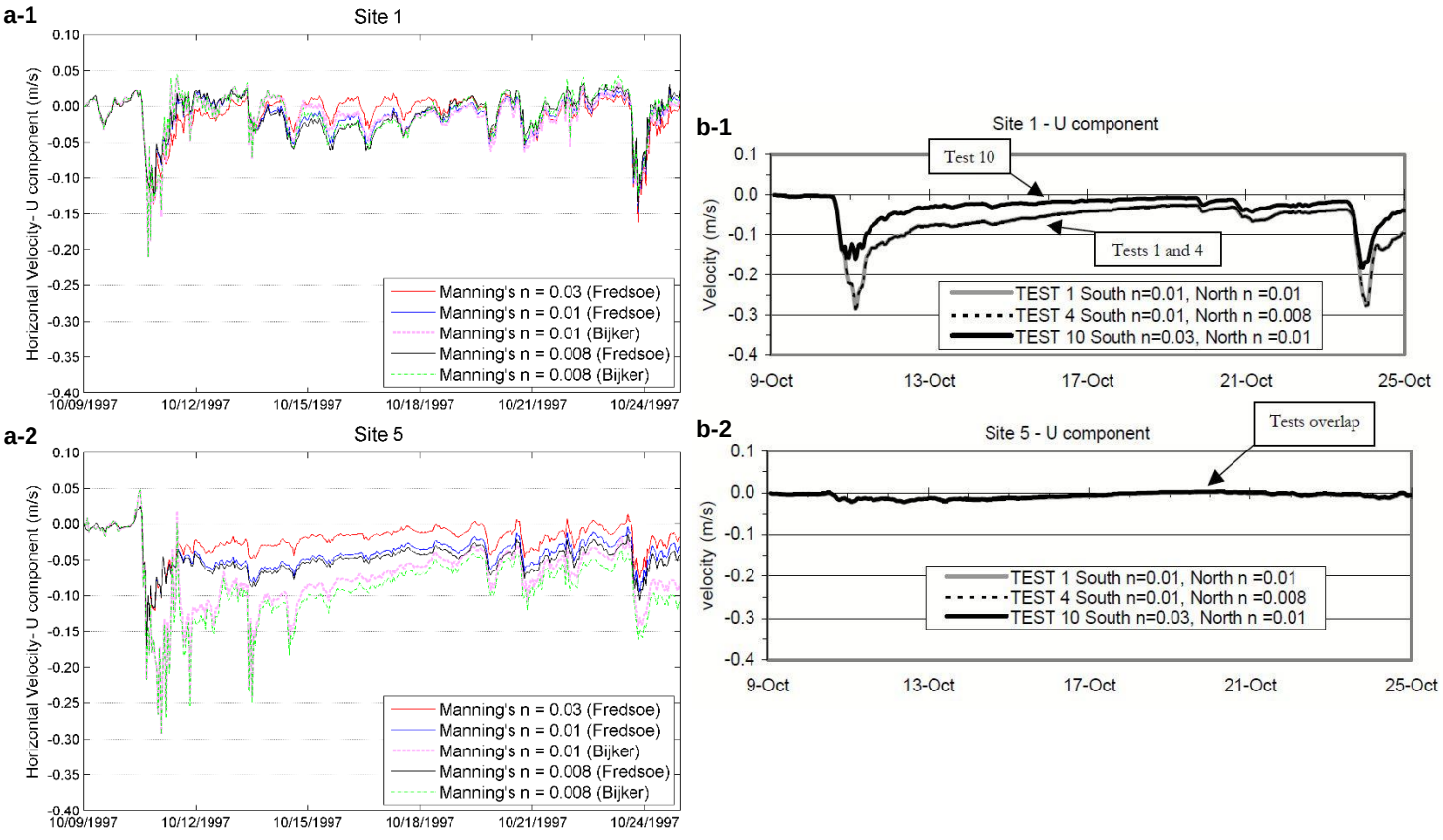

Figure 12. East/West velocity components for Manning's n tests by a-1), a-2) Delft3D model and b-1), b-2) RM10 model. Figures b-1, b-2 reprinted from *Internal Dynamics of a Terminal Basin Lake : A Numerical Model for Management of the Salton Sea* (p.77), C. B. Cook, 2000. Copyright 2000 by Christopher B. Cook.

Meteorological Station Numbers

Horizontal velocities under different wind fields generated by four wind stations (#41, # 127, #128, and #136) and by five stations (#41, #50, # 127, #128, and #136) were compared and shown in Figure 13. Neglecting the furthest wind station (#50) resulted in a slightly larger horizontal velocity during the storms event occurred on 10/11/1997. Overall, horizontal velocities are not influenced much by the two wind fields.

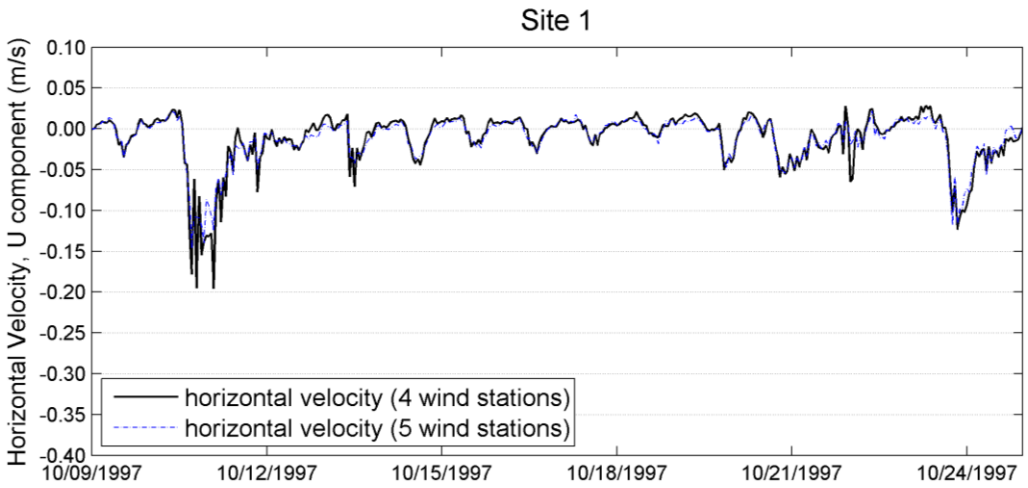

Figure 13. East/West velocity components for wind fields test

Refined Vertical Grids

Four vertical layers were compared to evaluate vertical refinement effects on horizontal velocities. The layer thickness is uniform for vertical layers that is based on Cartesian co-ordinates (Z-grid): 2, 4, and 8 layers, whereas, for vertical grids that contained 16 layers the distribution of the relative layer thickness is non-uniform, and is based on the σ-grid. Figure 14 shows that fewer vertical layers underestimated the horizontal velocities in general, especially during storms events.

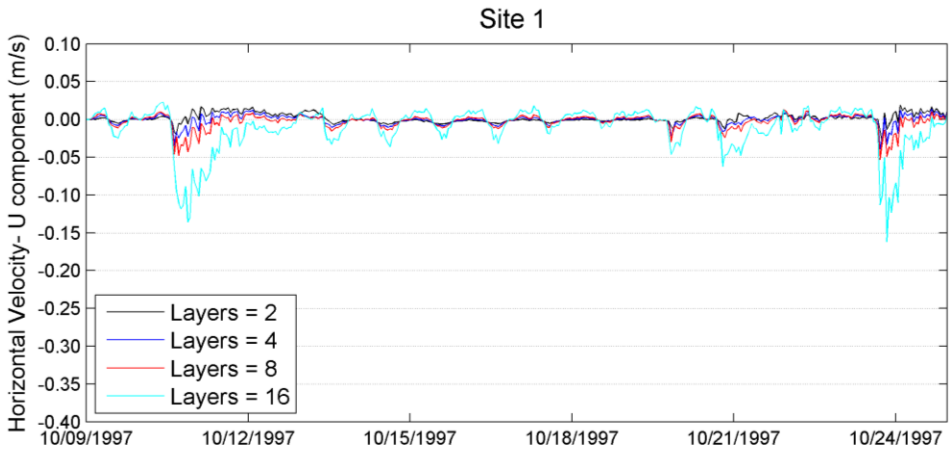

Figure 14. East/West velocity components for vertical resolution test

Timesteps

The sensitivity of the timestep variable was evaluated and presented in Figure 15. It was shown that the horizontal velocities are not affected by timesteps, therefore 30 minutes would be selected for the calibration task comparing to the Cook's dataset.

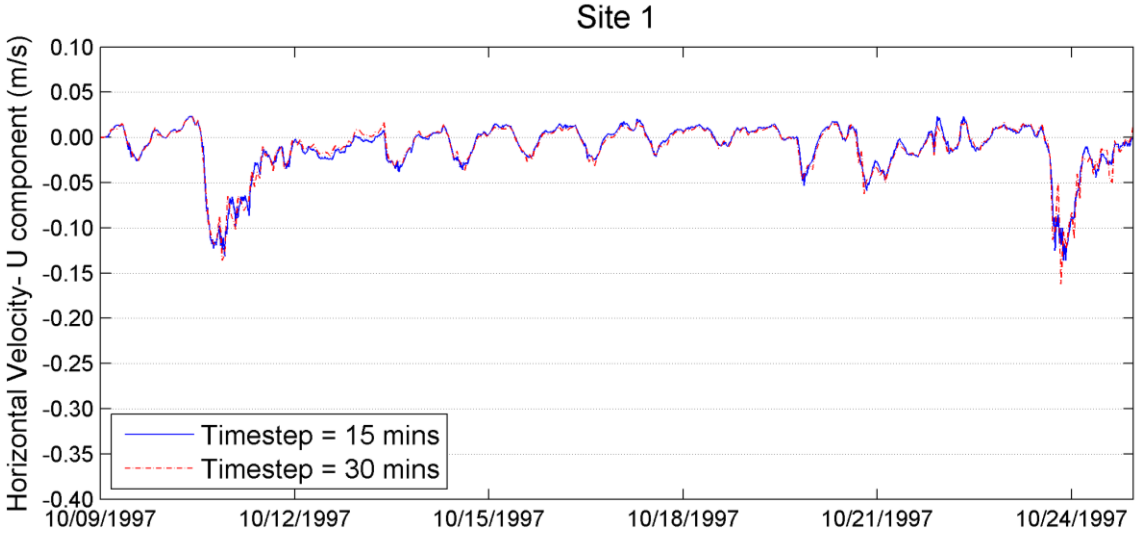

Figure 15. East/West velocity components for time step test

Grid Resolution at timestep = 15 mins

Using the timestep of 15 minutes, three grid resolutions were tested to evaluate their influences on horizontal velocities. Figure 16 show that grid resolutions have no impact on flow velocities.

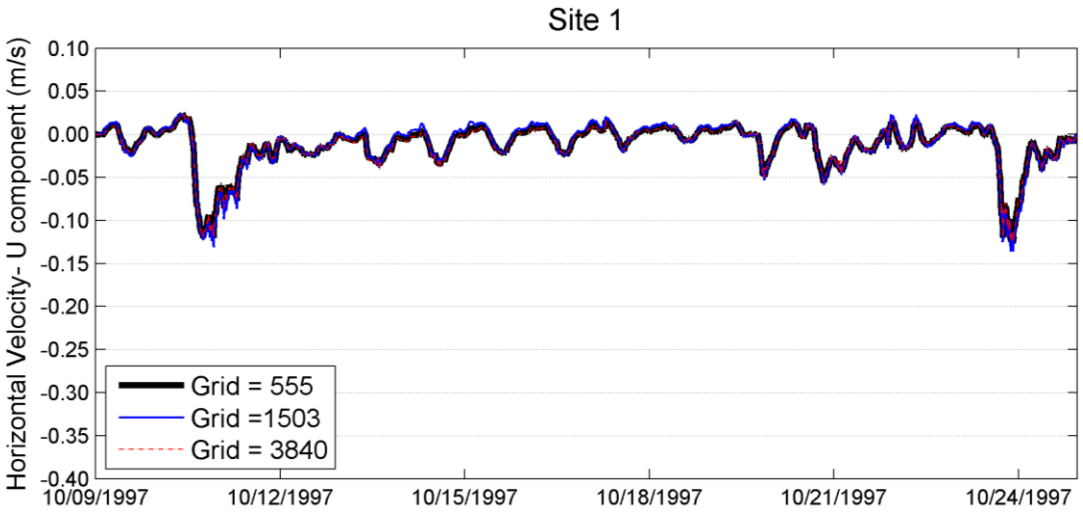

Figure 16. East/West velocity components for grid resolution test

Wave and current calibration/validation test (8/8/2005 – 9/17/2005)

Chung et al. (2009) conducted a field measurement program (8/2/2005 to11/25/2005) to collect the following data in synchronization at the Salton Sea: currents and waves, water temperature, turbidity (surrogate for suspended sediment concentration). The main objective of this paper is to investigate how wave, currents, and surface seiches effect on the sediment resuspension in the water column.

Wave and currents were measured by the use of a Nortek acoustic wave and current (AWAC) profiler at frequencies of 7 Hz for wave characteristics (30 min interval), and of 4.34 Hz for currents (10 min interval); turbidity data were collected by OBS sensors that were deployed 0.5 m off the bottom of the water depths of 4, 6, and 8 m in

the southeastern basin of the Salton Sea; temperature was measured by a UC Davis thermistor chain. The station #128 from the CIMIS was the sole source provided the data of wind speed and direction with a time interval of 60 minutes (Fig. 17).

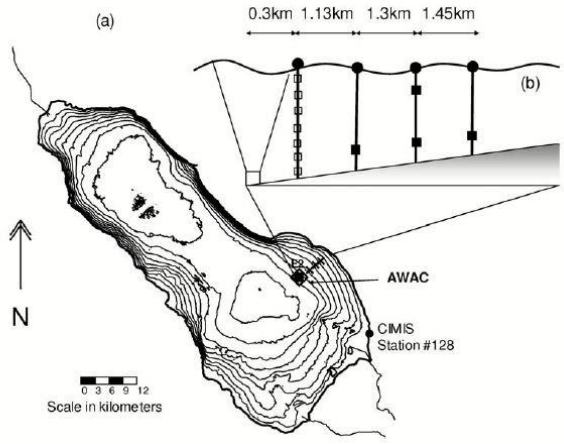

Figure 17. The location of the AWAC profiler (diamond shaped mark), OBS sensors (cross mark), thermistor chain (square mark), and CIMIS meteorological station (circle mark). Figure reprinted from *"Sediment Resuspension in a Shallow Lake."* by E.G. Chung, 2009a, *Water Resources Research*, 45, p.3. Copyright 2009 by the American Geophysical Union.

The compilation of meteo-lake conditions characterized during 8/8/2005 to 9/17/2005 was used to calibrate and validate Delft3D-Wave module. The calibration period is from 8/8/2005 00:00:00 to 9/9/2005 18:00:00, and the validation period is form 9/9/2005 00:00:00 to 9/17/2005 00:00:00. During the calibration period wind speed varied from 2 to 8 m/s while wave height ranged between 0.3 to 1.8 m. September 9 18:00 showed the highest wind speed (13.4 m/s) coming from 246^{o}, and 0.5 m of wave height followed by approximately 1.8 m of wave height in an hour later. The prevalent meteo-lake conditions were characterized by a low wind speed (2 m/s coming from ~70^{o}) and wave height of less than 1 m.

Table 5 summarized the processes, boundaries and parameters utilized in Delft3D-FLOW to carry out the hydrodynamic conditions of the Salton Sea driven by the

wind field based on the wind data measured at the CIMIS #128 meteorological site. The initial condition of sediment concentration was collected by the Bureau of Reclamation, and the discharge rates for open boundary at the New and Alamo River were obtained by the *USGS Surface-Water Daily Data for California.*

Table 5. Delft3D-FLOW hydrodynamic setting for wave calibration and validation (8/8/2005 - 9/17/2005)

Domain					
Grid	M=29 N=59 Sigma-coordinates= 16 layers				
Time step	1 min				
Initial conditions					
Water level	-69.6 m	vertical datum NAVD88			
Sediment concentration	0.077 kg/m^3				
Boundaries	Open boundary type	Forcing	Reflection parameter alpha	Vertical profile for hydrodynamics	Transport conditions
New River	total discharge	time-series	0 s	logarithmic	Sediment concentration
Alamo River	total discharge	time-series	0 s	logarithmic	Sediment concentration
Physical parameters					
Wind drag coefficients	Breakpoint A Breakpoint B Breakpoint C	0.00104 0.00145 0.00145	0 m/s 11 m/s 14 m/s		
Roughness formula	Roughness formula: *Manning* U:0.01 V:0.01	Stress formulation due to wave forces: *Bijker*			
Horizontal Viscosity/diffusivity	1 m^2/s 1 m^2/s				
Vertical viscosity	0.0001 m^2/s				
Model for 3D turbulence	k-Epsilon				
Sediment	Cohesive sediment				
Reference density for hindered settling	1600 kg/m^3				
Specific density	2650 kg/m^3				
Dry bed density	500 kg/m^3				
Fresh settling velocity	0.25 mm/s				
Saline settling velocity	0.25 mm/s				
Critical bed shear stress for sedimentation	0.0625 N/m^2				
Critical bed shear stress for erosion	0.0625 N/m^2				
Erosion parameter	0.0001 kg/m^2/s				
Initial sediment layer thickness at bed	0.05 m				
Wind					
CIMIS 128	Space-temporal varying wind				
Interpolation type	linear				

The hydrodynamic results were then used as input data in the Delft3D-WAVE module to simulate wave characteristics of the Salton Sea, and the parameters and processes activated were summarized in Table 6. Two nesting grids were added in addition to the computational grid from Delft3D-FLOW in the south basin of the Salton Sea; the secondary grids (2187 grids) cover 2/3 of the south basin, and the tertiary grids (648 grids) contains approximately 3miles within the proximity of the wave data measuring site (AWAC) by Chung et al. (2009) shown in Fig.17. Delft3D-WAVE module is run by the third generation **S**imulating **WA**ves **N**earshore (SWAN) model. In this study, the generation mode for physical formulation is the 3rd generation, which activated depth-induced breaking and bottom friction. Additional physical processes that are subject to modification, wind growth, quadruplets, refraction and frequently shift are selected.

Table 6. Delft3D-WAVE setting for wave calibration and validation (8/8/2005 to 9/17/2005)

Grids	
Nesting	Secondary (M=28, N= 82)
	Tertiary (M=28, N=25)
Spectral resolution	Lowest Frequency/ Highest frequency
	0.05/1 (default value)
Current type	Surface layer
Physical parameters	
Water density	1031 kg/m^3
North w.r.t. x-axis	42^o
Minimum depth	1 m
Convention	nautical
Forces	Wave energy dissipation rate 3D
Generation mode for physics	3rd generation
Depth-induced breaking (B&J model)	Alpha=1 (default value) Gamma 0.73 (default value)
Bottom friction	JONSWAP= 0.067 (m^2/s^3) (default value)
Processes activated	
	Wind growth
	Quadruplets
	Refraction
	Frequenty shift
Computational mode	
	Stationary

Two boundaries were defined by orientation: South and Northwest side of the computational grid, respectively, and from which the wave boundary conditions are imposed (Table 7). Conditions along each boundary move counterclockwise, the incident wave field is prescribed at 0 m and 1658 m from the begin point of the side. The wave directions were selected based on the prevalent wind directions measured from CIMIS #128: 118^{o}, 219^{o} in the south boundary, and 243^{o}, 258^{o} from the northwest boundary. Note that because the grid is rotated counterclockwise 42^{o} with respect to the x-axis, the measured wind directions were subtracted by 42^{o} to obtain the incident wave directions for the boundary conditions. Two significant wave heights were prescribed depending on the distance from the corner point, 0.2 m at 0 m from corner point, and 0.48 m from 1658 m from corner point.

Table 7. Summary of boundary condition parameters in Delft3D-WAVE

Boundaries					
Orientation	South				
Conditions along boundary					
		Section 1	Section 2	Section 3	Section 4
	Distance from corner point	0 m	1658 m	0 m	1658 m
	Significant wave height	0.2 m	0.48 m	0.2 m	0.48 m
	Peak period	2.5 s	2.5 s	2.5 s	2.5 s
	Direction (nautical)	118^o	118^o	219^o	219^o
	Directional spreading	4 (default)	4 (default)	4 (default)	4 (default)
Orientation	Northwest				
Conditions along boundary					
		Section 1	Section 2	Section 3	Section 4
	Distance from corner point	0 m	1658 m	0 m	1685 m
	Significant wave height	0.2 m	0.48 m	0.2 m	0.48 m
	Peak period	2.4 s	2.4 s	2.4 s	2.4 s
	Direction (nautical)	243^o	243^o	258^o	258^o
	Directional spreading	4	4	4	4
Specification of spectra					
Shape	JONSWAP	Peak enhanced factor =1.1			
Period	Peak				
Directional spreading	Cosine power				

Sensitivity tests were conducted to evaluate various processes and parameters effects on simulating significant wave height and current magnitudes. The period for sensitivity study is from 9/5/2005 00:00 to 9/9/2005 23:00, during which the highest storm occurred and generated the highest wave height on 9/9/2005 at 18:00 at the AWAC monitoring site (Fig.18). The sensitivity of physical processes of SWAN including

Non-linear triad interaction, Diffraction, and Whitecapping in the presence of the default activated processes in the 3rd generation mode for physics- Depth-induced breaking and Bottom friction - were carried out and shown in Figure 19.

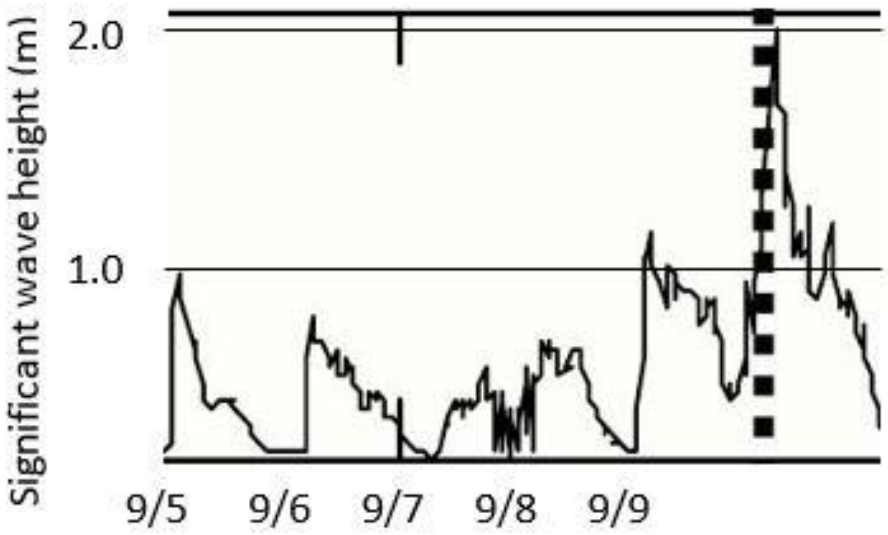

Figure 18. Measured significant wave height at AWAC site in the southeastern basin of the Salton Sea during 9/5/2005 to 9/9/2005. Figure reprinted from *"Sediment Resuspension in a Shallow Lake."* by E.G. Chung, 2009a, *Water Resources Research*, 45, p.5. Copyright 2009 by the American Geophysical Union.

Physical Processes

In Figure 19 it is shown that Whitecapping process had significant impact on the level of the significant wave heights, the effect was more prominent during storm events, causing doubling of the significant wave height on 9/9/2005 when whitecapping is deactivated. The magnitudes of the wave heights matched well with what were measured at the AWAC site (Fig.18). Therefore, the Whitecapping process would be de-activated throughout this study. On the other hand, the simulation output was under-estimated compared to the measured when only the "Non-linear triad interaction" and "Diffraction" were de-activated among the rest of the physical processes including the 3rd-generaito mode default processes "Depth-induced breaking" and "Bottom friction",

as well as “Diffraction”, “Wind growth”, and “Quadruplets” processes.

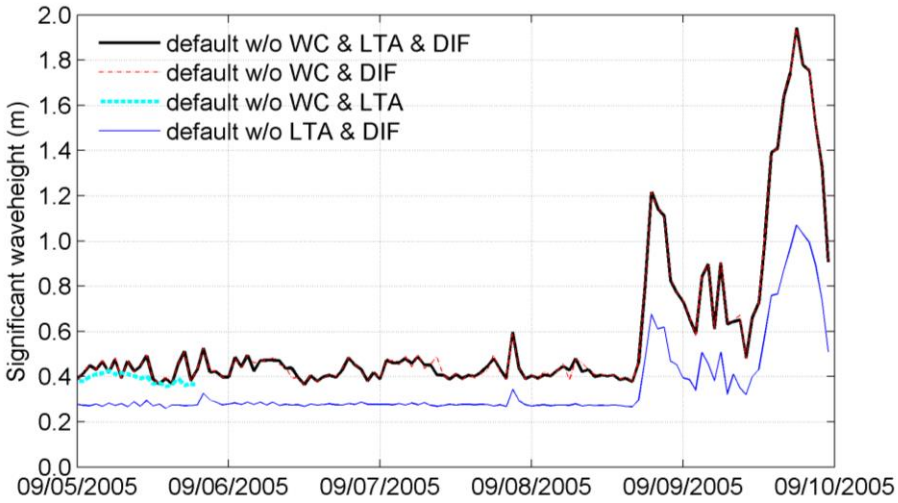

Figure 19. Sensitivity test results for significant wave heights simulated under various combinations of activated physical processes: non-linear triad interaction (LTA), Diffraction (DIF), *and* Whitecapping (WC).

Lastly, the results of significant wave height simulation were interrupted when only the “Non-linear triad interaction” and “whitecapping” were de-activated among the rest of the physical processes.

Minimum depth

Minimum depth is the constant value below which points are excluded from the computation, and the value determines the minimal level of significant wave heights. As it shows in Figure 20, the higher the minimum depth, the lower the starting level of the significant wave heights. The minimal levels lower than 2 m generated pretty similar results, starting at 0.4 m and reached to about 0.5 m during low wind speeds period from 9/5/2005 to 9/8/2005, and to 1.9 m during the storm at 18 pm on 9/9/2005. The test results showed that the minimum depth value of 3 m decreased the starting level to

about 0.35 m, but the peak levels remained consistent with that of the results from lower minimum depths. The wave height was started at 0.3 m when the minimum depth was at 4 m, which is closest to the measured values. As the results, minimum depth of 4 m was selected to simulate the wave activities at the Salton Sea.

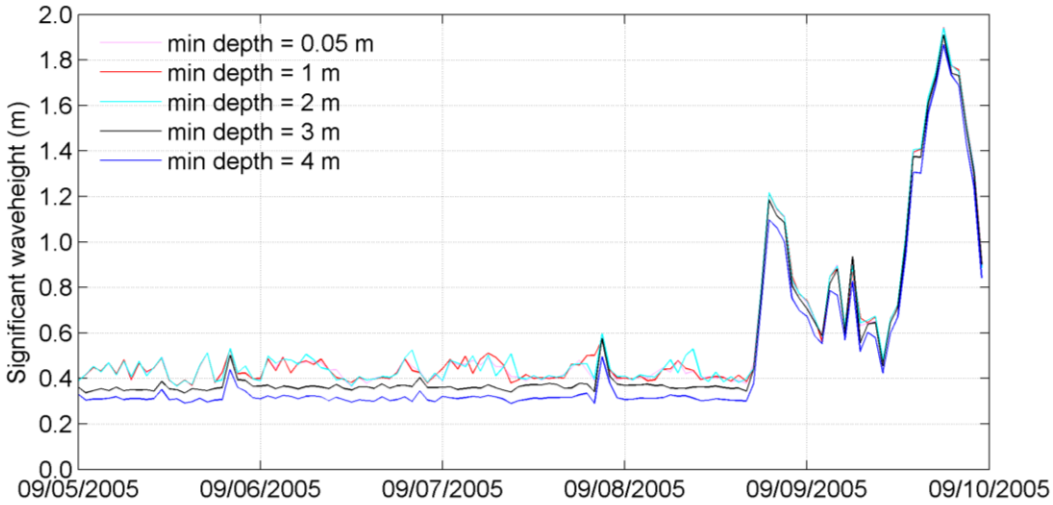

Figure 20. Sensitivity test results for significant wave heights simulated under various minimum depths.

Boundary orientation

The incident wave conditions at the boundary are critical to determine the significant wave heights and current magnitudes for the wave simulation. In this sensitivity test, the number of boundary sides and boundary orientations were evaluated to see the effects on significant wave heights. It should be noted that only the first computational grid is prescribed with incident wave boundary conditions.

The wave boundary orientations were determined based on the prevalent wind direction measured at the CIMIS #128 site (Fig.21). According to Figure 21,

predominant wind direction was from northwest, southeast, and southwest directions, wind blowing from 240º to 270º was especially stronger than the rest of the direction.

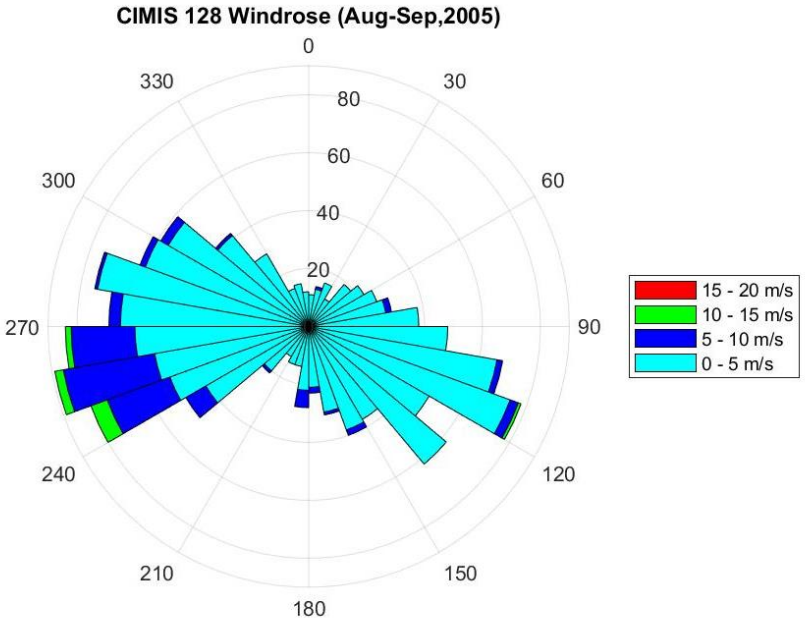

Figure 21. Wind speed and direction from 8/1/2005 to 9/27/2005 measured at CIMIS #128 at the Salton Sea.

In Figure 22, boundary condition that included west and northwest boundaries generated an overestimated wave heights during the low wind period from 9/5/2005 to 9/7/2005 compared to the measured wave heights shown above, and thus showing no contrast between the low winds and the storm. In addition, it was noticed that using only two boundaries contained south and northeast orientations yielded the same results compared to further divided south orientations into southwest and southeast orientations. Comparing the boundary conditions of Test 13 and Test 21 summarized in Table 6, it is shown that boundary orientation is the most critical parameter in influencing the magnitude of wave heights, and that the prescribed incident wave heights would be inhibited by boundary orientations. In Figure 22, it shows that the

wave heights of Test 21 were the same as Test 13 despite the fact that the prescribed incident wave heights were up to three times higher than that of Test 21.

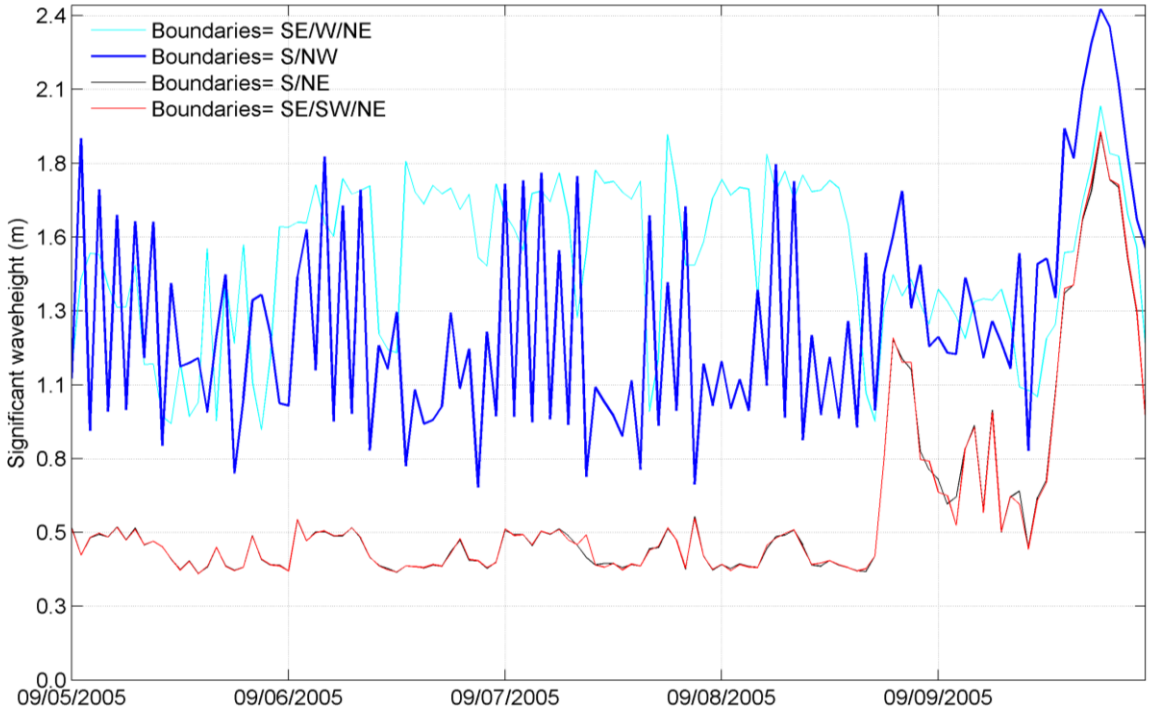

Figure 22. Sensitivity test results for significant wave heights simulated using various boundary conditions.

Table 8. Boundary conditions for sensitivity tests-9,11,13 and 21

	Orientations	Min. Depth (m)	0 m From corner point	1658m From corner point	0 m From corner point	1658m From corner point	0 m From corner point	1658m From corner point
			Sec1	Sec2	Sec3	Sec4	Sec5	Sec6
Test 9	**SE**	1	0.6m/118º	1.2m/118º				
	SW		0.1m/219º	1.5m/219º	0.6m/258º	0.6m/258º		
	NE			0.2m/0º		0.5m/58 º		
Test 11	**SE**	1	0.6m/118º	1.2m/118º				
	W		0.1m/219º	1.5m/219º	0.6m/258º	0.6m/258º		
	NE			0.2m/0º		0.5m/58 º		
Test 13	**S**	1	0.6m/118º	1.2m/118º	0.1m/219º	1.5m/219º	0.6m/258º	0.6m/258º
	NE			0.2m/0º		0.5m/58 º		
Test 21	**S**	1	0.2m/118º	0.6m/118º	0.2m/219º	0.6m/219º		
	NW		0.2m/243º	0.6m/243º	0.2m/258º	0.6m/258º		

Overall, this set of sensitivity test indicated that universal incident wave heights (0.2 m, 0.6 m) at the boundary conditions are sufficient to generate significant wave heights up to 1.82 m as long as the boundary orientations are consistent with prevalent wind directions. As the results, boundary orientation of south and northwest would be used to carry out calibration and validation runs.

Incident significant wave height

The impact of initial significant wave heights at the boundary on simulated significant wave heights are shown in Figure 23. At the minimum depth of 3 m, the initial wave height of 0.65 m prescribed at 1658 m from the corner point yielded overestimated wave heights during the low wind period form9/5/2005 to 9/8/2005; the observed values were below 0.6 m, which were 0.2 m lower than the simulated peak heights. However, initial wave heights of 0.4 m and 0.55 m at the boundary condition produced shallow significant wave heights where the total heights were less than 0.1 m before the storm occurred (upper figure).

As the results, minimum depth was adjusted to 4 m in order to reduce the lower bound of the simulated significant wave heights (lower figure). The initial wave heights of 0.48 m and 0.5 m both generated trends that resembled the observed values reasonably well. Since, majority of the observed wave heights were less than 0.5 m, initial significant wave heights at the boundary would be set at 0.48 m for calibration and validation tasks (Fig. 23).

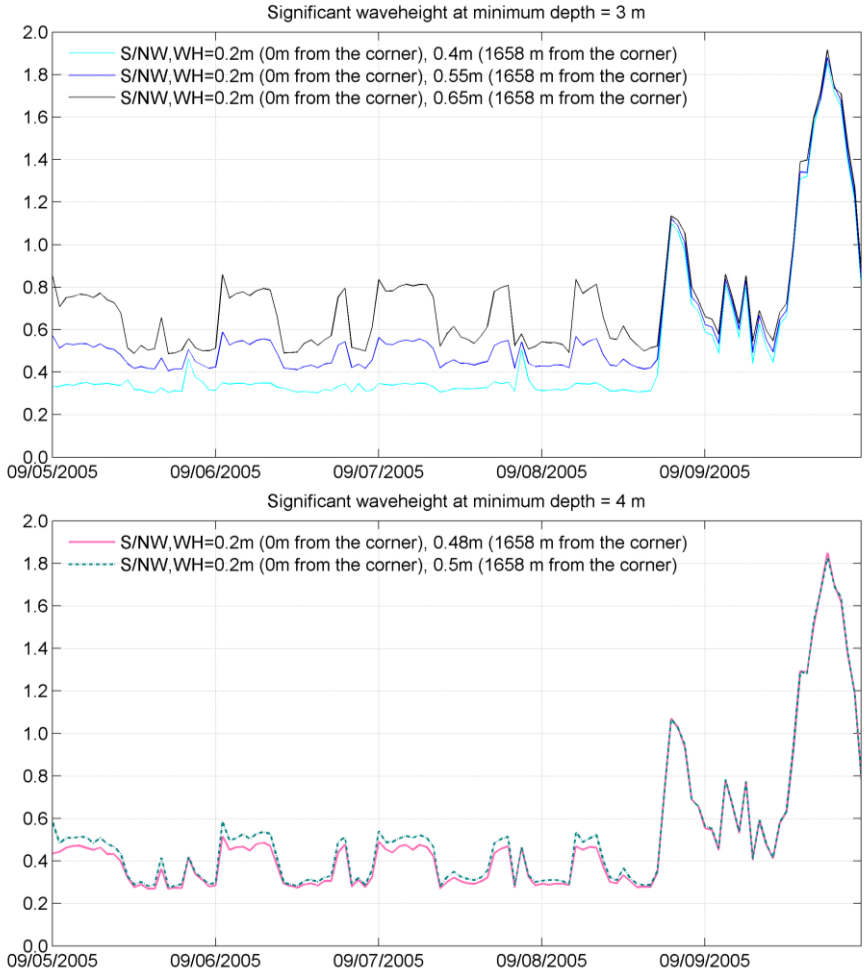

Figure 23. Sensitivity test results for significant wave heights simulated by different incident wave heights at two minimum depths

Calibration (08/08/2005 00:00 to 09/01/2005 00:00)

The calibration period stretched from 8/8/2005 00:00 to 9/1/2005 00:00. The simulated significant wave heights were compared against the data measured by Chung et al. (2009) using the AWAC at the southeastern basin of the Salton Sea. The wind velocity during the calibration period, the simulated significant wave heights overlaying the measured data, and the simulated current magnitude overlaying the measured current speeds were shown in Figure 24a, 24b, and 24c, respectively.

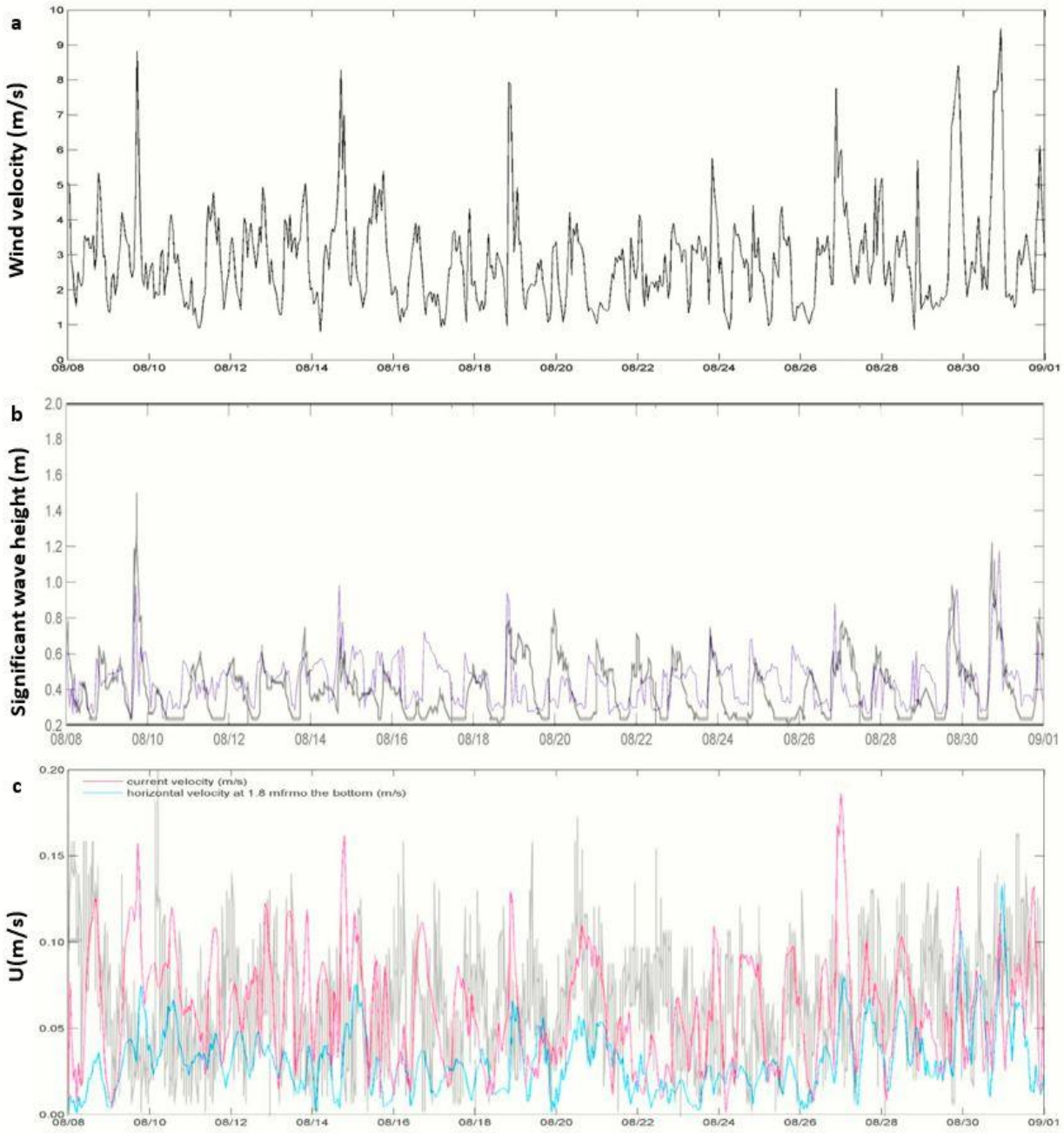

Figure 24. Comparison of measured and simulated variables of (a) wind velocity, (b) significant wave height, and (c) current speed in 1.8 m from the bottom during calibration period from August 8 to September 1 2005.The measured values were shown in black lines, the simulated wave height was in purple lines, simulated current velocity wasin pink line and simulated horizontal velocity was in blue line. Figures adapted from *"Sediment Resuspension in a Shallow Lake."* by E.G. Chung, 2009a, *Water Resources Research*, 45, p.5. Copyright 2009 by the American Geophysical Union.

During the calibration period, the predominant wind speed was in the range of 2 to 5 m/s, and occasionally the speeds reached to 8 to 9 m/s. In Figure 24b, it was noticed that significant wave height peaks were synced with higher wind speed spiks, indicating that wave characteristics are strongly driven by winds in the Salton Sea. The Delft3D-WAVE was able to simulate the shape and strength of the wave heights during the high wind conditions (8 – 9 m/s) and low wind speed (2 m/s) relatively well. Nonetheless, medium wave heights (~0.6 to 0.8 m) resulted from medium wind speed (~ 4 - 5 m/s) were not captured well by Delft3D WAVE.

In Figure 24c, simulated current velocity magnitudes (depth averaged) were overlayed with the measured current magnitudes (in 1.8 m from the bottom) during calibration period. The velocity measurement in the first 1.8 m above the bottom were within the “blanking distance”, therefore, the measured profile of current magnitudes was started at 1.8 m above the bottom. As shown in Figure 24c, the simulated current velocities (shown in magenta) followed the general trends/magnitude of current fluctuations. On the other hand, the simulated horizontal velocity magnitudes (shown in blue) at 1.8 m from the bottom was compared to the measured current velocity at the same depth. The results showed that the lower bounds of the measured current speeds were matched relatively well with the horizontal velocity at 1.8 m.

Validation (09/01/2005 00:00 to 09/17/2005 00:00)

The validation period is from 9/1/2005 00:00 to 9/17 00:00, the restart file taken form the last timestep of the calibration simulation was used to initiate the validation run. During the validation period, a storm occurred on 9/9/2005 at 18:00, generating highest wind speed of 13.2 m/s and kept remaining strong until 9/14/2005 (Figure 25a).

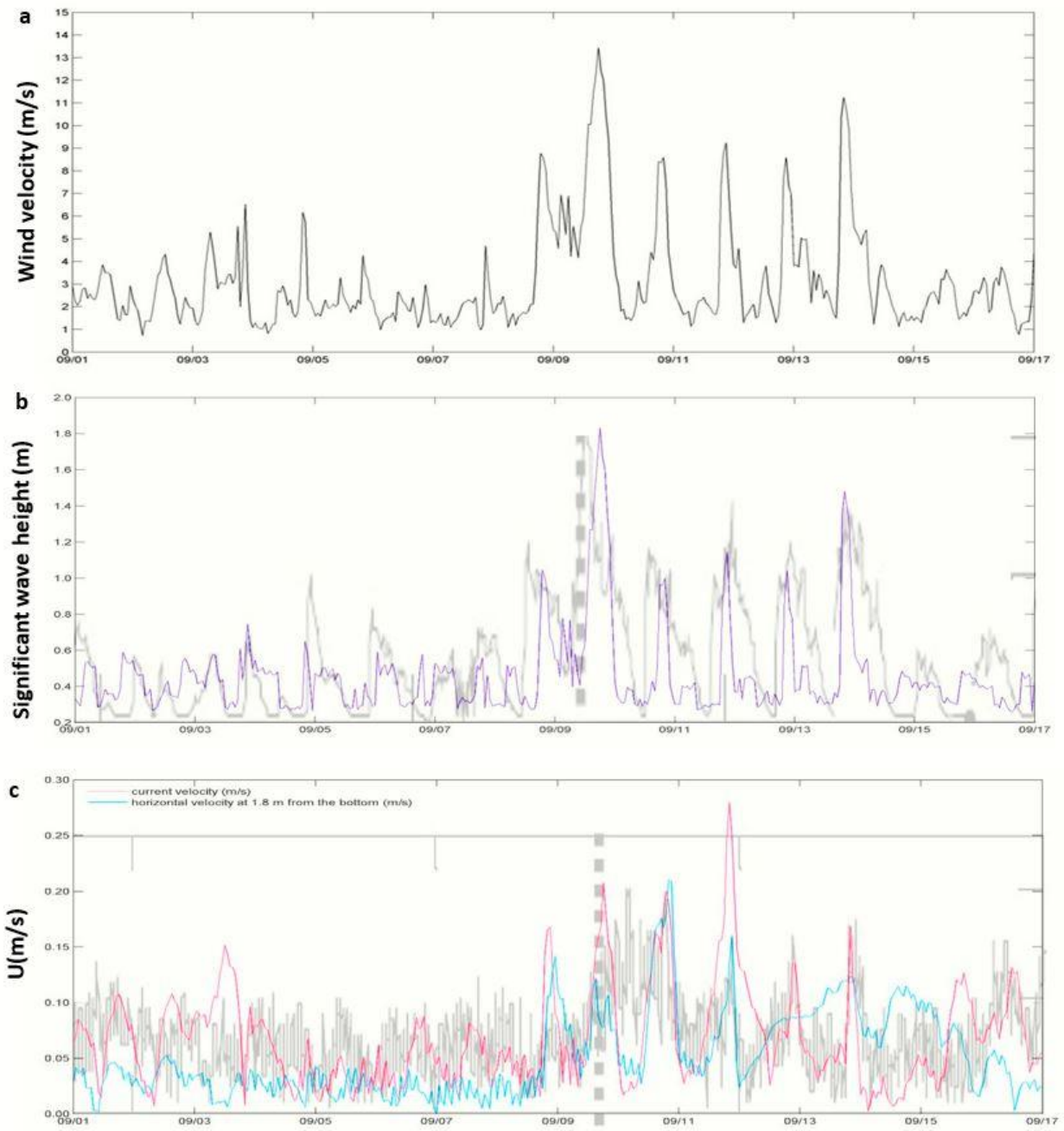

Figure 25. Comparison of measured and simulated variables of (a) wind velocity, (b) significant wave height, and (c) current speed in 1.8 m from the bottom during validation period from September 1 to September 17 2005. The measured values were shown in black lines, the simulated wave height was in purple lines, simulated current velocity was in pink line and simulated horizontal velocity was in blue line. Figures adapted from "*Sediment Resuspension in a Shallow Lake"* by E.G. Chung, 2009a, *Water Resources Research*, 45, p.5. Copyright 2009 by the American Geophysical Union.

Delft3D-WAVE successfully simulated the high significant wave heights during the storm period, and was able to matched the peak values well with the measured data. However, due to the fact that medium wave heights (0.6 to 0.8m) were not carried out well by the model, the width of the wave heights were thinner compared to the observed data. Overall, the wave heights shapes during the storm periods were corresponding to the shapes of the wind speed spikes (Fig. 25b).

The simulated depth-averaged current velocity (pink line) showed a rather good fit to the observed value, except an overestimation of up to 0.27 m/s during the storm period. On the other hand, the simulated horizontal velocity at1.8 m from the bottom (blue line) followed the lower bounds of the measured values well except after the storm period where the highest wind speed was recorded on 9/9/2005 18:00, it exceeded the lower bound and matched well with the measured data at approximately 0.2 m/s, and remained to match the current magnitude until 9/16 (Fig. 25c).

Chapter 3. Modeling Sediment resuspension in the water column

3.1 Abstract

Existing parametric models estimate the sediment resuspension rate by describing the dependence of entrainment rates on the following parameters: bed shear stress, shear velocity, wind velocity and sediment size. Choosing the most suitable formulations for the lake systems has become a challenge as the widely disparate results under the same conditions would lead to biased interpretation of sediment behaviors in lakes. Chung et al. (2008 and 2009) made the first attempt combining sediment resuspension models with a hydrodynamic/water quality model (Dynamic Lake model-water quality, DLM-WQ) to investigate the effect of sediment resuspension on nutrient cycling in the Salton Sea. Physical component such as temperature and salinity (vertical distribution) as well as the conceptual models that describe the transport and mixing processes for biological/chemical processes to simulate phytoplankton growth, cycling of nutrients and particulate materials are also incorporated into the DLM-WQ.

The simultaneous field measurement of wave/current and turbidity data conducted by Chung et al. (2009) provided direct evidence that showed the peaks of wind speed, wave height peaks and turbidity coincided, and therefore concluded that the bed shear stress exerted by surface waves is the most significant force to cause sediment resuspension events in shallow, wind-exposed lake. Furthermore, Chung et al. (2009) found a novel relationship that turbidity was nonlinearly proportional to wind speed. The researchers also developed a reasonably robust relation between turbidity

and the backscatter intensity of the acoustic wave and current profiler (AWAC) (Chung, Bombardelli, and Schladow 2009a).

Four different sediment resuspension models for non-cohesive and cohesive sediments were tested and evaluated using statistical and graphical methods in the subsequent study by the same research group. The results showed that the extended version of the Garcia and Parker model was most successful in simulating both seasonal trends and the short-term variation of most of the water quality variables compared to the other models that do no adapt to specific sediment characteristics (Chung, Bombardelli, and Schladow 2009b). Overall, the research confirmed that sediment-resuspension induced nutrient cycling are of critical importance in the Salton Sea.

3.2 Introduction

3.2.1 Computation of bed shear stress

Chung et al. (2009) conducted a 4-month field measurement program (4 August to 29 November 2005) to collect the following data in synchronization at the Salton Sea: currents and waves, water temperature, turbidity (surrogate for suspended sediment concentration), and water temperature. In order to quantify the contributions of various forces on sediment resuspension in the lake, characterization of bed shear stress due to waves and currents are discussed in this study. What follows is the descriptions of bed shear stress caused by wind-induced currents and waves and the critical shear stress estimation, respectively.

Equation 3.2.1 presents the current-induced bottom shear stress (τ_{curr}) is estimated by 10% of wind-induced surface shear stress (τ_0), which is estimated by drag coefficient (C_D), air density (ρ_a) and wind velocity (w_{10}) by a quadratic drag low:

$$|\tau_{curr}| = 0.1\tau_0 = 0.1C_D\rho_a w_{10}^2 \quad (3.2.1)$$

where $C_D = 0.001(0.75 + 0.067w_{10})$, and w_{10} denotes the wind velocity at 10 m above the surface water.

The bottom shear stress exerted by wind-induced waves (τ_{wave}) is estimated by Equation 3.2.2:

$$|\tau_{wave}| = 0.5\rho f_W U_W^2 \quad (3.2.2)$$

where ρ is the water density; f_W is the bottom friction factor; U_W is the amplitude of the wave orbital velocity, and can be calculated using wave height (H_W), period (T_W), length of wave (L_W), and water depth (H) based on the small-amplitude wave theory as $U_W = \frac{H_W\pi}{T_W \sinh\left(\frac{2\pi H}{L_W}\right)}$; the estimation of bottom friction factor is inversely related to the square root of wave Reynolds number (R_W), $f_W = \frac{2}{\sqrt{R_W}}$ (valid for the viscous-dominated regime where $R_W \leq 10^4$); and $R_W = \frac{U_W A_W}{\nu}$; ν is the kinematic viscosity of water; A_W denotes the maximum displacement of the individual fluid particles from their mean position, and is calculated by U_W and wave angular frequency (ω) that is related to wave period as $A_W = \frac{U_W}{\omega}$; $\omega = \frac{2\pi}{T_W}$.

The critical bottom shear stress, τ_{cr}, is estimated by the products of critical (nondimensional) Shield's parameter (τ_c^*), water density (ρ), submerged specific

gravity (R), acceleration of gravity (g), and sediment grain size (D) shown in Equation 3.2.3:

$$\tau_{cr} = \tau_c^* \rho RgD \quad (3.2.3)$$

Equation 3.2.4 shows the relationship between critical Shield's parameter and particle Reynolds number (Re_p) developed by Parker et al. (2003) and Park (2004) based on experimental dataset for incipient sediment motion done by Shields (1936):

$$\tau_c^* = [0.22Re_p^{-0.6} + 0.06\ 10^{(-7.7Re_p^{-0.6})}] \quad (3.2.4)$$

where particle Reynolds number is calculated by $Re_p = \sqrt{gRD^3/\nu}$

(Shields 1936)(Parker et al. 2003)(Parker 2004).

The computation results indicated that the shear stresses induced by currents are insignificant compared to induced by waves, and the critical bottom shear obtained for a sediment size of 25 μm was 6.25 x 10^{-2} N/m^2. The results showed that the bed shear stresses would succeed the critical shear stress when the wind speeds were above 7 m/s.

In addition to using the observed wave characteristics to compute the bed shear stress, a wave theory for shallow water bodies, Sverdrup-Munk-Bretschneider (SMB) method, was also used to calculate wave characteristics. The results showed that for a given values of wind spend and fetch, the modeled wave heights agreed reasonably well with the observed values, but wave period showed large scatter compared to the measured data. Nonetheless, the bed shear stress calculated using the measured wave characteristics and that calculated by the SMB model had good agreement in computed

bed shear stresses results above the critical shear stress level (Chung, Bombardelli, and Schladow 2009a).

3.2.2 Sediment resuspension formulations

In the first version of DLM-WQ applied on the Salton Sea, the sediment-resuspension was estimated based on an empirical model of (Somlyody 1986):

$$E = kw^{l} \tag{3.2.5}$$

where the sediment-resuspension rate, (E, g/m^2/s) is as a function of wind speed (w, m/s) and calibration parameters, k and l (Chung et al. 2008).

Later on, Chung et al. (2009) investigated three additional sediment resuspension models that are associated with calculated bed shear stresses based on estimated wave characteristics (height and periods) of the Salton Sea. Among the four sediment resuspension models, this study tested two cohesive sediment models for sediment erosion rates associated with the excess bed shear stress by a power law relationship using Equation 3.2.6 and Equation 3.2.7:

$$E = \alpha\left[\frac{\tau_b - \tau_{cr}}{\tau_{cr}}\right]^{m} \qquad for\ \tau_b \geq \tau_{cr} \tag{3.2.6}$$

$$E = 0 \qquad for\ \tau_b < \tau_{cr} \tag{3.2.7}$$

where E is the specific rate of entrainment of sediment (mass/area/time), τ_b is the bottom shear stress, τ_{cr} is the critical shear stress for sediment erosion, α is a coefficient. The first is a linear model when the exponent, m, equals to 1 (Hawley and Lesht 1992) (Sanford and Halka 1993)(Mei, Fan, and Jin 1997) (Sanford and Maa 2001)(Gowland et al. 2007), and the other is when m was given as 2 in the equation (Mian and Yanful 2004).

The entrainment rate for non-cohesive sediments that incorporated the distribution of sediment sizes in open-channel flows is given in the following formula by Garcia and Parker (M. H. Garcia and Parker 1991)(M. Garcia and Parker 1993) (Glenn et al. 1999):

$$E_S = \frac{AZ_u^5}{1+\left(\frac{A}{0.3}\right)Z_u^5} \quad (3.2.8)$$

where E_S is the non-dimensional coefficient for bed sediment entrainment into suspension that is expressed in terms of A, a constant (1.3 x 10^{-7}) and Z_u, which is as a function of shear velocity (u_*), sediment settling velocity in still water (w_s), and explicit particle Reynolds number (Re_p) shown in Equation 3.2.9:

$$Z_u = \left(\frac{u_*}{w_s}\right) f(Re_p) \quad (3.2.9)$$

The particle Reynolds number is calculated by $Re_p = \sqrt{gRD^3/\nu}$, with g being acceleration of gravity, D denotes the sediment grain size, v is the kinematic viscosity of water and finally, the submerged specific gravity, $R = (\rho_S - \rho)/\rho$, is expressed in terms of water density (ρ) and sediment density (ρ_S). Parker (1993) extended this formula to calculate sediment size as small as 100 µm with $f(Re_p) = 0.586\ Re_p^{1.23}$ ($1 < Re_p < 3$). The fourth sediment resuspension model tested was this non-cohesive model but is further extended to apply to the small particle size (< 100 µm) of the Salton Sea: $f(Re_p) = a\ Re_p^{3.75}$, with a= 7.6 x 10^{-2}, and valid for $0.4 < Re_p < 1$ (Chung, Bombardelli, and Schladow 2009b).

The results showed that the extended version of the Garcia and Parker model was most successful in simulating both seasonal trends and the short-term variation of

most of the water quality variables, and was able to resolve events of small entrainment rates. The model was applied to assess effects of potential restoration configurations- North Sea combined and South Sea combined- and showed that thermal stratification and summer anoxia persisted longer than it does in the whole Sea, which is associated with suppressed vertical mixing caused by reduced wind fetches for both alternatives. South Sea scenario showed higher NH_4 and Chl *a* among the three configurations because it was subjected to higher sediment resuspension due to relatively high wind speeds and shallower water depth in the southern basin.

The simulation results also suggested that extended and increased anoxia in the hypolimnion in the summer for reduced Sea scenarios resulted in more toxic substances (ammonia (NH_3), and hydrogen sulfide) accumulation near the bottom, and could create more harmful ecological impacts once the stratification is broken (Chung, Bombardelli, and Schladow 2009b).

3.3 Delft3D-WAQ

Delft3D-Water Quality is a multi-dimensional water quality model framework, the Delft3D-WAQ module can solve the advection-diffusion-reaction equation while interacting with the hydrodynamic module-Delft3D-FLOW-, from which the information on flow fields and predefined computational grid are derived.

A wide range of substances that describe the essential chemical composition as well as primary producers and consumers in an aqueous system are available in Delft3D-WAQ as depicted in Figure 26. Delft3D-WAQ categorizes substances in various functional groups, each sub-substance can be selected and combined freely by users to tailor specific aqueous system of interest. The lines between the boxes of functional groups indicate physical, (bio)chemical and biological processes occur within the water column or between the air/water and water/sediment interfaces for the fate and transport of the modelled substances.

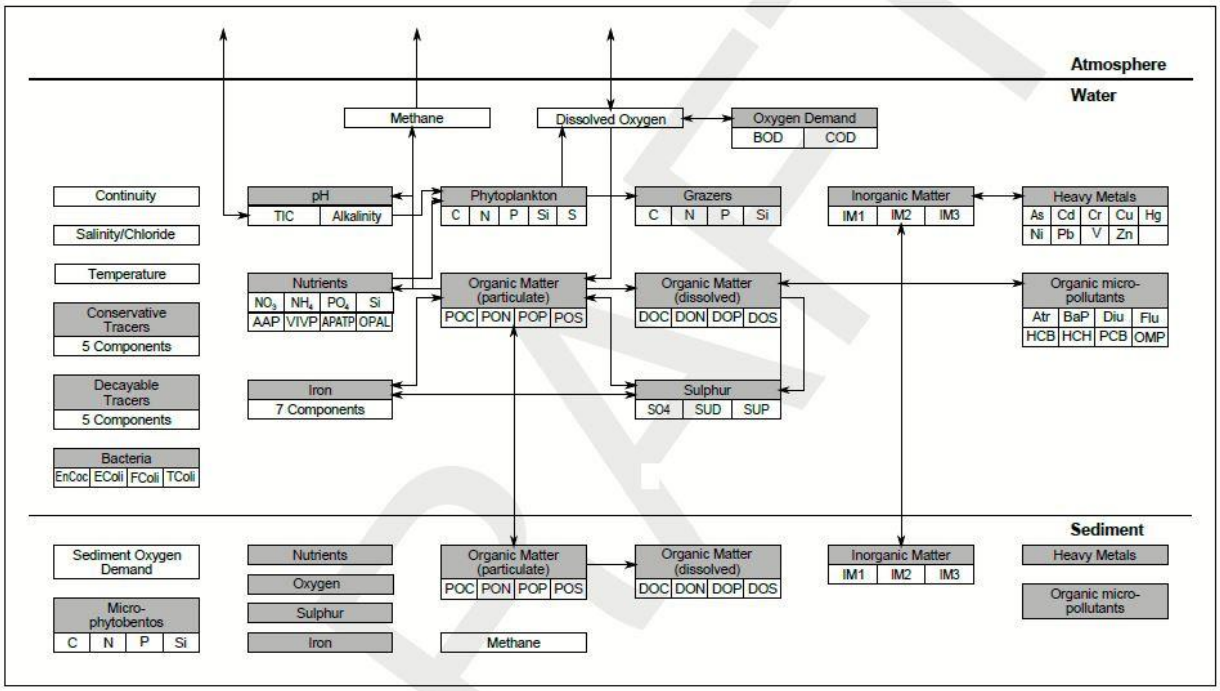

Figure 26. General overview of substances connections and transports via air/water/sediment in Delft3D-WAQ module. The functional groups of substances are in indicated by grey headers, except for those substances that form their own entities. Figure reprinted from "*D-Water Qaulity-Versatile water quality modelling in 1D,2D or 3D systems including physical, (bio)chemical and biological processes",* (p.205), by Deltares. Copyright 2019 by Deltares.

In this work, the main focus is on sediment resuspension activities on nutrient internal loading from sediment to a phosphorus-limiting hypersaline lake. Therefore, functional group of bacteria, micro-phytobentos, heavy metals and organic micropollutants are not included in the water quality simulation of the Salton Sea. The main substances and the processes that are selected to simulate the water quality of the Salton Sea is summarized in Table 9.

Table 9. Summary of substances and processes activated in Delft3D-WAQ module

State Variables	Processes
OXY	Denitrification in water column
	Nitrification
	Reaeration of oxygen
	Oxidation/Mineralization of BOD
	Oxidation of dissolved iron/sulphides/iron sulphides
NH_4	Nitrification
	Mineralization detritus PON
NO_3	Denitrification in water column/sediment
	Nitrification of ammonium
PO_4	Ad(de)sorption ortho phosphorus to inorganic matter
	Mineralization detritus POP
	Dissolution/precipitation of P in vivianite ($Fe_3(PO4)_2$)
	Dissolution/precipitation of apatite-like mineral ($Ca_3(PO4)_2$)
AAP	Ad(de)sorption ortho phosphorus to inorganic matter
	Sedimentation AAP (adsorbed PO4)
Si	Dissolution of Si in opal
H_2S	Sulphide oxidation
	Mineralization
	Speciation of dissolved sulphide
Iron	Precipitation and dissolution of iron(II) and iron (III)
	Formation of pyrite
	Reduction of iron by sulphides
	Oxidation of dissolved iron
	Speciation of dissolved iron
Iron sulphides	Oxidation of iron sulphides
	Sedimentation of iron sulphides/pyrite
	Precipitation and dissolution of iron(II) sulphide
IM1/IM2	Sedimentation
	Resuspension
	Burial
	Digging
Blue Green	BLOOM II algae module
	Sedimentation of algae species
Dinoflagellates	BLOOM II algae module
	Sedimentation of algae species
Marine Diatoms	BLOOM II algae module
	Sedimentation of algae species

The process formulations for critical processes for each state variable shown in Table 9 are described in the following section including *oxygen reaeration, nitrification, denitrification, adsorption of ortho-phosphate, settling of sediment, Transport in sediment and resuspension*, and *grow/mortality* of algae by *BLOOM* module. The formulations described in the following section are derived from the technical reference manual of the Delft3D-WAQ module (Deltares 2014a) .

Reaeration

Oxygen reaeration process is driven by first order process of dissolved oxygen (DO) deficit in the following form:

$$Reaeration\ flux = Rc_{rear} \times (DO_{sat} - [O_2]) \times \vartheta_{rear}^{(T-20)} \quad (3.3.1)$$

in which oxygen deficit is denoted by $(DO_{sat} - [O_2])$, and the first order reaeration rate constant (Rc_{rear} , $\frac{gO_2}{d \cdot m^3}$) is in the function of wind speed, stream velocity, and water depth as follows:

$$klrear = klrear^{20} \times ktrear^{(T-20)} \quad (3.3.2)$$

$$klrear^{20} = \left(\frac{a \times v^b}{H^c}\right) + (d \times W^2) \quad (3.3.3)$$

with:

ϑ temperature coefficients for reaeration = 1.016

a = 3.863, b= 0.5, c= 0.5, d= 0.065 x $klrear^{20}$

$klrear^{20}$ reaeration transfer coefficient at reference temperature 20°C (m/d)

$klrear$ reaeration transfer coefficient in water (m/d)

v flow velocity (m/s)

H depth of the water column (m)

W wind speed at 10 m height (m/s)

The reaeration transfer relation was validated for rivers, lakes, seas and estuaries by WL/Delft Hydraulics (1980b), and the coefficients were used in modeling studies for the Dutch lakes by the WL/Delft Hydraulics.

Nitrification

Under aerobic condition, nitrification can take place that converts ammonium (NH_4^+) to nitrate (NO_3^-). The stoichiometry of the reaction is ($NH_4^+ : O_2 : NO_3^- = -1:-4.571:1$), indicating that removing one gram of N from ammonia requires 4.57 gram of oxygen (gO_2/gN) shown in the following reaction equation:

$$NH_4^+ + 2O_2 + H_2O \rightarrow NO_3^- + 2H_3O^+ \quad (3.3.4)$$

The nitrification process is carried out based on equation (3.3.5):

$$Nitrification\ flux = -R_{nit} \times [NH_4^+] \times \vartheta_{nit}^{(T-20)} \times \frac{[O_2] - DO_{nit}^{Cr}}{DO_{nit}^{Opt} - DO_{nit}^{Cr}} \quad (3.3.5)$$

in which the nitrification rate ($R_{nit,}\ \frac{gN}{d \cdot m^3}$) is dependent on temperature and oxygen concentration in the sum of a zeroth and a first order process:

$$R_{nit} = k0_{nit} + f_{ox} \times k1_{nit} \times [NH_4^+] \quad (3.3.6)$$

$$k1_{nit} = \begin{cases} {k1_{nit}}^{20} \times {kt_{nit}}^{(T-20)} \\ 0.0 \qquad\qquad if\ T < T_C \end{cases} \quad (3.3.7)$$

With:

$k0_{nit}$ zeroth order nitrification rate ($\frac{gN}{d \cdot m^3}$)

$k1_{nit}$ first order nitrification rate (d^{-1})

kt_{nit} temperature coefficient for nitrification (-) = 1.07

f_{ox} the oxygen limit function (-)

T temperature (°C)

T_C critical temperature (°C) = 3 °C

When the water temperature drops below 3 ^{o}C , zeroth order flux with 0 $\frac{gN}{d \cdot m^3}$ would take place. On the other hand, first order flux is modified by the oxygen limit function that is in the range of 0 to 1 depend on oxygen concentrations. When the oxygen concentration is higher than optimal oxygen concentration (5 mg/L), f_{ox} equals to 1; when lowering than critical level (1 mg/L), f_{ox} equals to 0. The oxygen function is determined by linear interpolation for intermediate oxygen concentrations.

Denitrification

In the absence of oxygen microbial denitrifiers carry out the denitrification process reduces nitrate (NO_3^-) into elemental nitrogen (N_2). The reaction can occur in both water and sediment layers, and the overall reaction equation reads:

$$4NO_3^- + 4H_3O^+ \rightarrow 2N_2 + 5O_2 + 6H_2O \quad (3.3.8)$$

Equation (3.3.8) suggested that denitrification reaction produces 2.86 gram of oxygen per gram nitrogen (2.86 gO_2/gN).

The denitrification flux (R_{den}, $\frac{gN}{d \cdot m^3}$) is highly sensitive to temperature and is also corrected for oxygen concentrations as shown in Equations (3.3.9) (3.3.10)

$$R_{den} = k0_{den} + f_{ox} \times k1_{den} \times NO_3^- \quad (3.3.9)$$

$$k1_{den} = \begin{cases} {k1_{den}}^{20} \times {kt_{den}}^{(T-20)} \\ 0.0 \qquad\qquad if\ T < T_C \end{cases} \quad (3.3.10)$$

With:

$k0_{den}$ zeroth order denitrification rate ($\frac{gN}{d \cdot m^3}$)

$k1_{den}$ first order denitrification rate (d^{-1})

kt_{den} temperature coefficient for denitrification (-) = 1.07

f_{ox} the oxygen limit function (-)

T temperature (°C)

T_C critical temperature (°C) = 2 °C

When the water temperature drops below 3 °C , no reaction would take place based on the default value zeroth-order reaction. The first order flux is modified by the oxygen limit function that is in the range of 0 to 1 depend on oxygen concentrations just as it does in the nitrification process. However, on the contrary, when the oxygen concentration is lower than optimal oxygen concentration (1 mg/L), f_{ox} equals to 1; when higher than critical level (3 mg/L), f_{ox} equals to 0. The oxygen function is determined by linear interpolation for intermediate oxygen concentrations.

Adsorption of ortho-phosphate

The fine sediment fraction (clay and silt) determines the adsorption capacity of ortho-phosphate (PO_4^-) in the sediment. The absorbing components that consist of more than 90% within the fine sediment include iron (III)oxyhydroxides, aluminum hydroxides, silicates, manganese oxides and organic matter. As the results, phosphate adsorption is highly pH dependent as the mechanism involves phosphate group competes PO_4^- with OH^- group for the adsorption sites. In addition, since the level of oxygen concentrations determines the conversion between iron (III) and iron (II), which in turn determines the adsorption capacity of the sediment particles.

Iron (III) tends to accumulate in the oxidizing sediment top later, therefore the phosphate sorption capacity is large. The sorption capacity decreases as the sediment layer goes deeper (i.e. become reducing condition), and that most iron would be reduced to iron (II) form under anaerobic condition. When the organic matters in the oxidizing top sediment layer undergo decomposition, the phosphate would be release

from sediment to the overlying water, causing an order of magnitude of phosphate increase in the water column.

The pH, DO and temperature dependent adsorption formulation is used to calculate the sorption flux of phosphate concentrations as shown in Equation (3.3.11):

Comprehensive Langmuir adsorption

$$ADS(OH)_a + P \leftrightarrow ADSP + a\ OH \quad (3.3.11)$$

$$K_{ads} = \frac{C_{pha_e} \times OH^a}{C_{phd_e} \times C_{ads_e}} \quad (3.3.12)$$

$$K_{ads} = {K_{ads}}^{20} \times ktads^{(T-20)} \quad (3.3.13)$$

$$OH = 10^{-(14-pH)} \quad (3.3.14)$$

a	stochiometric reaction constant
C_{ads_e}	equilibrium concentration of free adsorption sites (molFe /L)
C_{pha_e}	equilibrium adsorbed phosphate concentration (molP /L)
C_{phd_e}	equilibrium dissolved phosphate concentration (molP /L)
K_{ads}	adsorption equilibrium constant [$(mol/L)^{a-1}$]
k_{tads}	temperature coefficient for adsorption (-)
OH	molar hydroxyl concentration (mol/L)
pH	acidity
e	index for the chemical equilibrium value

Equation (3.3.13) shows that adsorption equilibrium constant is modified by temperature coefficients for adsorption and is dependent on adsorption capacity from water acidity and the total iron fraction in suspended inorganic sediment (C_{ads_e}).

To estimate the availability of free adsorbent, Equation (3.3.15) shown below describes that the total adsorbent concentration (C_{adst}) is proportional to the reactive iron (III) fraction within the concentration of inorganic matters (1= fine particles, 2=

coarser particles). Furthermore, since the total reactive iron (III) fraction is dependent on the redox condition of the water/sediment layer, the critical oxygen constraints are expressed by correction factors:

$$C_{adst} = fcor \times \sum_{i=1}^{2}(ffe_i \times C_{im_i}) \times \frac{1}{56{,}000 \times \emptyset} \quad (3.3.15)$$

$$fcor = 1.0 \quad \text{if } C_{ox} \geq C_{oxc} \times \emptyset$$

$$fcor = ffeox \quad \text{if } C_{ox} < C_{oxc} \times \emptyset$$

$$fim_i = (ffe_i \times C_{im_i}) / \sum_{i=1}^{2}(ffe_i \times C_{im_i}) \quad (3.3.16)$$

C_{adst} total molar concentration of adsorption sites (molFe /L)
C_{im_i} concentration of inorganic matter fractions i=1,2 (gDW/m^3)
C_{ox} dissolved oxygen concentration (g/m^3)
C_{oxc} critical dissolved oxygen concentration (g/m^3)
f_{cor} correction factor for the oxidized iron (III) fraction
f_{im_i} fraction of adsorbed phosphate bound to inorganic matter fractions i=1,2
ff_{e_i} fraction of reactive iron in inorganic matter fractions i=1,2(gFe/gDW)
ff_{eox} fraction of oxidized iron (III) in the reactive iron fraction
$\emptyset$ porosity

The equilibrium concentrations of adsorbed phosphate concentration are approximated with Equations (3.3.17) (3.3.18) (3.3.19):

$$C_{pha_e} + C_{phd_e} = \frac{(C_{pha} + C_{phd})}{31{,}000 \times \emptyset} \quad (3.3.17)$$

$$C_{ads_e} = C_{ads} = C_{adst} - \frac{C_{pha}}{31{,}000 \times \emptyset} \quad (3.3.18)$$

$$C_{pha_e} = \frac{(C_{pha} + C_{phd})}{31{,}000 \times \emptyset \times (1 + \frac{OH^a}{K_{ads} \times C_{ads}})} \quad (3.3.19)$$

C_{ads} the concentration of free adsorption sites after the previous time-step (molFe /L)

C_{pha} the adsorbed phosphate concentration after the previous time-step (gP /m^3)

C_{phd} the dissolved phosphate concentration after the previous time-step (gP /m^3)

e index for chemical equilibrium value

The sorption rate is calculated as shown in Equation (3.3.20):

$$R_{sorp} = k_{sorp} \times (31{,}000 \times \emptyset \times C_{pha_e} - C_{pha}) \quad (3.3.20)$$

where k_{sorp} denotes sorption reaction rate (d^{-1}).

Settling of sediment

Inorganic matter, organic detritus, and algae biomass are subject to settling, and the settled substances become the sediment inorganic pool and part of sediment oxygen demand. The settling flux is calculated by the sum of zero-order and first-order kinetics as shown in (Eq. 3.3.21) and (Eq. 3.3.22):

If $H < H_{min}$ $F_{set_i} = 0$ else

$$F_{set_i} = \min (F_{set_i}', \frac{C_{x_i} \times H}{\Delta t}) \quad (3.3.21)$$

$$F_{set_i}' = F_{set0_i} + s_i \times C_{x_i} \quad (3.3.22)$$

If $\tau = -1.0$ $f\tau = 1.0$ else

$$f\tau_i = \max (0.0, \left(1 - \frac{\tau}{\tau_{c_j}}\right)) \quad (3.3.23)$$

$$R_{set_i} = f\tau_i \times \frac{F_{set_i}}{H} \quad (3.3.24)$$

when the water depth is lower than the determined minimal water depth ($H_{min} = 0.1$), as well as when the shear stress exceeds the critical shear stress, the setting rates become zero. Otherwise, the settling flux is determined by the products of individual substance concentration and the settling velocity of each substance in addition to the zero-order settling flux of a substance.

C_x	concentration of a substance (g DM/m^3)
F_{set_0}	zero-order settling flux of a substance (g DM/m^2.d)
F_{set}	settling flux of a substance (g DM/m^2.d)
$f\tau$	shear stress limitation function
H	depth of the water column
H_{min}	minimal depth of the water column for resuspension (m)
R_{set}	settling rate of a substance (gDM.m^{-3}.d^{-1})
s	settling velocity of a substance (m.d^{-1})
τ	shear stress (Pa)
τ_c	critical shear stress for suspension (Pa)
Δt	timestep in DELWAQ (d)
i	index for substance (*i*)

The settling velocity of a substance i is modified by temperature coefficient, salinity and concentration function dependencies of flocculation (Eq. 3.3.25).

$$s_i = f_{temp} \times f_{sal} \times f_{con} \times s0_i \quad (3.3.25)$$

$$f_{temp} = kt^{(T-20)} \quad (3.3.26)$$

$$f_{con} = (\frac{C_s}{C_{sc}})^{ni} \quad (3.3.27)$$

$$f_{sal} = \frac{(a_i+1)}{2} - \frac{(a_i-1)}{2} \times cos\frac{(\pi \times S)}{S_{max}} \quad (3.3.28)$$

where

a	coefficient for the enhancement of flocculation
C_s	concentration of total suspended solids (gDM m^{-3})
C_{sc}	critical concentration of total suspended solids above which flocculation occurs (gDM.m^{-3})
f_{con}	function for the concentration dependency of flocculation
f_{sal}	function for the salinity function dependency of flocculation
f_{temp}	function for temperature dependency of settling
kt	temperature coefficient for settling (water density correction)
n_i	constant for concentration effect on flocculation

S salinity (g/kg)

S_{max} salinity at which the salinity function is at its maximum (g/kg)

T water temperature (°C)

i index for substance (*i*)

Transport in sediment and resuspension

Sediment layers are modeled in the DELWAQ module using the two layers -S1 and S2- approach. The sediment layers are subject to resuspension, burial and digging processes; sediment components are released into the water column by resuspension (erosion) activity (S1 and/or S2), sediment components are transported to deeper layer (S1 to S2), or removal to even deeper sediment (S2 to boundary) by burial activity, and lastly, digging transports sediment components from boundary to S2, and from layer S2 to S1. The sediment components included in this study include inorganic sediment and particulate organic detritus.

Resuspension

The resuspension flux of sediment components is calculated as the sum of zero-order and first-order kinetic with constraints of critical water depth and dry matter concentrations as shown in Equation (3.3.29):

$$Fres'_j = f\tau_j \times (Fres0 + r \times \frac{C_{dm_j}}{A}) \quad (3.3.29)$$

If $H < Hmin$ $\quad Fres'_j = 1.0$ else

$$Fres_j = \min\,(Fres'_j, \frac{C_{dm}}{A \times \Delta t}) \quad (3.3.30)$$

The formulation indicates that there would be no resuspension flux from the S2 layer as long as there are available dry matter in the top sediment layer:

If $DMS1 > 0.0 \quad FresS2 = 0.0$

The relationship between resuspension flux and shear stress follows from:

If $\tau = -1.0 \qquad f\tau = 1.0 \qquad$ else

$$f\tau_j = \max\left(0.0, \left(\frac{\tau}{\tau_{c_j}} - 1.0\right)\right) \tag{3.3.31}$$

in which the formulation shows that when the shear stress doesn't exceed the critical shear stress, the shear stress limitation function become zero. In addition, it is assumed that the mass in upper layer (S1) would be completely resuspended before the lower layer (S2) become in contact of bottom shear stress. Thus, resuspension from the second layer (S2) only take place if no mass is available in the upper layer (S1).

S1	top sediment layer
S2	second sediment layer
A	surface area of overlying water compartment (m^2)
C_{dm}	amount of sediment dry matter (gDM)
$Fres0$	zero-order resuspension flux of sediment ($gDM.m^{-2}.d^{-1}$)
Fres	resuspension flux of sediment ($gDM.m^{-2}.d^{-1}$)
$f\tau$	shear stress limitation function
H	depth of the water column, thickness overlying water layer (m)
$Hmin$	minimal depth of the water column for resuspension (m)
r	first-order resuspension rate (d^{-1})
τ	shear stress (Pa)
τ_c	critical shear stress for suspension (Pa)
Δt	timestep in DELWAQ (d)
j	index for sediment layer S1 or S2

The resuspension flux of individual sediment components including inorganic matter, organic carbon/nitrogen/phosphorus, silicate and adsorbed phosphate is

estimated based on its individual fraction in the sediment dry matter according to Equation (3.3.32)

$$Rres_{i,j} = fs_{i,j} \times fr_{i,j} \times Fres_j / H \quad (3.3.32)$$

fr	fraction of a component in sediment dry matter (gX. gDM^{-1})
fs	scaling factor (-)
$Rres$	resuspension rate of a component ($gX.m^{-3}.d^{-1}$)
i	index for component i
j	index for sediment layer S1 or S2

Burial

Burial is the downward movement of particulates within the sediment layers. The sum of zero-order and first-order kinetics for burial flux is chosen to calculate burial fluxes as shown in Equation 3.3.33-37:

$$Fbur_j = \min\left(\left(Fbin_j + Fbad_j\right), Fbmax_j\right) \quad (3.3.33)$$

$$Fbin_j = Fbur0_j + rb_j \times Cdm_j / A \quad (3.3.34)$$

$$Fbad_j = \max\left(0, \frac{(Z_j - Zmax_j) \times \rho_j \times (1 - \emptyset_j)}{\Delta t}\right) \quad (3.3.35)$$

$$Fbmax_j = Fin_j - Fout_j + \frac{Cdm_j}{A \times \Delta t} \quad (3.3.36)$$

$$Cdm_j = A \times Z_j \times \rho_j \times (1 - \emptyset_j) \quad (3.3.37)$$

$$F_{in_1} = F_{set}$$

$$F_{in_2} = F_{bur_1}$$

$$F_{out_1} = F_{res_1}$$

$$F_{out_2} = F_{dig_1}$$

For the uppermost layer (S1), the influx to S1 layer is same as the settling flux from the water column, and the outflux of sediment is essentially the resuspension flux from the S1 layer. For the lower layer (S2), the influx to S2 layer is the burial flux from S1 layer, and the outflux of the sediment from S2 to S1 layer is carried out by the digging flux.

C_{dm}	amount of sediment dry matter (gDM)
F_{bad}	additional burial flux to obey maximal layer thickness (gDM.m^{-2}.d^{-1})
F_{bin}	burial flux of sediment based on input parameters (gDM.m^{-2}.d^{-1})
F_{bmax}	maximal possible burial based on available sediment (gDM.m^{-2}.d^{-1})
F_{bur0}	zero-order burial flux of sediment (gDM.m^{-2}.d^{-1})
F_{bur}	burial flux of sediment (gDM.m^{-2}.d^{-1})
F_{dig}	digging flux of sediment (gDM.m^{-2}.d^{-1})
F_{in}	influx of sediment (gDM.m^{-2}.d^{-1})
F_{out}	outflux of sediment (gDM.m^{-2}.d^{-1})
F_{res}	resuspension flux of sediment (gDM.m^{-2}.d^{-1})
F_{set}	setting flux of sediment (gDM.m^{-2}.d^{-1})
rb	first-order burial rate (d^{-1})
Z	actual thickness of sediment layer (m)
$Zfix$	fixed thickness of sediment layer (m)
$\emptyset$	porosity
ρ	density of sediment dry matter (g.m^{-3})
Δt	timestep in DELWAQ (d)
j	index for sediment layer S1 or S2
A	surface area of overlying water compartment (m^2)

The burial of sediment components including inorganic matter, organic carbon/nitrogen/phosphorus, silicate and adsorbed phosphate follows from Eq. 3.3.38 and Eq. 3.3.39:

$$F_{bur_{i,j}} = fs_{i,j} \times fr_{i,j} \times F_{bur_j} \quad (3.3.38)$$

$$R_{bur_{i,j}} = F_{bur_{i,j}}/H \quad (3.3.39)$$

where the burial rate of the individual particulate fractions in the sediment layer is proportional to its weight fraction, described by its specific fraction in sediment dry matter and scaling factor.

fr	fraction of a component in sediment dry matter (gX.gDM^{-1})]
fs	scaling factor
H	depth of the water column, thickness overlying water layer (m)
F_{bur}	burial flux of sediment (gDM.m^{-2}.d^{-1})
R_{dig}	digging rate of a component (gX.m^{-3}.d^{-1})
i	index for component i
j	index for sediment layer S1 or S2

Digging

Digging is the upward movement of particulates within the sediment layers. The digging fluxes of sediment of each layer are calculated using a zero-order kinetics as shown in Eq. 3.3.40 and Eq. 3.3.41:

$$F_{dig_j} = \min\left(F_{dig0_j}, F_{dmax_j}\right) \quad (3.3.40)$$

$$F_{dmax_1} = \frac{Cdm_2}{A \times \Delta t} \quad (3.3.41)$$

$$F_{dmax_2} = \infty \quad (3.3.42)$$

$$Cdm_2 = A \times Z_2 \times \rho_2 \times (1 - \emptyset_2) \quad (3.3.43)$$

The equation shows that digging flux of layer S1 depends on the mass of sediment dry matter in layer S2, and since the S1/S2 approach assumes that deeper sediment layer below layer S2 is the defined by means of the concentrations of the components in the boundary layer, the digging flux from the boundary layer then becomes infinity.

C_{dm}	amount of sediment dry matter (gDM)
F_{dig}	digging flux of sediment (gDM.m^{-2}.d^{-1})
F_{dig0}	zero-order digging flux of sediment (gDM.m^{-2}.d^{-1})
F_{dmax}	maximal possible digging based on available sediment (gDM.m^{-2}.d^{-1})
Z	actual thickness of sediment layer (m)
ρ	density of sediment dry matter (g.m^{-3})
Δt	timestep in DELWAQ (d)
j	index for sediment layer S1 or S2
A	surface area of overlying water compartment (m^2)

The digging of individual sediment components including inorganic matter, organic carbon/nitrogen/phosphorus, silicate and adsorbed phosphate is dependent on the quality of the underlying layer as shown in Equation 3.3.44:

$$F_{dig_{i,j}} = fs_{i,j+1} \times fr_{i,j+1} \times F_{dig_j} \quad (3.3.44)$$

and the digging rate of a component in the sediment layer is proportional to its weight fraction.

$$R_{dig_{i,j}} = F_{dig_{i,j}}/H \quad (3.3.45)$$

fr	fraction of a component in sediment dry matter (gX.gDM^{-1})]
fs	scaling factor
H	depth of the water column, thickness overlying water layer (m)
F_{dig}	digging flux of a component (gX.m^{-2}.d^{-1})
R_{dig}	digging rate of a component (gX.m^{-3}.d^{-1})
i	index for component i
j	index for sediment layer S1 or S2

Nutrient constraints

The nutrient balance shown in Eq. 3.3.46 indicates that the total available nutrient concentrations (N,P,Si) are the sum of dissolved inorganic nutrient k (k= N,P,Si) in the water column, and the nutrients in the composition of phytoplankton, subtracted by the minimal available concentrations of dissolved N, P and Si.

$$Ctnut_k = Cnut_k + \sum_{i=1}^{n}\left(anut_{k,i} \times Calg_i \right) - Cnutc_k \quad (3.3.46)$$

$Ctnut_k$	concentration of total available nutrient k (gN/P/Si m^{-3}) ;
$Cnut_k$	concentration of dissolved inorganic nutrient k (gN/P/Si m^{-3})
$anut_{k,i}$	stochiometric constant of nutrient k originating from dissolved inorganic nutrient over organic carbon in algae biomass (gN/P/Si gC^{-1});
$Calg_i$	algae biomass concentration (gC/m^3)
$Cnutc_k$	threshold concentration of dissolved inorganic nutrient k (gN/P/Si m^{-3})
i	index for algae species
k	index for nutrients, 1= nitrogen, 2= phosphorus, 3 = silicon
n	number of species types

The above constraint also requirements that $Calg_i \geq 0.0$ and $Cnut_k \geq 0.0$

Energy constraints (light)

The constraint of solar radiation is defined by the net phytoplankton growth rate compensates the sum of respiration and mortality rates. As the results, when self-shading causing the total light extinction exceeds the critical value of no net growth, energy in light becomes limiting.

The maximum extinction coefficient is derived from critical light intensity (total available amount of light) within the water column and at the surface layer using a depth

integrated law of Lambert-Beer equation (equation not shown). The critical light efficiency is expressed by the sum of specific maintenance respiration rate ($krsp_i$) and specific mortality rate ($kmrt_i$) divided by specific growth rate as shown in Eq. 3.3.47:

$$Efc_i = \frac{(krsp_i + kmrt_i)}{kgp_i} \quad (3.3.47)$$

Efc_i critical light efficiency factor (-)
$krsp_i$ specific maintenance respiration rate (d^{-1})
$kmrt_i$ specific mortality rate (d^{-1})
kgp_i specific growth rate (d^{-1})

The specific rates of algal growth, respiration are modified by temperature coefficients individually, and mortality rates are corrected for temperature and salinity stress.

Growth constraints

The growth constraint formulation shown below is applied to all three types of algae (i) - Energy, Nutrient, and Growth limited- within each algae species (j):

$$Calgmax_i = Calg_{1i} \times e^{((k_{gp_i} \times Ef_i - k_{rsp_i}) \times \Delta tb)} \quad (3.3.48)$$

$$Calgmax_j = \sum_{i=1}^{m} (Calgmax_i) \quad (3.3.49)$$

If $Calgmax_j \geq Calgc_j$ Then

$Calgmax_j = Calgmax_j$

If $Calgmax_j < Calgc_j$ Then

$Calgmax_j = 0$

$$\sum_{i=l}^{m} (Calg_{2i} \leq Calgmax_j) \quad (3.3.50)$$

$$\Delta tb = ft \times \Delta t \quad (3.3.51)$$

With

$Calgmax$	maximum concentration of an algae species or type at time t_2 , the end of a timestep (gC/m^3)
$Calgc$	threshold biomass concentration of an algae species at time t_1, the beginning of a timestep (gC/m^3)
$Calg_1$	biomass concentrations of algae species j at time t_1 (gC/m^3)
$Calg_2$	biomass concentrations of algae species j at time t_2 (gC/m^3)
ft	ratio of the BLOOM timestep and the DELWAQ timestep ≥ 1.0
Ef	light efficiency factor ($0 < Ef < 1$)
k_{gp}	potential specific growth rate of the fastest growing type of an algae species (d^{-1})
k_{rsp}	specific maintenance respiration rate of the fastest growing type of an algae species (d^{-1})
Δt	timestep in DELWAQ (d)
Δtb	time interval, the timestep in BLOOM (d)
j	index for algae species
i	index for algae species type
l	index of the first algae type for species j
m	index of the last algae type for species j

The above equations suggest that the maximum increase of the biomass of a species *i* is determined by the initial biomass ($Calg_{1i}$) and the net growth rate ($k_{gp_i} \times Ef_i - k_{rsp_i}$). In addition, if at any time the biomass is lower than minimum biomass ($Calgc$) when the growing condition is unfavorable to the species, the threshold value is used instead, and the growth of another species that thrive in the condition would be enabled.

Mortality constraints

The minimum biomass of a species is defined by the biomass concentration of an algae type *i* with a species modified by only specific mortality rate shown in Equation 3.3.52:

$$Calgmin_i = Calg_{1i} \times e^{(-k_{mrt_i} \times \Delta tb)} \quad (3.3.52)$$

$$Calgmin_j = \sum_{i=1}^{m} (Calgmin_i) \quad (3.3.53)$$

If $Calgmin_j \geq Calgc_j$

Then $Calgmin_j = Calgc_j$

If $Calgmin_j < Calgc_j$

Then $Calgmax_j = 0$

$$\sum_{i=l}^{m} (Calg_{2i} \geq Calgmin_j) \quad (3.3.54)$$

with

$Calgmin$ minimum concentration of an algae species or type at time t_2, the end of a timestep (gC/m^3)

$Calgc$ threshold biomass concentration of an algae species at time t_1, the beginning of a timestep (gC/m^3)

$Calg_1$ biomass concentrations of algae species j at time t_1 (gC/m^3)

$Calg_2$ biomass concentrations of algae species j at time t_2 (gC/m^3)

k_{mrt} specific mortality rate of an algae species type (d^{-1})

The above constrains show that minimum concentration of an algae species ($Calgmin_j$) would not be less than the threshold biomass concentration of an algae species type *i* in any time, so that there wouldn't be a complete removal of an algae species type within a single timestep.

Growth, mortality, and respiration rates

The algae processes are critical to the overall water quality as algal growth, respiration and mortality determines the levels of algae biomass/detritus production, nutrients consumption in an aqueous system. The growth, respiration and mortality rates of each algae species are shown in the following:

$$R_{gr_i} = \frac{(Calg2_i - Calg1_i)}{\Delta tb} \quad (3.3.55)$$

$$R_{gr_{on,i}} = R_{gr_i} \times (an_i + adn_i + aen_i) \quad (3.3.56)$$

$$R_{gr_{op,i}} = R_{gr_i} \times (aph_i + adph_i) \quad (3.3.57)$$

$$R_{gr_{osi,i}} = R_{gr_i} \times asi_i \quad (3.3.58)$$

$$R_{gp_i} = R_{gr_i} + R_{rsp_i} + R_{mrt_i} \quad (3.3.59)$$

$$R_{np_i} = R_{gp_i} - R_{rsp_i} \quad (3.3.60)$$

$$R_{rsp_i} = krsp_i \frac{(Calg_{2i} + Calg_{1i})}{2} \quad (3.3.61)$$

$$R_{mrt_i} = kmrt_i \frac{(Calg_{2i} + Calg_{1i})}{2} \quad (3.3.62)$$

with

$Calg_{1i}$ algae biomass concentrations at time t_1 , the beginning of timestep (gC/m^3)

$Calg_{2i}$ algae biomass concentrations at time t_2 , the end of timestep (gC/m^3)

an stochiometric constant for ammonium/nitrate over carbon in algae biomass (gN/gC)

adn stochiometric constant for detritus nitrogen over carbon in algae biomass (gN/gC)

aen stochiometric constant of nitrogen originating from elemental nitrogen in algae biomass (gN/gC)

aph stochiometric constant for phosphate over carbon in algae biomass (gP/gC)

$adph$ stochiometric constant for detritus phosphorus over carbon in algae biomass (gP/gC)

asi stochiometric constant for silicon over carbon in algae biomass (gSi/gC)

$krsp$ specific respiration rate (d^{-1})

$kmrt$ specific mortality rate (d^{-1})

R_{gp} gross primary production rate ($gC/m^3/d$)

R_{gr} growth rate for organic carbon ($gC/m^3/d$)

$R_{gr_{on}}$ growth rate for organic nitrogen ($gN/m^3/d$)

$R_{gr_{op}}$ growth rate for organic phosphorus ($gP/m^3/d$)

$R_{gr_{osi}}$ growth rate for “organic” silicate ($gSi/m^3/d$)

R_{mrt} mortality rate ($gC/m^3/d$)

R_{np} net primary production rate ($gC/m^3/d$)

R_{rsp} respiration rate ($gC/m^3/d$)

Δtb time interval, the timestep in BLOOM (d)

i index for algae species type 1-3

Algae growth rates are deduced from the change of the algae biomass over a timestep, and the respiration rates as well as mortality rates are estimated by the average of the algae biomass between two timesteps multiplied by specific respiration rate and specific mortality rate, respectively. The growth rates for organic nutrients (N/P/Si) are calculated by growth rate for organic carbon modified by each specific stoichiometric constants shown in Equations (3.3.56) (3.3.57) (3.3.58). Finally, the gross primary production rates are the sum of growth rates (for all nutrients), respiration rates and mortality rates. The net primary production rates are estimated by the gross primary production rates minus respiration rates.

3.4 Methods

3.4.1 Sediment Data

Sediment Characteristics of the Salton Sea

In 1998 Schroeder et al. (2002) chose 11 sites in the Salton Sea that were representative for sediment depositional environment in various depths: shallow (4.6 m), medium (9,) and deep (14-15m). Five shallow sites were located in the delta regions where each of the five perennial river discharges to the Sea in north, northeastern, and south ends. Two medium sites were sampled in the areas between the coalesced deltas of the New and Alamo River and south basin, and between Whitewater River and the north basin. Four deep sampling sites including two deepest areas in the north (15.2 m) and south basins (14.6 m), and two sites that were at 13 m deep contour plan, one in the saddle between the basin, the other near the center of the south basin (Schroeder, Orem, and Kharaka 2002).

The distribution of bottom sediment sizes in three different depth levels from the 11 sites were summarized in Table 10. It was shown that sediment sizes varied in space and in depth: on average shallow regions are predominantly sand particles (53%), silt (40.5%) and clay (42.5%), and showed similar percentage in medium depth. Clay percentage increase as the depth decreases, and shows significantly higher percentage (73.25) than the other sediment types in the deepest depth(Schroeder, Orem, and Kharaka 2002).

Table 10. Grain size (percent by weight) of bottom sediment from the Salton Sea (adapted from Table 1 Schroeder et al. (2002)).

Site no.	Depth (m)	Clay	Silt	Sand
3	4.6	1	1	99
4	4.6	20	27	53
5	4.6	14	10	76
8	4.6	33	33	34
11	4.6	29	68	3
	average	19.4	27.8	53
6	9.1	32	35	33
10	9.1	49	50	1
	average	40.5	42.5	17
1	13.1	62	18	15
9	13.1	64	19	17
7	14.6	86	13	1
2	15.2	81	13	6
average	average	73.25	15.75	9.75

Vogol et al. (2002) conducted a large-scale, two-phases field investigation of the physical and chemical characteristics of sediments in and around the Salton Sea and its main tributaries in December 15-22, 1998 and January 19-22, 1999. The contaminant concentrations and sediment particle size distribution in the bottom sediment were analyzed by grab sampling and core sampling methods; 42 grab sampling sites and six core sampling sites in Phase I, and 15 grab sites and 10 core sites in the target areas in Phase II (Richard A Vogl and Henry 2002).

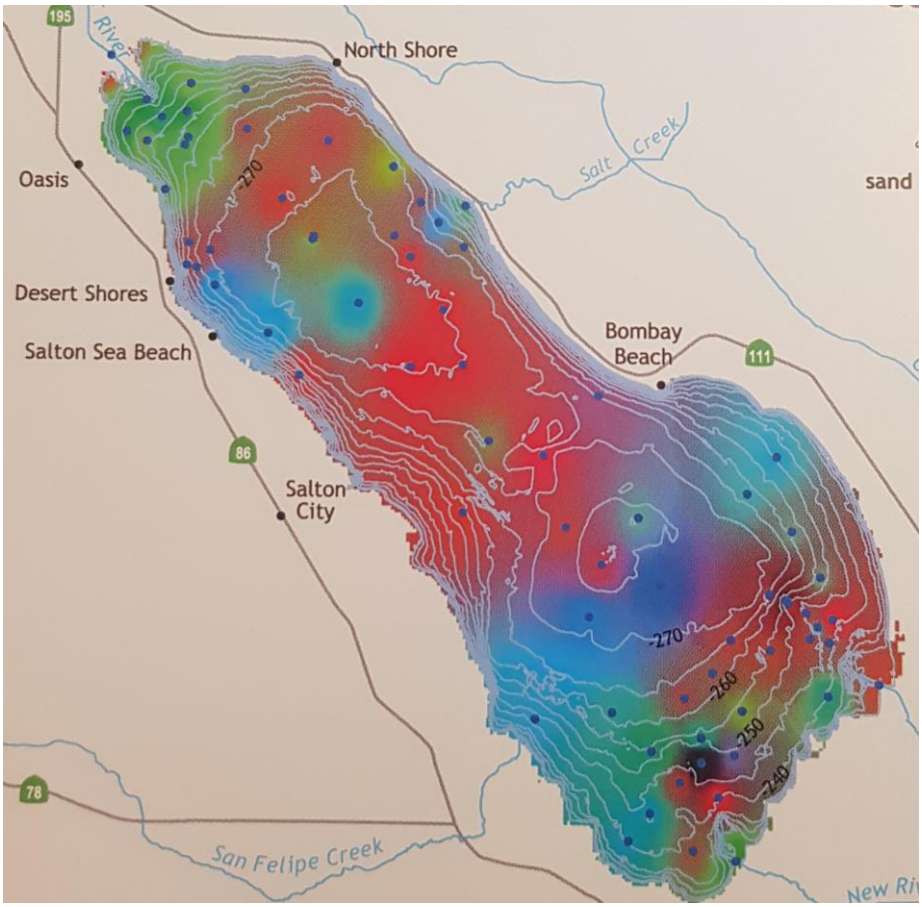

Figure 27. Sediment distribution composition (data collected in 1999) Figure reprinted from "*Salton Sea Atlas*" (p. 94), by Redlands Institue. 2002.

The evaluation results showed that the bottom sediments consisted of silt, clay and finer grained sands, and the distribution of sand, silt, and clay varied in depth and space through the Sea. In general, this study determined that sand percentages are high on the western bank of the Sea, and near the mouths of the New and Alamo River due to the high incoming flow velocity into the Sea. In addition, sand composition in the surface sediment was also high from offshore in the middle region where the bottom floor is higher and extended into the central, deeper parts of the Sea. Whereas, silt was predominantly found in the Whitewater River delta, and in the southwestern shore area near the New and Alamo rivers. The shallow layer of the southwestern corner and

offshore of the Desert Shores was covered in large by clay, and the smallest sized particle extended toward the deepest parts in both north and south sub-basins (Redlands Institue 2002) (Fig.27). The study also suggested that silt and clay were more abundant in the deeper sediment composition sampled from the central and southern parts of the Sea compared to fine sand (R.A. Vogl et al. 1999).

Anderson et al. (2008) conducted a large-scale field sampling in 2001 where sediments were collected in 90 sites located based on a regular, staggered-start sampling grid on the Salton Sea. A Ponar grab sampling method was used to collect the uppermost 5-7 cm of the sediment. The sediment properties and distribution were analyzed and showed the evidence of sediment compositions evolution over the past 45 years since the conditions presented by Arnal (1961) in the study done in January 1955 (Anderson et al. 2008). The average and range of sediment particle size distribution in the Salton Sea was shown in Table 11. This study indicated huge variation within the sediments, but there's a general pattern observed from sediment properties and depth: "excluding % sand and porewater NH_4-N and TDP, sediment properties were positively correlated with depth". In addition, based on organic C content of the sediment, the study provided depths that define the erosional zone (up to ~9 m), transportational zone (9 m to near the maximum depth), and depositional zone (near the maximum depth) (Anderson et al. 2008).

Table 11. Average sediment particle size distribution in the Salton Sea

Particle size distribution %	Anderson et al. (2008)
Sand (63µm - 2mm)	24.1 (0.6-92.5)
Silt (2 µm - 63 µm)	45.4 (0.0-68.1)
Clay ($2e^{-3}$ µm -2 µm)	30.5 (7.2-50.3)

3.4.2 Calibration and Validation

Suspended sediment calibration/validation test (8/8/2005 – 9/17/2005)

Sensitivity tests were conducted to evaluate various parameters effects on suspended sediment concentrations. The period for sensitivity study is from 8/9/2005 00:00 to 8/12/2005 00:00, during which the turbidity peaked at the highest wind speed on 8/10/2005 at 18:00 at the AWAC monitoring site. The parameters for sensitivity test in suspended sedimentation simulation include *sedimentation velocity IM1/IM2, zeroth-order resuspension flux* and *first-order resuspension flux.*

The significance of sedimentation velocity of inorganic matters (IM1=fine particle sized, IM2= medium particle sized) on suspended solids concentrations in the water column is shown in Fig. 28. The simulation results indicated that degree of resuspension activities controlled by the combinations of zeroth-order resuspension flux (ZResDM) and first-order resuspension flux (VResDM) only take place after high wind velocity (9 m/s) occurred on 8/9/2005 (Fig. 28a). Once the shear stress generated by wind calm down after two days, the suspended solids concentration is largely dependent on the imposed sedimentation velocities.

Figure 28 shows that the suspended solids concentrations at 0.5 m off the bottom in depth of 6m. The sedimentation velocity of 0.5 m/d was set for all of the settling matters including IM1/IM2 in Fig. 28a. The simulated results indicated that during the resuspension the sediment concentration could reach up to 14.5 mg/L, and settled at about 9 mg/L. The effect of increasing sedimentation velocity of IM1/IM2 to 1 m/d (while the rest of the settling matters remain to be 0.5 m/d) is shown in Fig. 28b. It is shown that doubling the setting velocity of IM1/2 inhibited the suspended solids be

resuspended to reach higher than the initial value, and once the wind velocity dropped, the suspended solid concentration settled around 3 mg/L in the water column near the bottom.

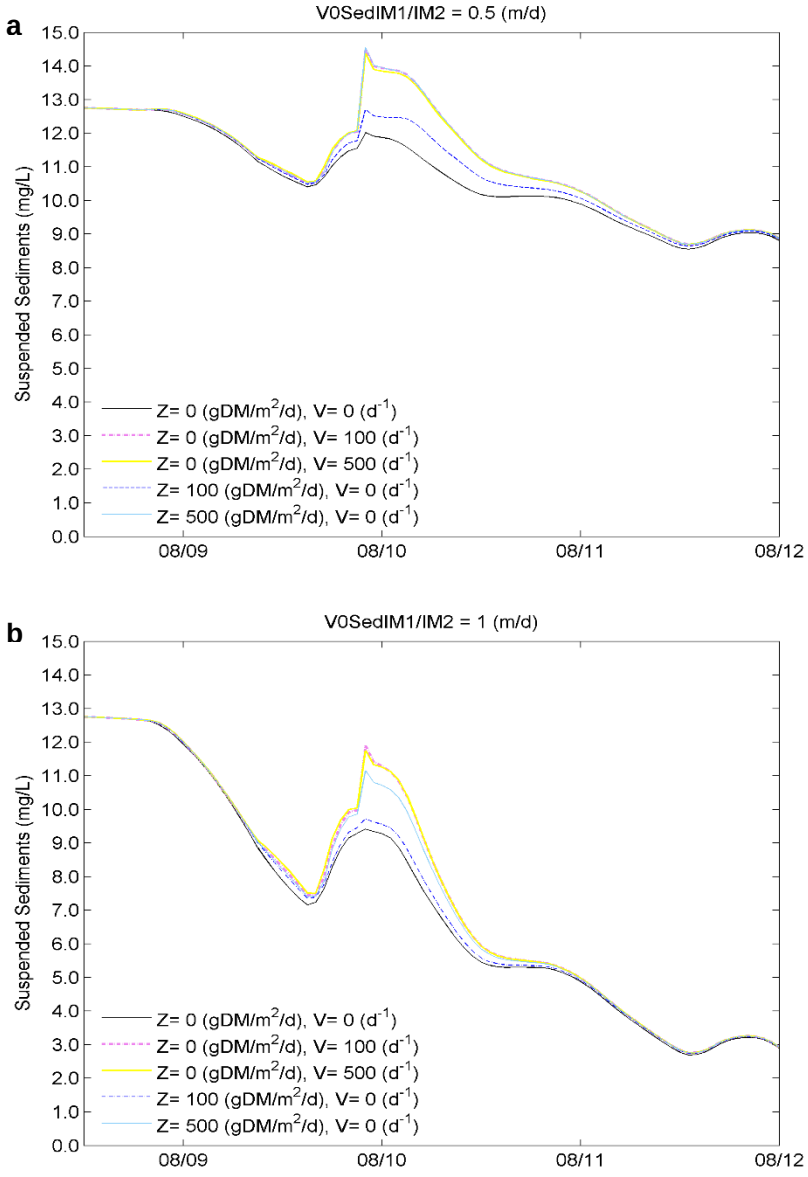

Figure 28. Sensitivity test of the combined effects of various zeroth-order resuspension flux and first order resuspension velocity on suspended sediment concentrations using inorganic matter (IM1/IM2) sedimentation velocity of 0.5 (m/d) (a), and of 1 m/d (b).

The combined effects of ZResDM and VResDM are further investigated using a universal sedimentation velocity of 0.5 m/d of all of the settling matters (inorganic matters, organic C/N/P, silicate, adsorbed phosphate and algae biomass) within the water column during 8/28/2005 to 9/1/2005 (Fig. 29).

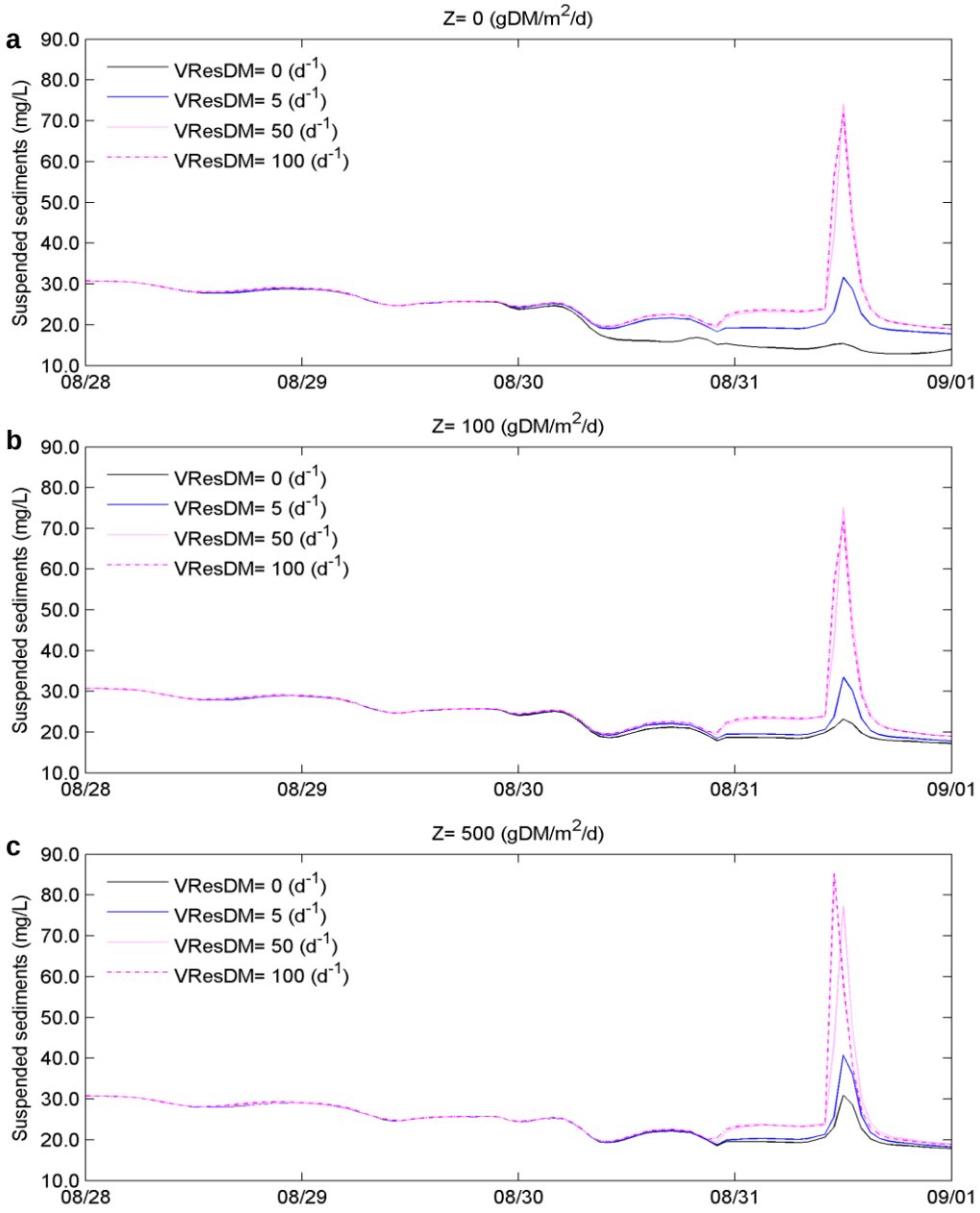

Figure 29. Sensitivity test of the combined effects of various zeroth-order resuspension flux: (a) ZResDM = 0 (gDM/m^2/d), (b) 100 (gDM/m^2/d), and (c) 500 (gDM/m^2/d). and first order resuspension velocity on suspended sediment concentrations using inorganic matter (IM1/2) sedimentation velocity of 0.5(m/d).

Figure 29 shows that the larger the first order resuspension velocity (VResDM), the higher the suspended solids in the water column until it reached the maximal value

available from the bottom. In this case, increasing the resuspension velocity from 50 to 100 d^{-1} had no effect on increasing the suspended solids concentrations higher than approximately 75 mg/L at 0.5 m off from the bottom of water depth of 6m.

Comparing panels a, b and c, it indicates that increasing zeroth order resuspension flux (ZResDM) from 0 to 500 had limited effect on the level of resuspension. At the highest resuspension velocity of 100 d^{-1}, the overall suspended solids only increased approximately 10 mg/L when ZResDM level was increased from100 to 500 gDM/m^2/d.

Further sensitivity test is conducted on the parameters relevant to burial and digging processes under the same condition of initial concentration and sedimentation velocities (Figure 30). Figure 30 a) shows that first order burial velocities (VBurDM) have significant impact on suspended solid concentrations in the water column; imposing the burial velocity of 5 d^{-1} reduced the sediment concentration from 52 to 32 mg/L. On the other hand, zeroth-order digging flux (ZDigDM) = 0 g DM/m^2/d had almost the same effect of that of 10 g DM/m^2/d. Figure 30 b) shows that increasing ZResDM from 0 to 100 gDM/m^2/d only slightly increase the suspended sediment solid concentrations.

Overall, these sensitivity tests suggested that among ZResDM, VResDM , ZDigDM, VBurDM and sedimentation velocities, the parameters of VResDM, VBurDM and Settling velocities play significant roles in determining the level of sediment resuspension events in the water column.

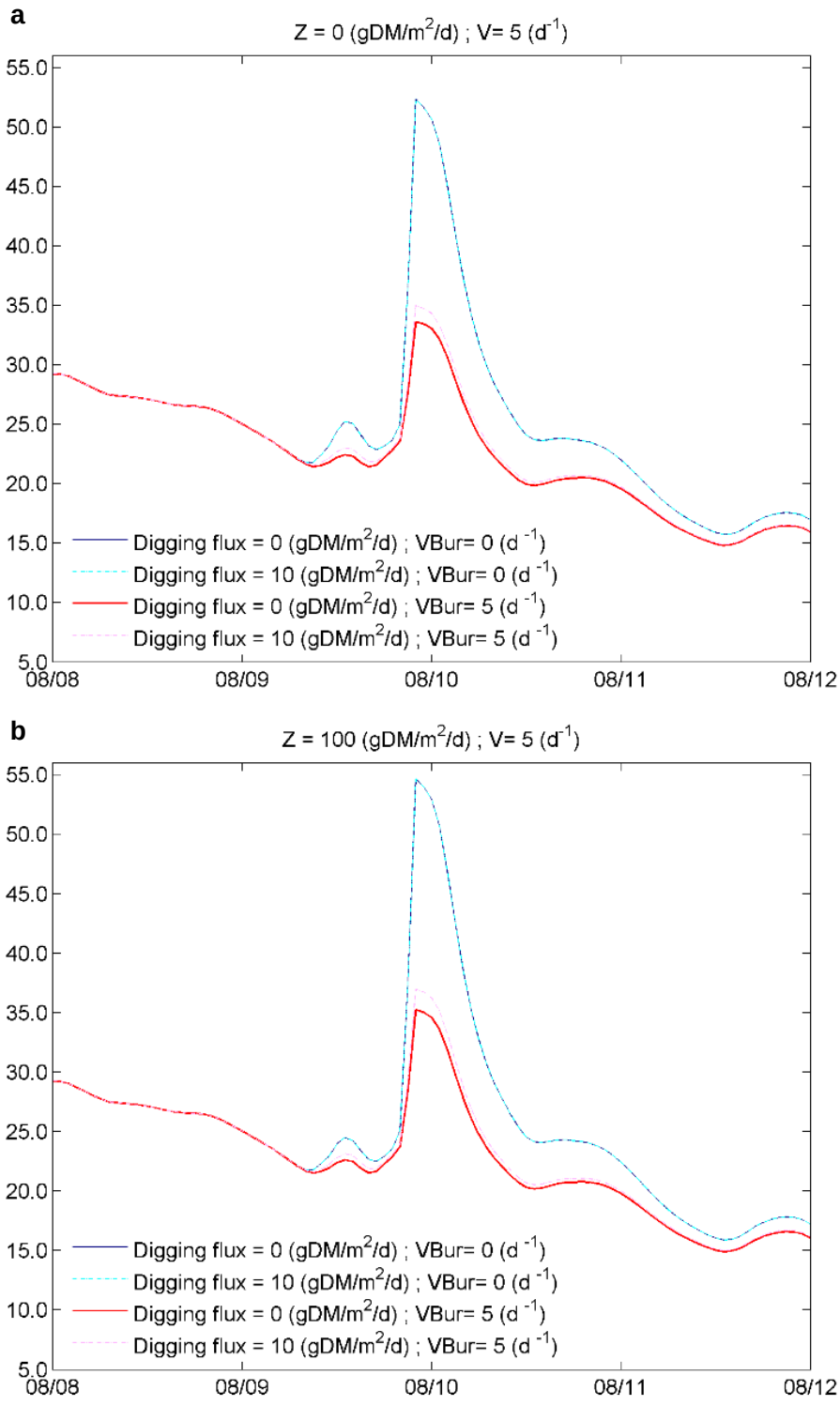

Figure 30. Sensitivity test of the combined effects of various zeroth-order digging flux and first-order burial rates under the conditions of: (a) ZResDM = 0 (gDM/m^2/d); VResDM = 5 (d^{-1}), (b) ZResDM = 100 (gDM/m^2/d); VResDM = 5 (d^{-1}) on suspended sediment concentrations

The warm-up period for the calibration task was from 8/8/2005 00:00:00 to 8/15/2005 00:00:00. The restart file at the last timestep of the warm-up run was used as the initial conditions for the calibration run. The suspended solid concentrations in the water column at the southeastern basin was calibrated against the measured turbidity data from 8/15/2005 00:00 to 9/1/2005 00:00. The overlay of simulated total bottom stress and bottom shear stress caused by waves is shown in Figure 31a. The simulated suspended sediments (mg/L) and the measured turbidity (NTU) data is shown in Figure 31b. Note that the relationship between turbidity and total suspended solids was converted by an equation tested previously on Mark Twain Lake (Knowlton and Jones (1995)): $TSS(mg/L) = 0.932 \times TURB(NTU) + 0.0038 \times TURB^2$. The conversion result in a roughly 1: 1 ratio between turbidity (NTU) and suspended solids concentration (mg/L).

The composition of sediments is summarized in Table12. The constituent concentrations were obtained from the quarterly monitoring program by Burau of Reclamation. Since in 2005 the sampling dates closest to the period of August 8-Sepetmer 17 were from June 21 and September 27, therefore nutrients and particulate organic matter concentrations were derived from the average of the data between June and September. Since the measured inorganic matter concentrations in the surface and bottom of the Salton Sea in June and September were large in range (20 to 144 mg/L), the mode value (~54 mg/L) was selected to carry out the calibration/validation tests. Those marked “modelled” specified the substances which values were derived from water quality processes in the model.

Table 12. Summary of input substance values for Delft3D-WAQ used for suspended sediment calibration/validation test

Substances	Input Name	Unit	Value
Inorganic matter 1	IM1	gDM/m^3	36
Inorganic matter 2	IM2	gDM/m^3	18
Carbonaceous BOD	CBOD5	gO_2/m^3	0
Ammonium	NH4	gN/m^3	0.186
Nitrate	NO3	gN/m^3	0.221
Ortho-Phosphate	PO4	gP /m^3	0.016
Adsorbed ortho phosphate	AAP	gP /m^3	0.012
Vivianite-P	VIVP	gP /m^3	modelled
Apatite-P	APATP	gP /m^3	modelled
Dissolved silica	Si	gSi/m^3	4.6
Opal-Si	Opal	gSi/m^3	14
Total inorganic carbonate	TIC	gC/m^3	248.5
Dissolved organic carbon	DOC	gC/m^3	47
methane	CH4	g/m^3	0.016
Alkalinity	Alka	$gHCO_3/m^3$	201
Sulphate	SO4	gS/m^3	11466
Total dissolved sulphide	SUD	gS/m^3	10
Iron (II) carbonate	FeCO3	gFe/m^3	modelled
Total dissolved reducing iron	FeIId	gFe/m^3	0.03
Dissolved oxidizing iron	FeIIId	gFe/m^3	0.03
Particulate amorphous oxidizing iron	FeIIIpa	gFe/m^3	modelled
Particulate crystalline oxidizing iron	FeIIIpc	gFe/m^3	modelled
Iron(II) sulphide	FeS	gFe/m^3	modelled
Pyrite	FeS2	gFe/m^3	modelled
Fast decomposing fraction particulate organic carbon	POC1	gC/m^3	1.6
Medium decomposing fraction particulate organic carbon	POC2	gC/m^3	0.7

Slow decomposing fraction particulate organic carbon	POC3	gC/m^3	0.1
Fast decomposing fraction particulate organic nitrogen	PON1	gN/m^3	2.7
Medium decomposing fraction particulate organic nitrogen	PON2	gN/m^3	5.4
Slow decomposing fraction particulate organic nitrogen	PON3	gN/m^3	0.1
Fast decomposing fraction particulate organic phosphorus	POP1	gP/m^3	0.06
Medium decomposing fraction particulate organic phosphorus	POP2	gP/m^3	0.11
Slow decomposing fraction particulate organic phosphorus	POP3	gP/m^3	0.01
Bluegreen energy type	BLUEGRE_E	gC/m^3	0.03
Bluegreen nitrogen type	BLUEGRE_N	gC/m^3	0.09
Bluegreen phosphorus type	BLUEGRE_P	gC/m^3	0.006
Marine dinoflag energy type	DINOFLAG_E	gC/m^3	0.03
Marine dinoflag nitrogen type	DINOFLAG_N	gC/m^3	0.09
Marine dinoflag phosphorus type	DINOFLAG_P	gC/m^3	0.006
Marine diatoms energy type	MDIATOMS_E	gC/m^3	0.03
Marine diatoms nitrogen type	MDIATOMS_E	gC/m^3	0.09
Marine diatoms phosphorus type	MDIATOMS_E	gC/m^3	0.006

Process parameters most relevant to sediment solids sedimentation and resuspension are summarized in Table 13. The sedimentation velocities of settling

matters ranged from 0.2 to 1 m/d, and the algae sedimentation velocities were the default values.

Table 13. Summary of process parameter values for Delft3D-WAQ used for suspended sediment calibration/validation test

Parameters	Input Name	Unit	Value
Zeroth-order resuspension flux	ZResDM	gDM/m^2/d	5
First-order resuspension velocity	VResDM	1/d	20
Zeroth-order burial flux for S1	ZBurDMS1	gDM/m^2/d	0
Zeroth-order burial flux for S2	ZBurDMS2	gDM/m^2/d	0
First-order burial rate for S1	VBurDMS1	1/d	0.05
First-order burial rate for S2	VBurDMS1	1/d	0.05
Zeroth-order digging flux to S1	ZDigS1DM	gDM/m^2/d	1
Zeroth-order digging flux to S2	ZDigS1DM	gDM/m^2/d	10
Critical shear stress for S1 resuspension	TaucRS1DM	N/m^2	0.0625
Critical shear stress for S2 resuspension	TaucRS2DM	N/m^2	0.0625
Zeroth-order sedimentation flux for IM1	ZSedIM1	g/m2/d	0
Zeroth-order sedimentation flux for IM1	ZSedIM2	g/m2/d	0
Algal (Blue Green) sedimentation velocity	Blue Green (E/N/P)	m/d	0
Algal (Marine diatoms) sedimentation velocity	Marine Diatoms (E/N/P)	m/d	0.5/1/1
Algal (Marine dinoflag) sedimentation velocity	Marine Dinoflag (E/N/P)	m/d	0.5/1/1
Sedimentation velocity VIVP	VSedVIVP	m/d	0.2
Sedimentation velocity APATP	VSedAPATP	m/d	0.2
Sedimentation velocity Opal	VSedOpal	m/d	0.5
Sedimentation velocity FeCO3	VSedFeCO3	m/d	0.2

Sedimentation velocity particulate amorphous oxidizing iron	VSedFe3pa	m/d	0.2
Sedimentation velocity particulate crystalline oxidizing iron	VSedFe3pc	m/d	0.2
Sedimentation velocity Iron(II) sulphide	VSedFeS	m/d	0.2
Sedimentation velocity pyrite	VSedFeS2	m/d	0.2
Sedimentation velocity IM1	V0SedIM1	m/d	0.5
Sedimentation velocity IM2	V0SedIM2	m/d	0.5
Sedimentation velocity POC1	V0SedPOC1	m/d	0.5
Coefficient in flocculation	n POC1	-	0
Salinity enhanced settling factor	EnhSedPOC1	-	3
Sedimentation velocity POC2	V0SedPOC2	m/d	0.5
Coefficient in flocculation	nPOC2	-	0
Salinity enhanced settling factor	EnhSedPOC2	-	3
Sedimentation velocity POC3	V0SedPOC1	m/d	0.5
Coefficient in flocculation	nPOC3	-	0
Salinity enhanced settling factor	EnhSedPOC3	-	3
Bottom roughness/friction	Rough	m	0.0175
Mannings coefficient	Manncoef	m	0.01

Calibration test (8/15/2005 00:00 to 9/1/2005 00:00)

The simulation results of the sediment concentration in the water column showed strong correlation with the bottom shear stress. In Figure 31 a), the horizontal gray dash line indicated the critical shear stress of 0.0625 N/m^2 used in Chung's study,

and during the calibration period the shear stress remained below 0.025 N/ m^2, and only increased above 0.03 N/ m^2 on 8/31/2005.

The comparison between the measured turbidity data and the simulated sediment concentrations (shown in green) is shown in Figure 31 (b). The constraint conditions used in the resuspension formulation in Delf3D-WAQ suggest that when the shear stress doesn't exceed the critical shear stress, the shear stress limitation function become zero (Eq.3.3.31). As the results, the simulated sediment concentrations remained low below 10 mg/L during low bottom shear stress period, but peaked on 8/31/2005 at the level of approximately 37 mg/L, which agreed with the measured value reasonably well at increased bottom shear stress event.

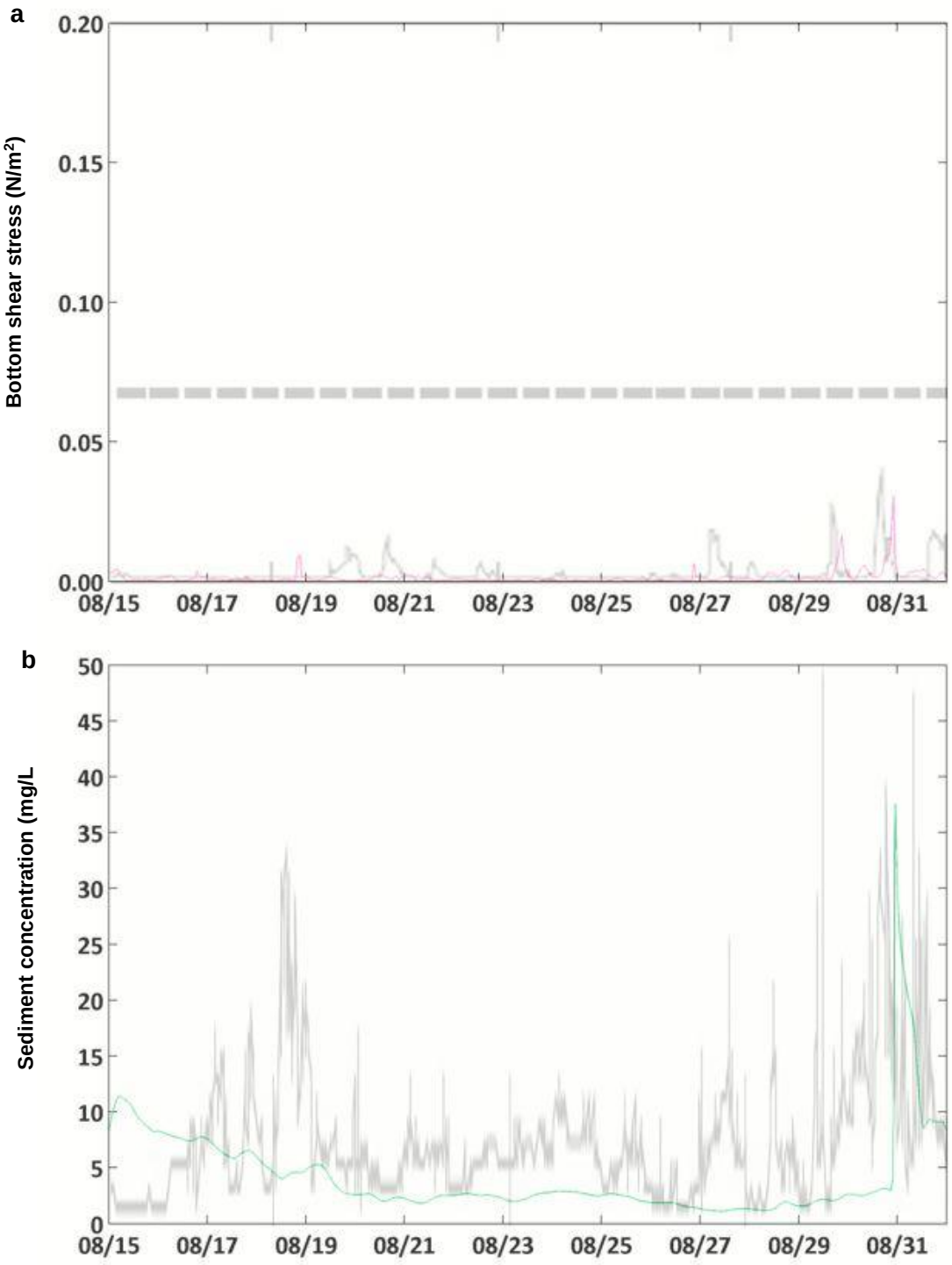

Figure 31. Comparison of bottom shear stress (a) and suspended solid concentrations (b) from calibration period, August 9 2005 to September 1 2005 at 0.5 m off the bottom in depth of 6 m. The measured data was shown in black line, the simulated bottom shear stress was shown in pink line and the simulated sediment concentration was shown green line.

Validation test (8/15/2005 00:00 to 9/1/2005 00:00)

The validation period is from 9/1/2005 00:00:00 to 9/17/2005 00:00:00, the initial condition on 9/1/2005 was derived from the last timestep of the calibration period. Figure 32a indicated that the simulated bottom shear stress matched with the measured shear stress caused by waves pretty well. The bottom shear stress increased significantly and reached 0.17 N/m^2 on 9/9/2005 at 18:00 and remained in the average level of critical shear stress during the storm period.

The data showed that the bottom shear stress from 9/1/2005 to 9/9/2005 was mostly below 0.01 N/m^2, as the results, the sediment solid concentration remained low at 5 mg/L before the storm occurred. During the storm occurred on 9/9/2005, the model resolved significant increase of the simulated sediment solid concentrations from 5 to 45 mg/L that agreed well with the measured data (Fig. 32b).

Overall, the calibration/validation test suggested that the model was able to generate suspended sediment concentration in the water depth of about 5.5 m (0.5 m off from the bottom near south eastern shore) at a reasonable range as compared to the measured data. In addition, the bottom shear stress simulation results corresponded with the observed shear stress data very well, therefore, the timing of sediment resuspension in the water column was considered well matched.

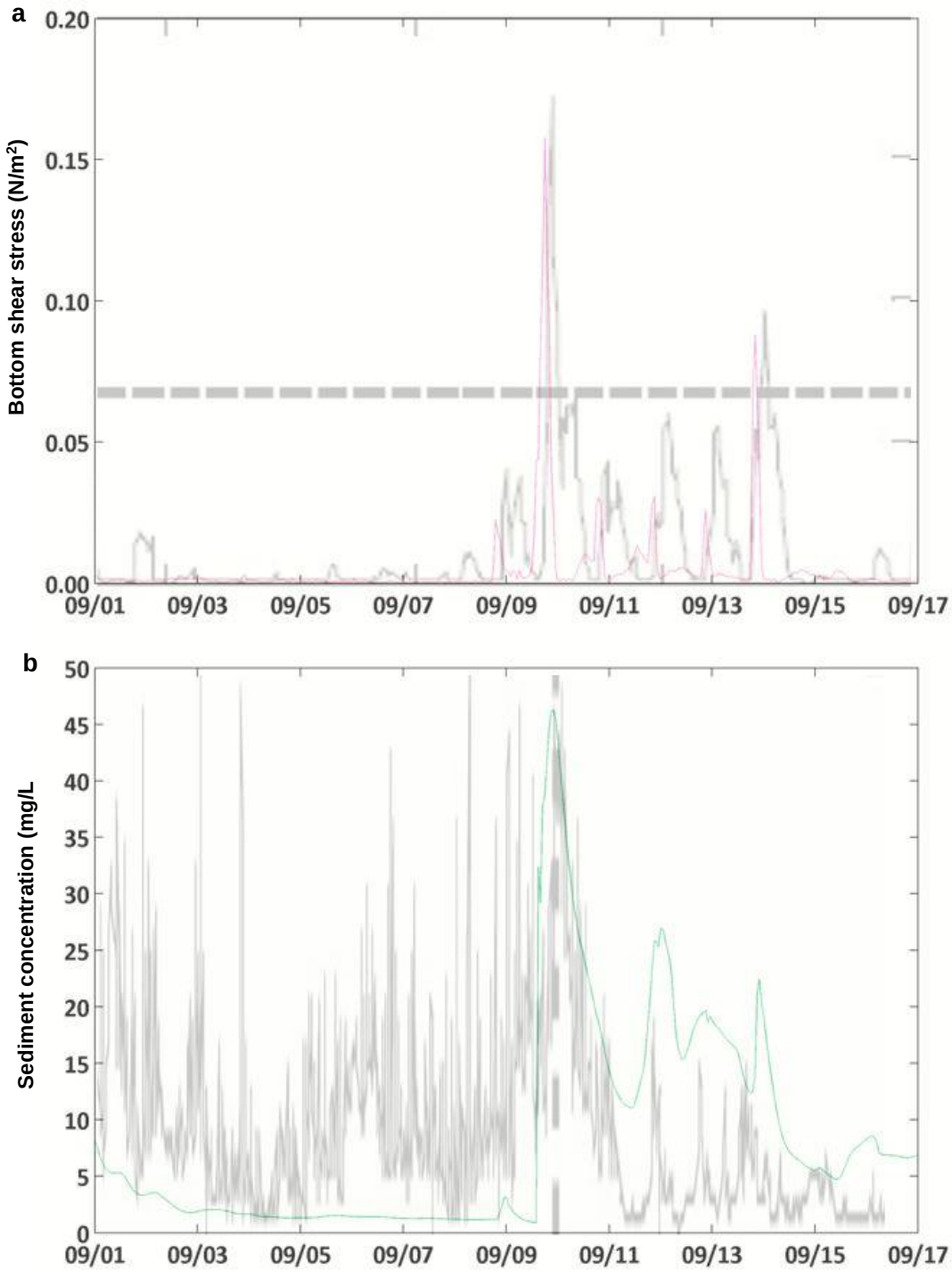

Figure 32. Comparison of bottom shear stress (a) and suspended solid concentrations (b) from validation period, September 1 2005 to September 17 2005 at 0.5 m off the bottom in depth of 6 m. The measured data was shown in black line, the simulated bottom shear stress was shown in pink line and the simulated sediment concentration was shown in green line.

Water quality variable validation (9/1/2005 00:00 to 8/8/2007 00:00)

The water quality parameters selected for validation test are Dissolved oxygen (DO), unionized ammonia (NH_3), orthophosphate (PO_4), and chlorophyll *a* (Chl *a*). In the WAQ module, the period to generate initial conditions is from 8/8/2005 to 8/15/2005, followed by calibration period from 8/15/2005 to 9/1/2005, and the nearly two years of validation period from 9/1/2005 to 8/8/2007. The observed water quality parameters at the Sea and influent rivers were obtained from the quarterly sampling campaign conducted by Bureau of Reclamation in collaboration with California Department of Water Resources and Salton Sea Authority since 1999. The validated model output for DO are compared with the measured values in Figure 33.

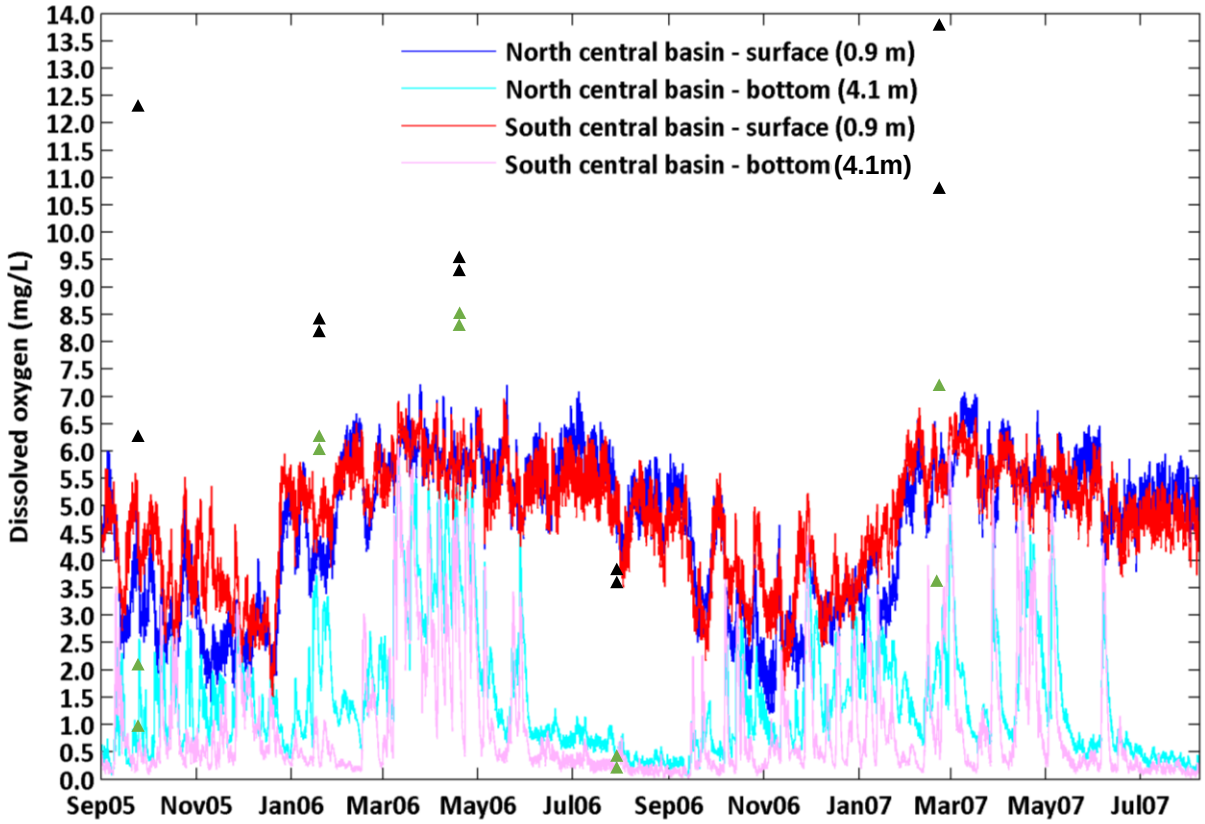

Figure 33. Comparison between measured DO (triangles) and simulated DO (lines) in north central/south central basins of the Salton Sea. The black triangles denote measured data at 0.95 m from the surface, and green triangles denote that from 4.1 m above the bottom.

Vertical aggregation in the WAQ module played a significant role in determining the values of the water quality parameters. The vertical grid is 16 layers in the FLOW module where a more detailed vertical schematization is required to resolve stratification and was aggregated into 6 layers in the WAQ module. In this work σ-grid (constant number of layers, with varying layer thickness) was used for 3D computation. As the results, the layer thickness of the aggregated layers from top to bottom are 6.8%, 6.8%, 10.05%, 18%, 27%, 30.9%, which is equivalent to dynamic segment depths of 0.95 m, 0.95 m, 1.47m, 2.52m, 3.78 m, 4.1 m, respectively in roughly central north and south basin regions.

Figure 33 showed that DO concentration in 0.95 m below the surface were underestimated in general except in the month of July. It is due to the fact that WAQ module could not compute DO concentration in segment smaller than 0.95 m within the surface layer. Therefore, higher reaeration rate and gross primary algal production rate that occurred at the surface were not account for in the WAQ module. On the other hand, the DO concentration in the bottom layer matched with the measured values fairly well, with small level of under estimation during spring season.

The validated model output for NH_3 were compared with the measured values in Figure 34. At the pH value set constant at 8.2, the results showed that among the two basins, simulated results from the central south basin showed better agreement with the measured values. The reason could be due to the fact that the discharge rates from Alamo and New River in the south end are 10 times larger than Whitewater River in the north end. Therefore, simulated results in both basins were both more aligned with the measured data in the south basin.

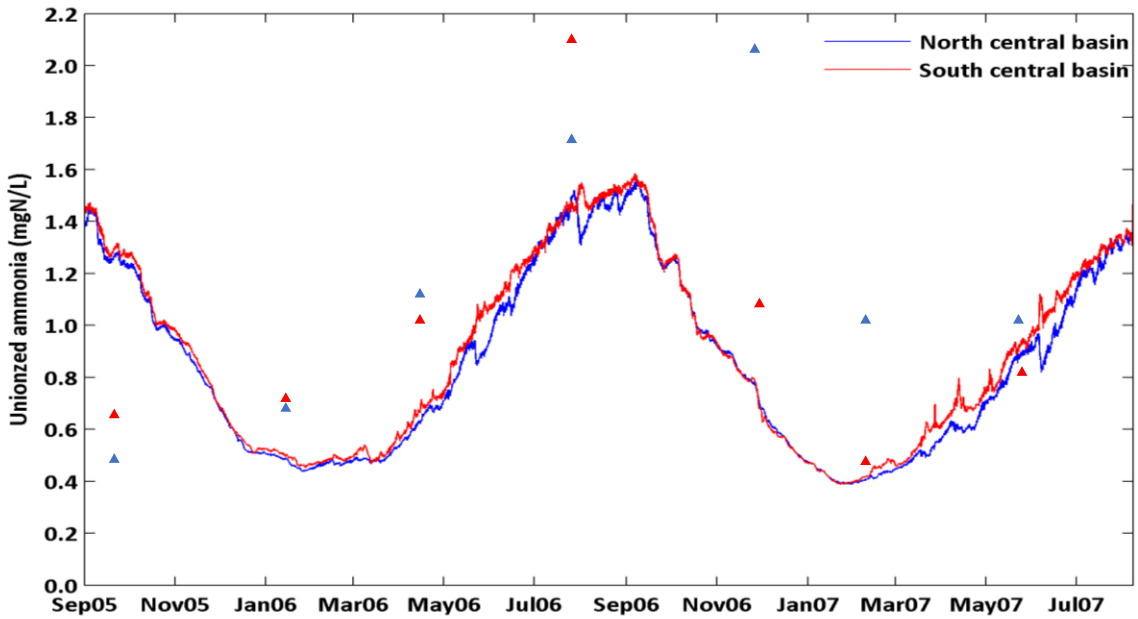

Figure 34. Comparison between measured unionized ammonia (triangles) and simulated depth averaged unionized ammonia (lines) in north central/south central basins of the Salton Sea. The blue triangles denote measured depth averaged values in north central basin, and red triangles denote that in south central basin. EPA method 350.1was used for ammonia analysis and has a precision of 0.058 as standard deviation in this range of concentrations.

Note that the nutrient concentrations (ammonium, nitrate and orthophosphate) in the river inflows were set at constant values based on the two years average of the quarterly data from September 2005 to May 2007, therefore introducing some errors in nutrient simulations. Nonetheless, the WAQ module was able to resolve the seasonal fluctuations of unionized ammonia reasonably well. Unionized ammonia concentrations were within 24% difference in the south-central basin, and within 66 % difference in the north central basin compared to the observed values.

The validated model output for orthophosphate were compared with the measured values in Figure 35. The simulated results showed an over prediction before winter 2007 and under prediction in February 2007. The measured values showed that

PO_4 concentrations were low in July 2006, and high in February 2007, which is considered associated with high algal productivity in the summer and low in the winter.

The WAQ module computes dissolved orthophosphate based on the mass balance below:

$$\frac{\Delta PO_4}{\Delta t} = loads + transport \pm sorption + mineralization \pm percipitation + primary\ production + autolysis + atmospheric\ deposition \pm sediment\ exchange\ flux.$$

Among which the process of phosphorus adsorption onto suspended sediments, and precipitation/dissolution of vivianite and apatite minerals are subjected to huge uncertainty due to lacking information on iron containing fraction of the sediments and iron (II) concentrations in the Sea. Another uncertainty lied within the autolysis process where fractions of nutrients are released into the water column when primary producer die. The parameters involved in this process were set in default as there were no information on autolysis fraction in each primary producer.

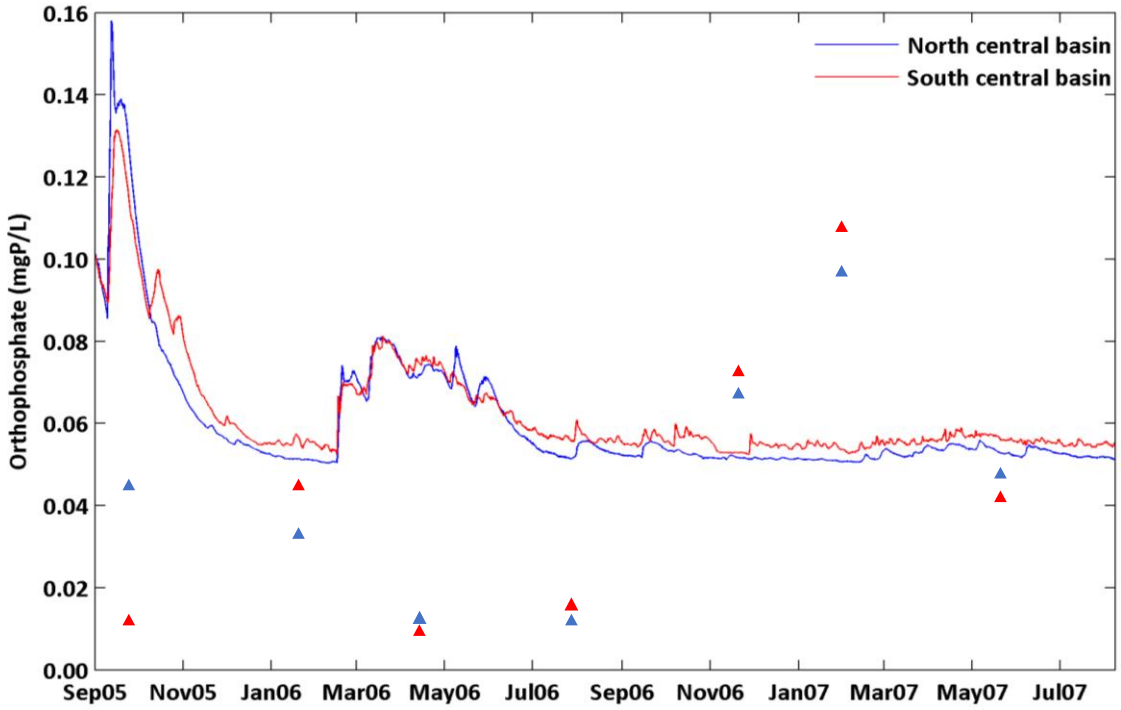

Figure 35. Comparison between measured orthophosphate (triangle) and simulated depth averaged orthophosphate (lines) in north central/south central basins of the Salton Sea. The blue triangles denote measured depth averaged values in north central basin, and red triangles denote that in south central basin. EPA method 365.1was used for orthophosphate analysis and has a precision of 0.0165 as standard deviation in this range of concentrations.

The two peaks of PO_4 concentrations in September 2005 and March 2006 were resulted from sediment resuspension induced orthophosphate desorption in the water column. The two events were the direct results of the two storm events occurred during that time. Note that the WAQ module assumes that phosphate desorption fluxes and mineralization fluxes from the sediment layers are instantaneous input to the entire water column, which could lead to peaks of high orthophosphate concentrations in the water column as shown in Figure 35. Overall, the simulated results showed that the resuspension flux of adsorbed phosphate from the sediments is the main driving flux to determine the orthophosphate concentrations in the water column.

The simulated results for chlorophyll *a* are compared with the measured values in Figure 36. The comparison showed that the simulated chlorophyll *a* followed the measured trends rather well, with the exception of under estimation in mid-February 2007. The patterns of chlorophyll *a* demonstrated seasonal trend that differentiate high algal productivity during the spring and summer seasons, and low during the winter months.

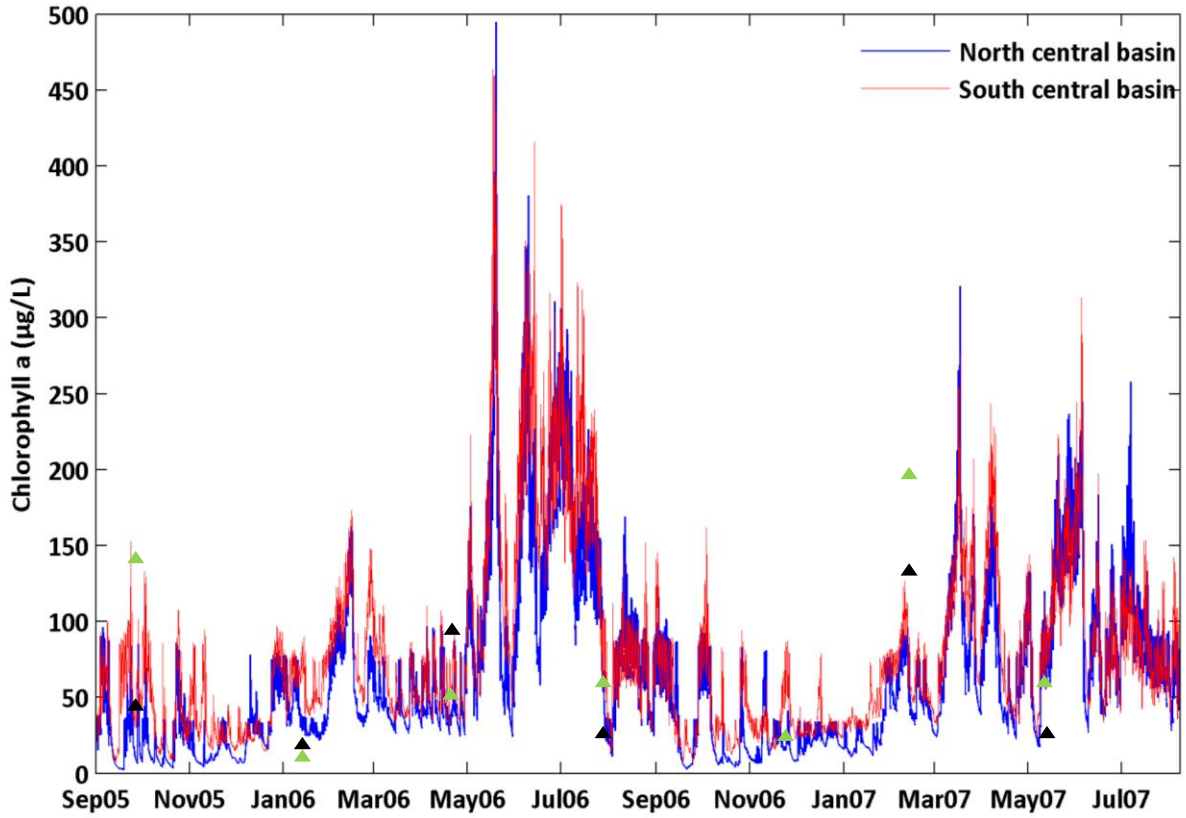

Figure 36. Comparison between measured chlorophyll a (triangle) and simulated depth averaged chlorophyll a (lines) in north central/south central basins of the Salton Sea. The green triangles denote measured depth averaged values in north central basin, and black triangles denote that in south central basin.

Chapter 4 Water Quality Mitigation Strategies

Previous studies have repeatedly confirmed that sediment resuspension played a significant role in influencing the water quality of the Salton Sea, and the resuspension events are heavily driven by winds. Therefore, in this chapter wind-induced sediment resuspension events and the consequent water quality dynamics in the water column are being evaluated in the presence of emerged islands in the south basin of the Salon Sea. In this scenario the emerged islands serve as the wind fetch obstruction devices on the surface water.

The other critical water quality issue of the Salton Sea is the rising salinity, which was exacerbated by the execution of the Quantification Settlement Agreement that led to 38.4 % of agricultural runoff diverted away from the Sea to metropolitan areas since 2018. In the other mitigation scenario, sweater import/export implementation was simulated to assess the impacts on salinity and consequential water quality dynamics in the Salton Sea. Lastly, the combination of seawater canals and treated tributary inflows is simulated as the most robust mitigation strategy. The nutrients (ammonium-N, nitrate/nitrite-N, and orthophosphate) in the treated tributary river water were reduced by 90% before entering the Sea.

The effects of reduced wind fetch on thermal stratification and horizontal velocity during the storm period in September, 2005 are presented in section 4.1 and section 4.2. The seawater canals locations and discharge rates are discussed in section 4.3, and the two years of long-term effects on critical water quality variables are presented in section 4.4. The timeframe of simulations for the status quo condition and the three mitigation scenarios are from 8/8/2005 to 8/8/2007. Within the time frame, the

calibration period in the FLOW module is from 8/8/2005 to 9/1/2005, and the validation period is from 9/1/2005 to 8/8/2007. In the WAQ module, the period to generate initial conditions is from 8/8/2005 to 8/15/2005, followed by calibration period from 8/15/2005 to 9/1/2005, and the nearly two years of validation period from 9/1/2005 to 8/8/2007.

4.1 Status quo

The status quo condition of the Salton Sea is shown in Figure 37. The letters N and S denote the center of north basin and the center of south basin, respectively.

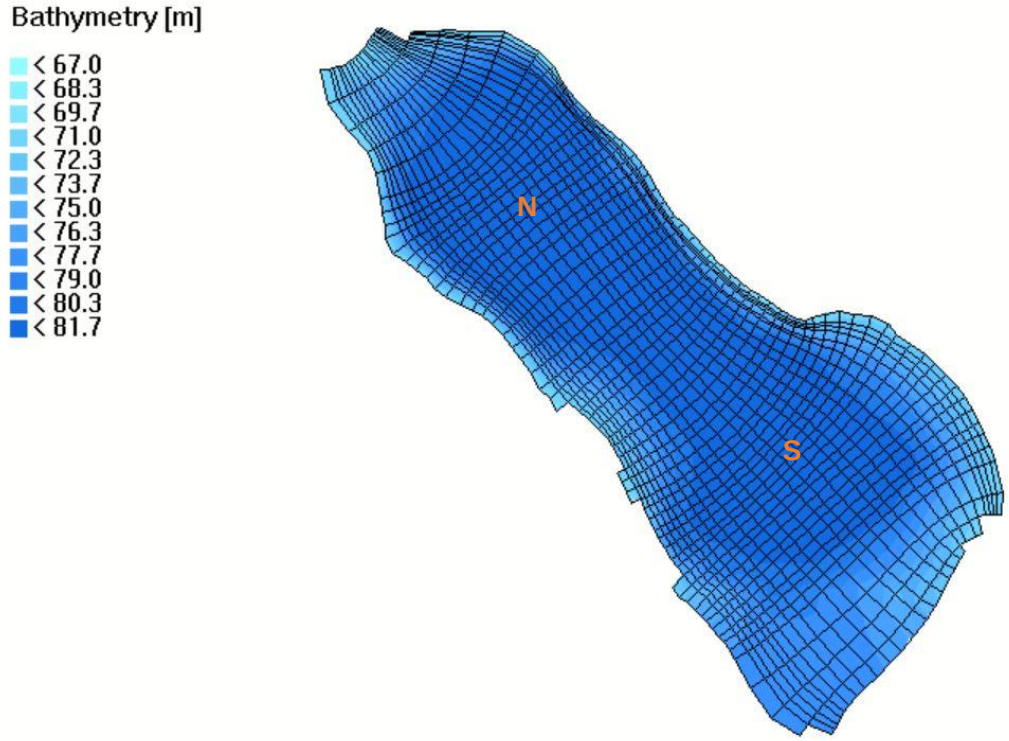

Figure 37. Salton Sea surface in the status quo condition (vertical datum NAVD88)

Water temperatures

North basin stratification

In the center of the north basin where the deepest water depth reaches to 83 m below sea level, the simulation results showed a distinct thermal stratification before the

storm occurred in the evening of 9/9/2005, ranging from 29 to 34 ^{o}C. The temperature range of 29 to 30 ^{o}C and 33 to 34 ^{o}C dominated the bottom and surface three to four meters in depth. Diurnal temperature fluctuations in the surface layer were resolved by the model, representing by the intermittent one degree, sometimes up to two degrees increase in the surface layer. During the storm period from 9/9/2005 to 9/15/2005, it is shown that the water temperature became homogeneous throughout the water column, averaging the surface and bottom temperature and keeping the water temperature at the range of 30 to 32 ^{o} C. Later on, the water column remained homogenous in temperature as it entered fall season (Fig. 38a).

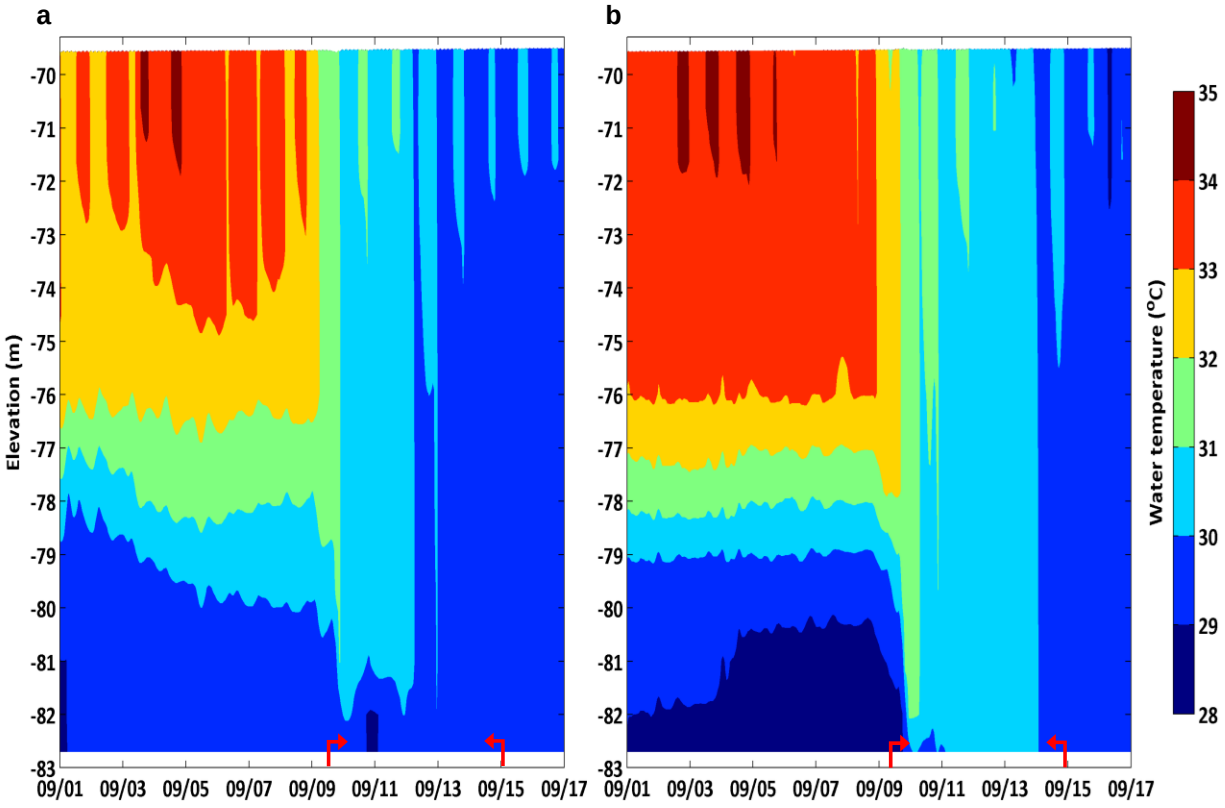

Figure 38. Thermal stratification in (a) central north and (b) central south basin form 9/1/2005 to 9/17/2005. The storm period is denoted by the red bracket.

South basin stratification

During the same period of time the thermal stratification in the center of the south basin showed a larger temperature stratification from 28 to 35 ^{o}C from the bottom to the water surface before the storm events. However, compared to that of the north basin, almost the entire six meters down from the surface were uniformly in the range of 33 to 34 ^{o}C, with occasional increase to 35 ^{o}C. A less structured thermocline was shown in the central south basin where most of the water column was 33 to 34 ^{o}C, followed by a rather sharp transitional layers from -77 m to -79.5 m in depth where the temperature dropped three degrees to reach the range of 28 to 30 ^{o}C from three meters above the bottom. During the storm period, a homogeneous temperature range of 30 to 31^{o}C also occurred dominantly in the south-central basin, followed by a homogeneous temperature range of 29 to 30 ^{o}C in the fall season.

The results were consistent with the findings presented by Rueda et al. (2009), in which a more prominent thermal stratification was shown in the north basin, and a less structured thermal stratification was in the south basin.

Horizontal velocity

Timeseries (9/1/2005 00:00:00 to 9/17/2005 00:00:00) of horizontal velocity magnitudes in the north basin center and the south basin center are shown in Figure 39. The simulation showed that during the storm event that peaked on 9/9/2005 18:00, the horizontal velocity magnitude increased from about 0.03 m/s to 0.3 m/s in both central basins in two meters above the bottom. However, during the storm period, the simulation showed slightly higher velocity (less than 0.03 m/s higher) in the northern

basin. This phenomenon could be due to the fact that the deepest depth of the north basin was about one meter deeper than that of the deepest depth of the south basin, and the south basin is generally shallower.

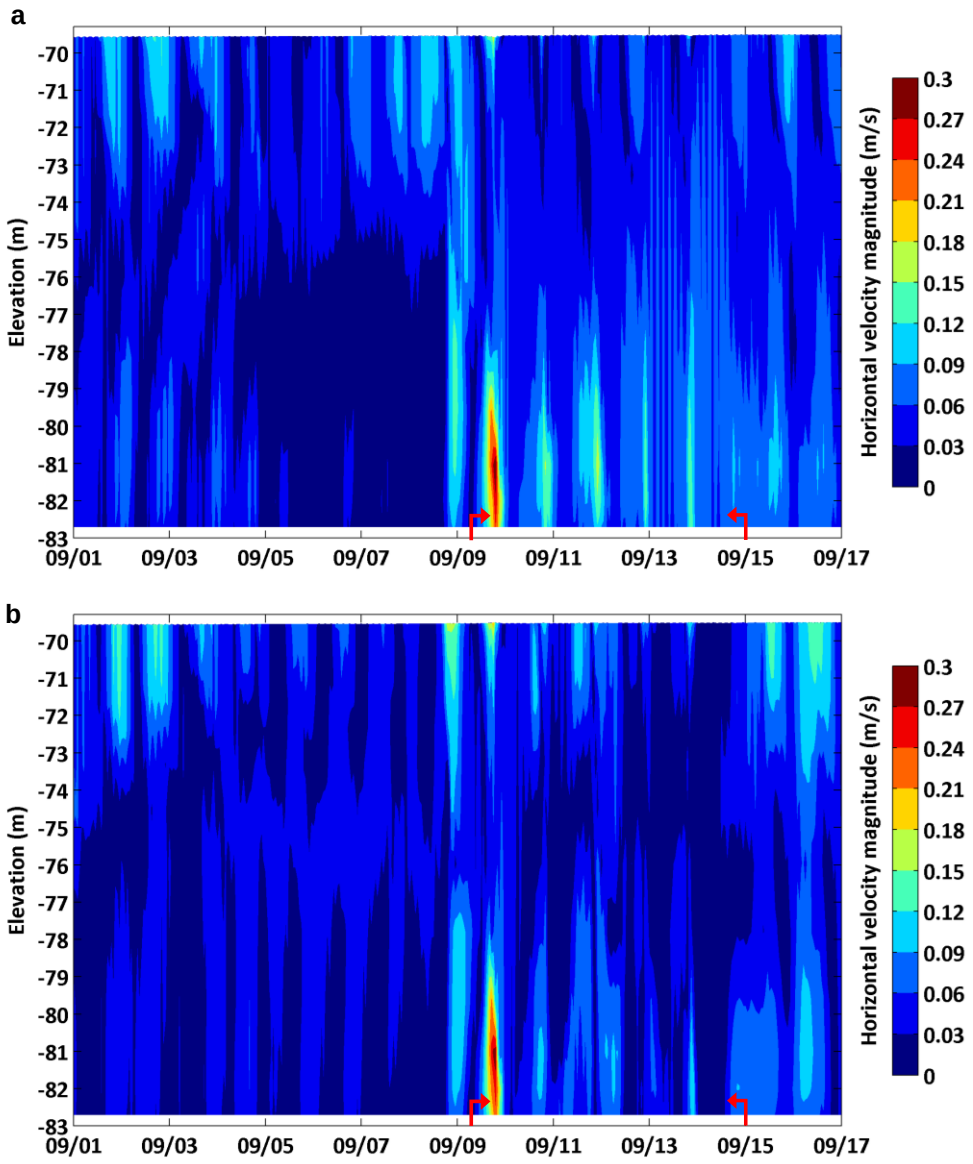

Figure 39. Horizontal velocity magnitudes in depth contour in central north (a) and central south basin (b) from 9/1/2005 to 9/17/2005. The storm period is denoted by the red bracket.

4.2 Emerged islands as wind obstruction devise scenarios

The proposed emerged islands design is based on the fact that the wind speed and direction from 8/1/2005 to 9/27/2005 measured at the southeastern meteorological site CIMIS #128 (Fig. 21) showed that predominant wind direction was from northwest, southeast, and southwest directions, among which wind blowing from 240^{o} to 270^{o} was especially stronger

than the rest of the direction. As the results, the islands serve to obstruct wind fetch and to interfere the flow from the two main tributary rivers from the south end. The emerged islands (shown as blue polygons in Figure 40) were consisted of five rigid sheets extended from the bottom to above the surface of the Sea with surface areas ranging from 2 to 2.5 mi^2.

Figure 40. Emerged islands in the Salton Sea.

Water temperatures

The thermal stratification simulation results in the presence of emerged island suggested that having installed islands in the south basin would not affect thermal stratification structure in the north basin much compared that in the status quo condition (Fig.41a). The thermal stratification in the central north basin during the same timeframe was almost identical to that in the status quo. Similarly, central south basin also showed consistent thermal stratification with the status quo where a deeper layer of temperature range (33 to 34 ^{o}C, with occasional 35 ^{o}C) was extended from the surface to six meters below the surface, followed by a steep temperature drop from 33 to 30 ^{o}C from -76 to -79 m msl.

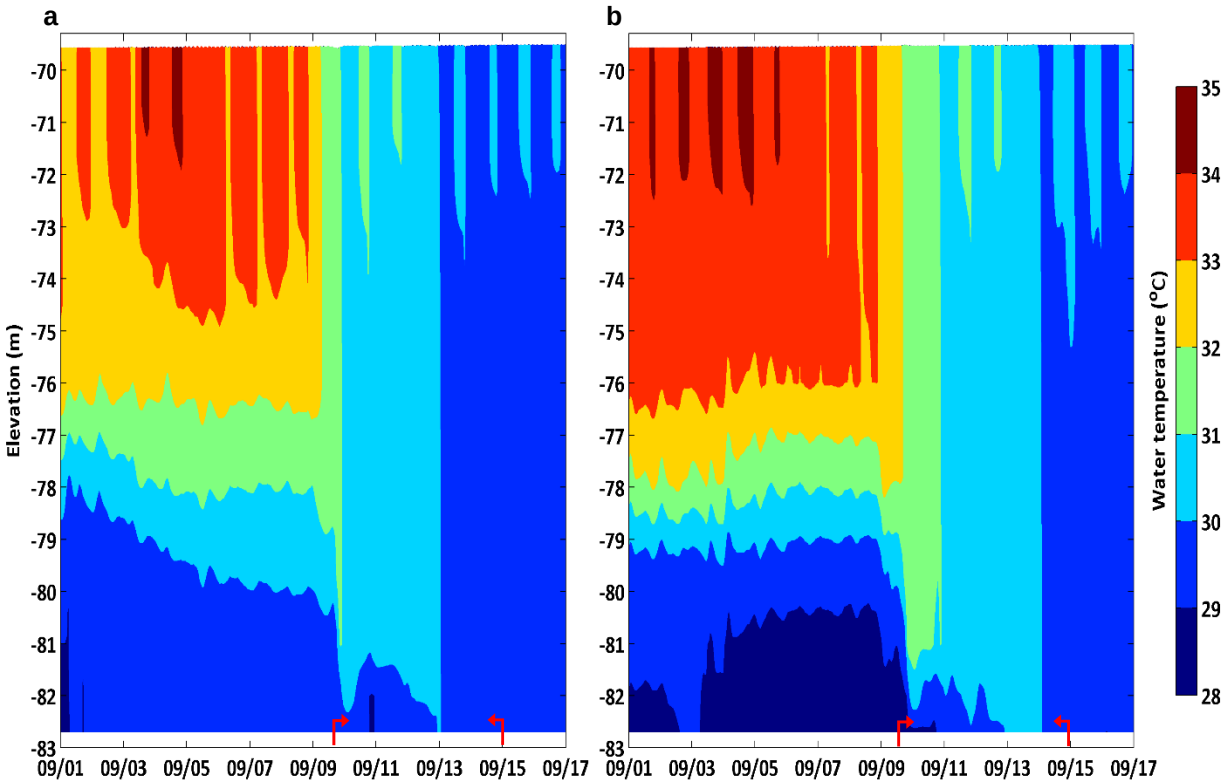

Figure 41. Thermal stratification in central north (a) and south basin (b) from 9/1/2005 to 9/17/2005 in the presence of emerged islands. The storm period is denoted by the red bracket.

The change occurred in central south basin during the storm period where it appeared that the water column was not completely homogenous in temperature; the water column had a smaller thermal stratification, ranging from 29 to 32 ^{o}C, the low temperature only occurred from 1.5 meters above the bottom. This phenomenon suggested that emerged island prevented the water column to be completely mixed in the central south basin (Fig. 41b).

Horizontal velocity

Comparing to the horizontal velocity magnitudes in the status quo, the simulation results in the presence of emerged island showed that central north basin also experienced same degree of higher horizontal velocity during the storm period in 5 meters above the bottom; the velocity increased up to 0.27 m/s during the storm peak, and to 0.15 m/s in average during the storm (Fig. 42a).

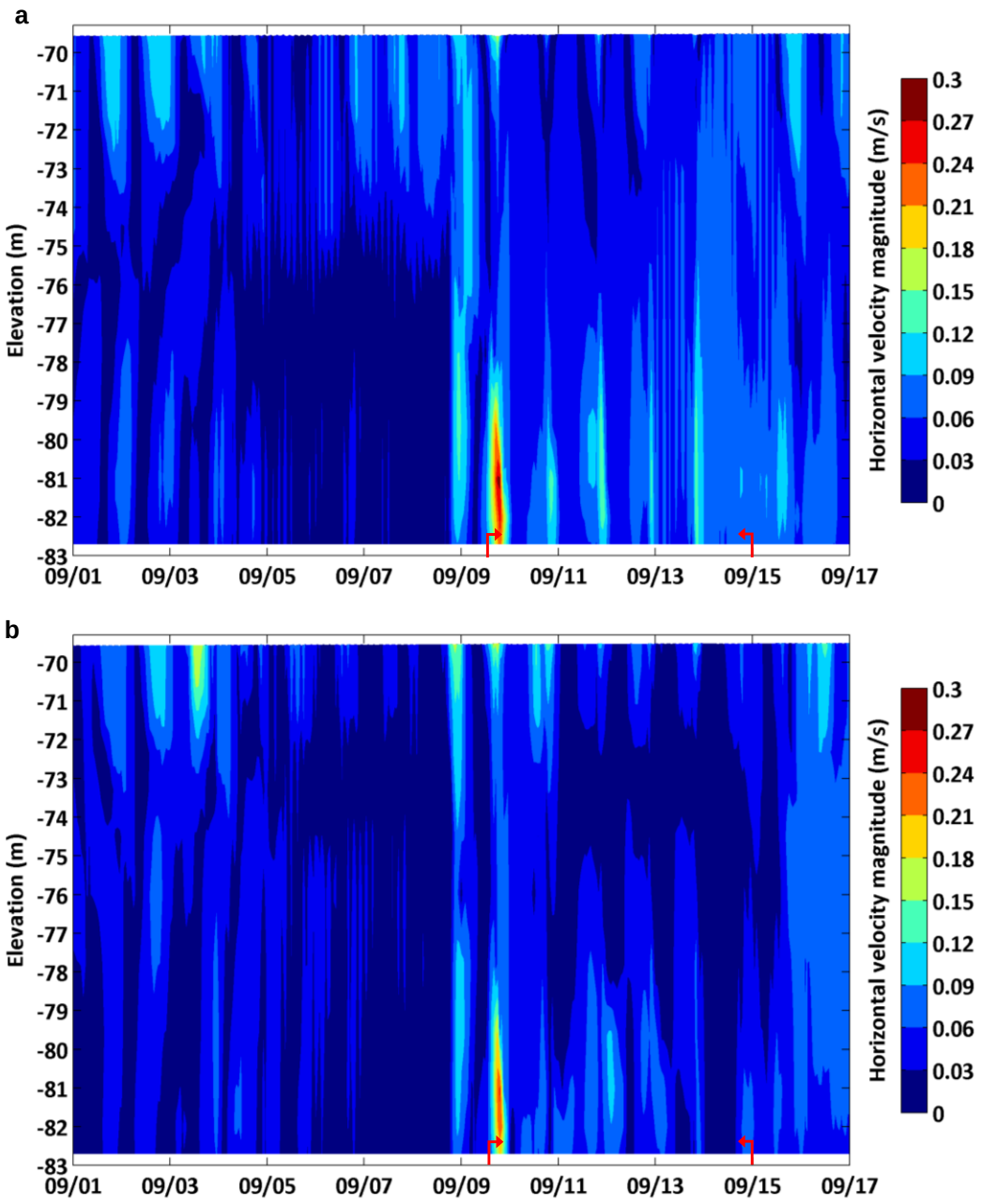

Figure 42. Horizontal velocity magnitude in depth contour in central north basin (a) and south basin (b) from 9/1/2005 to 9/17/2005 in the presence emerged islands. The storm period is denoted by the red bracket.

On the contrary, during the storm period the horizontal velocity magnitude in the central south basin decreased to range of 0.21 to 0.24 m/s, which is up to 0.06 m/s

decreased compared to that in the status quo. The results showed that reduced wind fetch also reduced horizontal velocity toward the bottom of the central south basin.

4.3 Seawater import/export scenarios

The seawater import and export canals locations are indicated as diagonal polygons in the south and north shorelines, respectively in Figure 43.

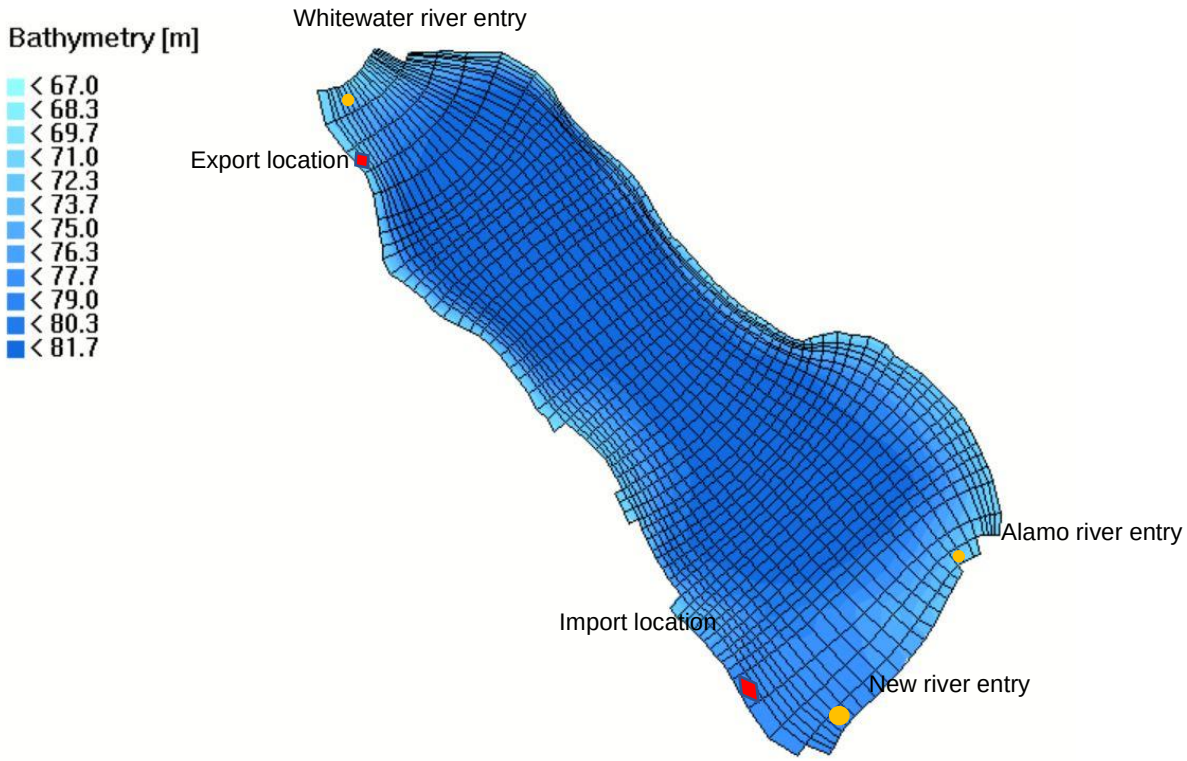

Figure 43.Discharge locations of the Salton Sea. Diagonal denotes seawater import/export entry and exit points, and circle refer to the locations of the tributary river entry points.

A first order integration of a continuous stirred-tank reactor model was utilized to estimate the seawater inflow/outflow rates. The mass balance to estimate out-going salinity is calculated as follows:

$$V\frac{dC}{dt} = Q_{in} \cdot C_{in} - Q_{out} \cdot C_{out}$$

where V denotes the volume (m^3) of the Sea using an average depth of 9 m, and C_{in} , C_{out} represent salinity concentration in the unit of g/m^3, t is timestep in section, and Q_{in} , Q_{out} denote the canals flow rates (m^3/s) at inflow and out flow, respectively.

The components of inflow/outflow flow rates and concentrations are described as follows:

$$Q_{in} = Q_{in,sea} + Q_{in,new\ river} + Q_{in,alamo\ river}$$

$$Q_{out} = Q_{out,sea} + Q_{out,\ evaporation}$$

$$C_{in} = C_{in,sea} + C_{in,new\ river} + C_{in,alamo\ river} + C_{in,whitewater\ river}$$

Average values for the tributary river flow rates, and evaporation rate were used to estimate the out-going salinity concentration. The tabulated values are summarized in Table 14.

Table 14. Parameters for salinity mass balance

$V\ (m^3)$	8.24E+09
$Q_{in,sea}\ (\frac{m^3}{s})$	225
$Q_{in,new\ river}\ (\frac{m^3}{s})$	24.34
$Q_{in,alamo\ river}\ (\frac{m^3}{s})$	16
$Q_{out,sea}\ (\frac{m^3}{s})$	215.5
$C_{in,sea}\ (\frac{g}{m^3})$	36000
$C_{in,new\ river}\ (\frac{g}{m^3})$	2500
$C_{in,alamo\ river}\ (\frac{g}{m^3})$	2500

Based on the estimation, the salinity would gradually decrease from 46 ppt in 2005 and be stabilized at around 38 ppt in 2.47 years.

4.4 Water quality variables comparisons

In this section the long-term effects on Salton Sea's water quality in the status quo condition, in the presence of emerged island, having seawater imported/exported into/out of the Sea, and combining seawater canals implementation with treated tributary rivers scenarios are compared. The results shown are during the validation period from 9/1/2005 to 8/8/2007, and the water quality variables being examined are dissolved oxygen (DO), orthophosphate (PO_4), unionized ammonia (NH_3), chlorophyll a (*Chl a*), and salinity.

Dissolved oxygen

Mean dissolved oxygen concentrations in the 0.95 meter below the surface and 4.1 meters above the bottom of the Sea in four scenarios during the summer season (4/1/2007 – 6/30/2007) are shown in Figure 44.The simulation showed that in the status quo condition, the mean DO concentration was approximately at 5 mg/L (90% of saturation) in the first meter below the surface (Fig. 44 a-1), and dropped below 2 mg/L from the bottom to roughly four meters above the bottom (Fig. 44 a-2).

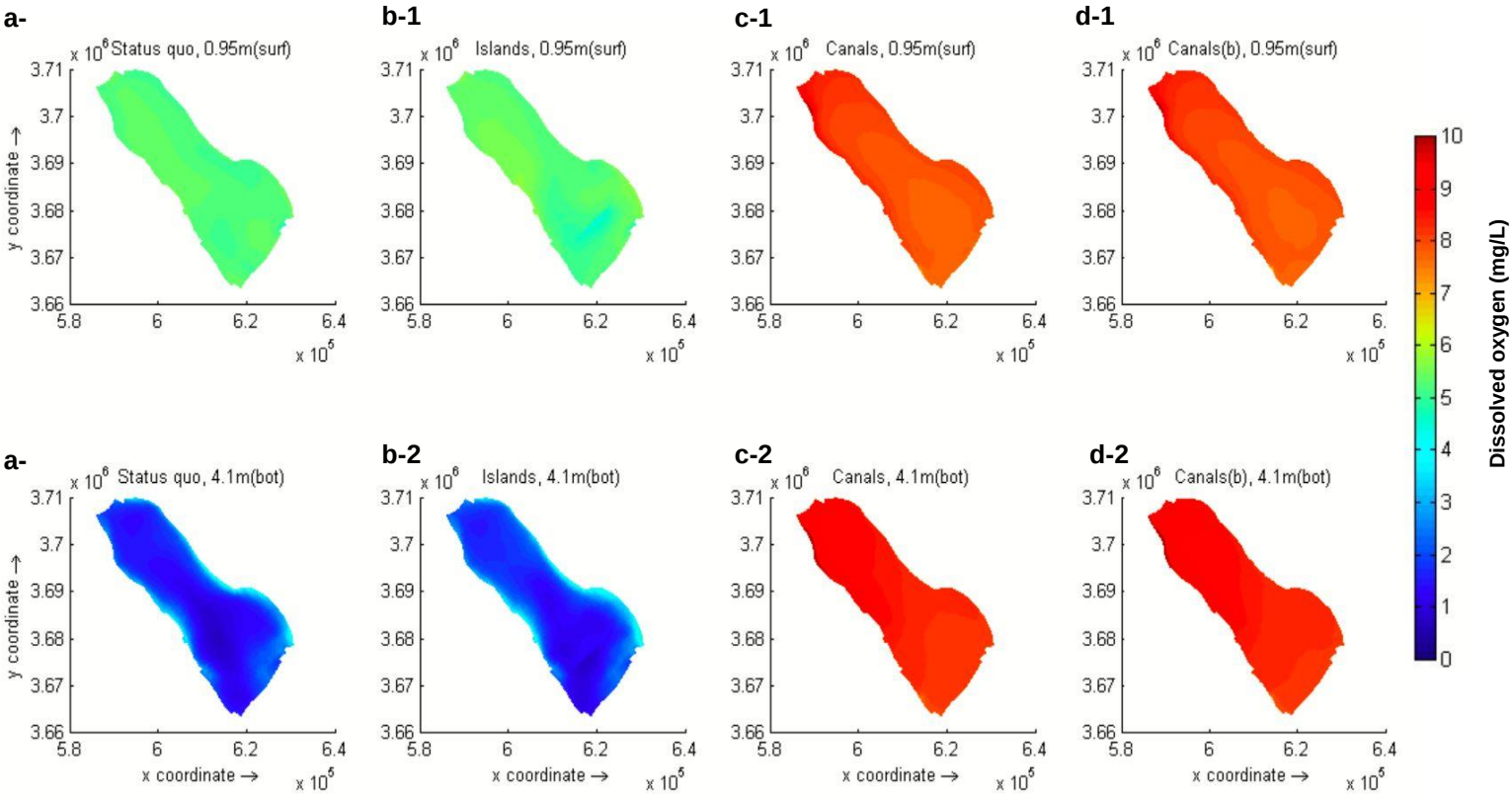

Figure 44. Mean dissolved oxygen concentration in the status quo condition and under the three mitigation scenarios in summer season from 4/1/2007 to 6/30/2007. 1 m(surf) and 4.1 m(bot) denote 1 meter below the surface, and 4.1 meter above the bottom, respectively. Canals(b) represents the scenarios of canals with treated tributary rivers.

In the presence of emerged islands, the DO concentration in surface 0.95 meter showed similar results to the status quo, but about 0.5 mg/L higher in the bottom layer (Fig.44 b-1, b-2). The phenomenon is due to less biological oxygen demand substances being suspended by wind-induced currents, therefore less oxygen consumption in the water column.

The seawater import/export scenario brought in seawater that contained high DO saturated water (8mg/L) at the rate of 225 m^3/s in the south basin from layer 5 (among the total of 6 layers), and exported lake water that contained average DO concentration in the north basin at 215.5 m^3/s from layer 5 (Fig.44 c-1, c-2). As the results, the DO

concentration in the surface layer increased to the range of 8 to 9 mg/L, and in the bottom four meters, the DO concentrations increased to approximately 8 to 10 mg/L on average during spring 2007. The reason why the DO level in bottom layer showed approximately 1 mg/L higher concentration than the surface layer is due to the general underestimation of surface layer discussed in previous section. Lastly, having treated tributary inflows in addition to canals implementation showed rather similar results to the only canals scenarios (Fig.44 d-1, d-2).

Orthophosphate

The results of depth averaged PO_4 concentration in the north and south-central basins are shown in Figure 45. In the status quo condition orthophosphate concentrations peaked to the range of 0.08 to 0.16 mg/L in response to the two storms (>12 m/s) occurred in the Salton Sea, and maintained at approximately 0.058 mg/L in both north and south-central basins during normal days.

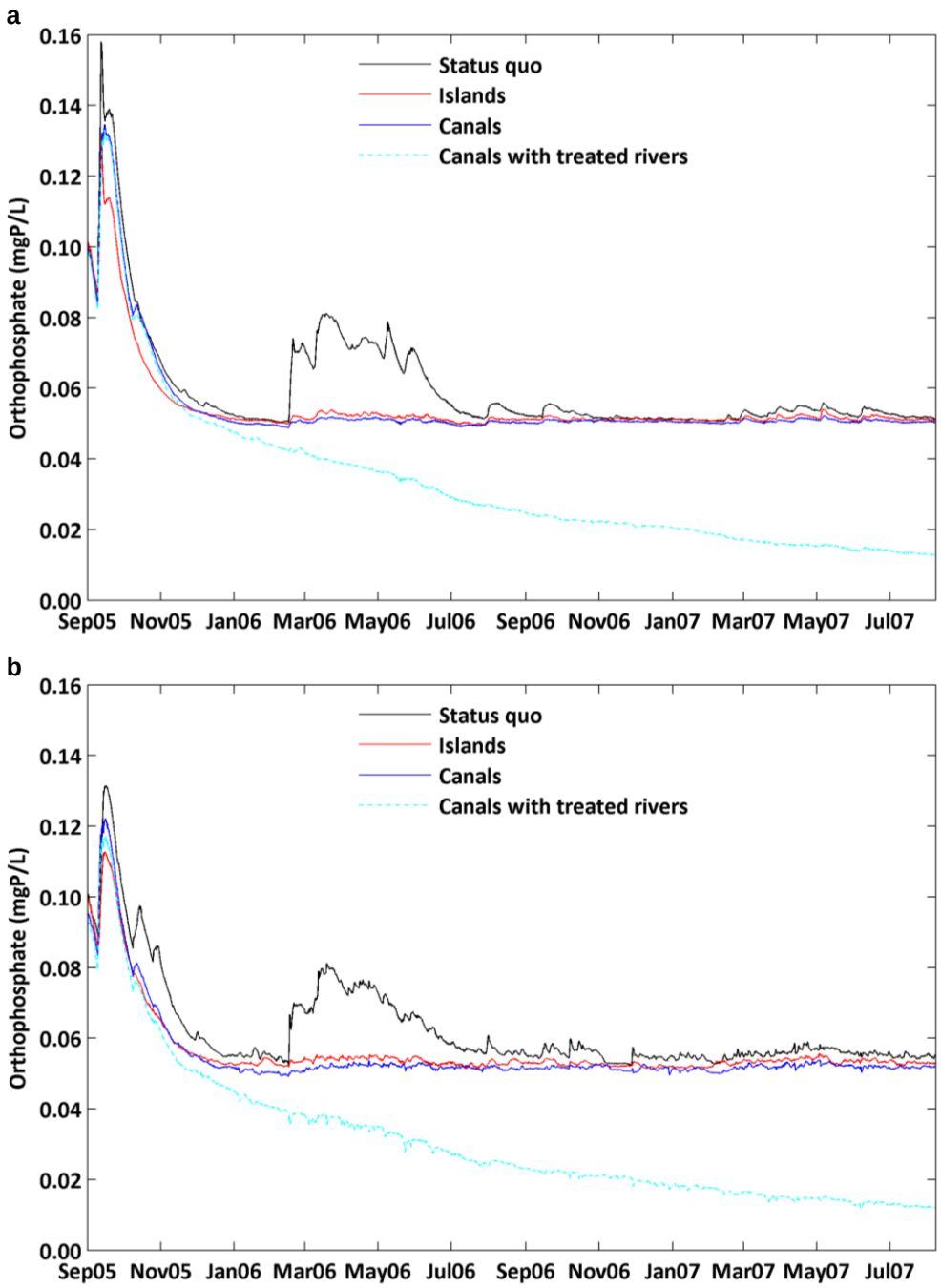

Figure 45. Mean orthophosphate concentration in the status quo condition and under the mitigation scenarios from 9/1/2005 to 8/8/2007 in a) north central basin and b) south central basin in the Salton Sea.

Orthophosphate adsorbs onto the adsorbing components of suspended sediments including iron(III)oxyhydroxides, aluminum hydroxide, silicates, manganese

oxides and organic matter. The mechanism of PO_4 reduction in the scenario of emerged islands is mainly associated with sediment activities. The wind-induced sediment resuspension activities were reduced because of reduced bottom shear stress, as the results, less resuspension occurred to release orthophosphate into the water column. The presence of islands reduced PO_4 by 18 % in the first peak, and by 31 % in the second compared to the status quo.

The seawater import/export scenario brought in seawater that was set to have no PO_4 along with sediments from the south basin at 225 m^3/s, and exported lake water that contained average PO_4 and sediment concentrations in the north basin at 215.5 m^3/s. The simulated results showed that depth averaged PO_4 concentration in the north central basin decreased by approximately 14% in the first peak during the first storm, and by 36% during the second storm compared to the status quo. In the south-central basin, the peak was decreased by 8.3% during the first storm, by 36% during the second. After a year of simulation, the decrease percentage remained at approximately 5% in the north central basin and 8% in the south-central basin and from August 2006 until the end of simulation.

In the scenario where nutrients in the tributary rivers were reduced by 90% in addition to seawater canals implementation, the results showed drastic decline of PO_4 concentrations starting from March 2006, leading to PO_4 concentrations as low as 0.01 mg/L by August 7, 2007 in the Salton Sea.

Unionized ammonia

Unionized ammonia is toxic to aquatic lives and is mostly contributed by the tributary river inflows that contain municipal waste, agricultural and manure application runoff. The unionized ammonia is the product of the dissociation of the ammonium (NH_4^+) ion, which is subjected to aerobic nitrification to produce nitrate (NO_3). As the results, the concentration of unionized ammonia changed as the oxygen level changed. During the summer season, dissolved oxygen tends to decrease due to high water temperature and algal production, causing less nitrification and favoring ammonium ion dissociation, therefore higher unionized ammonia being produced in the water column. The phenomenon is resolved by the WAQ module, unionized ammonia concentrations had seasonal fluctuation patterns in the status quo and three other mitigation strategies as shown in Figure 46.

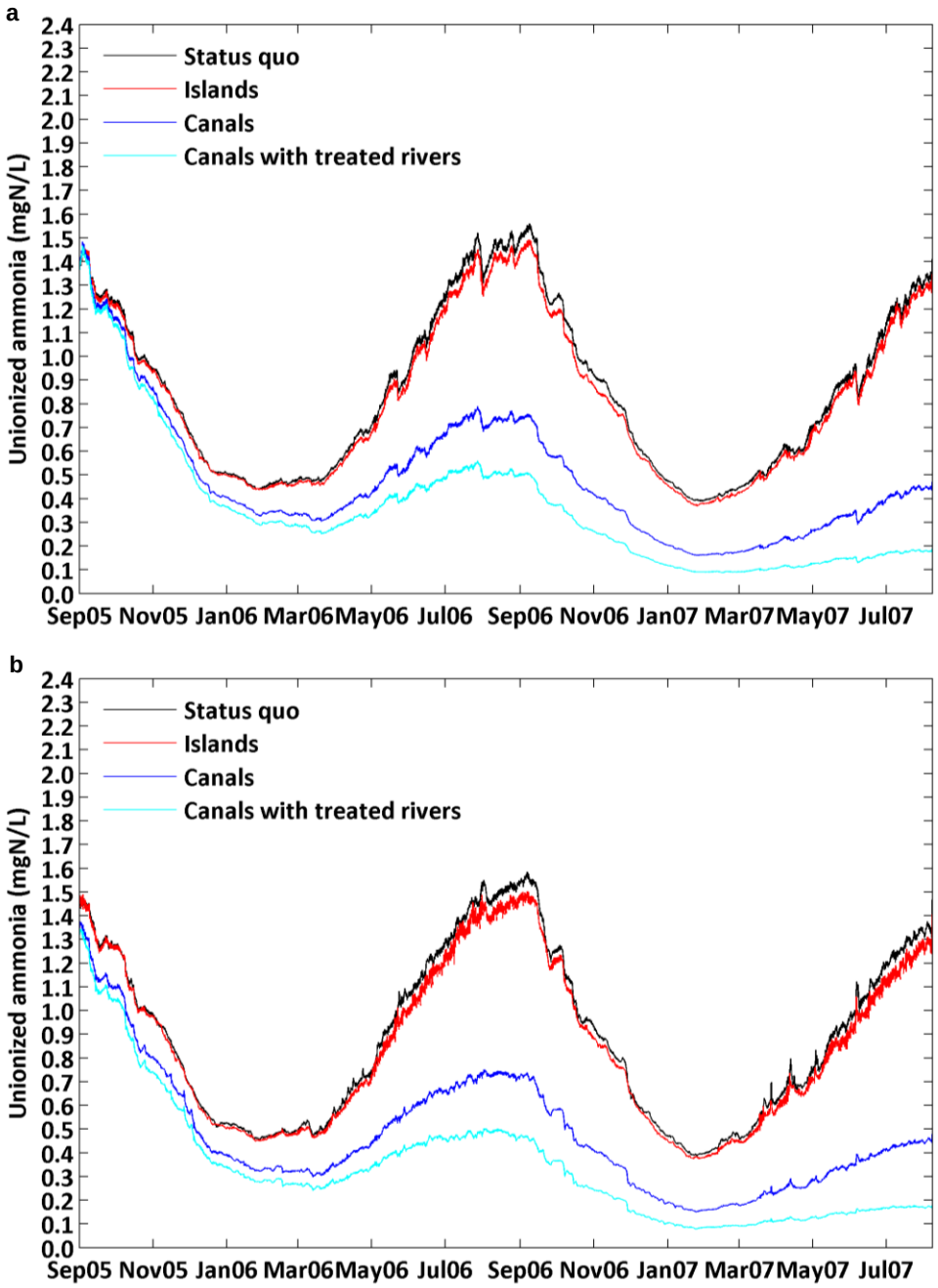

Figure 46. Mean unionized ammonia concentration in the status quo condition and under the mitigation scenarios from 9/1/2005 to 8/8/2007 in a) north central basin and b) south central basin in the Salton Sea.

The emerged islands situated in the south basin served to restrict currents that were loaded with high ammonium concentrations from the rivers entering in the south basin, preventing concentrated ammonium to further transported into the whole sea

before being taken up by phytoplankton, or undergone nitrification. The effects of unionized ammonia declined was most prominent during summer season (from June to early September), in which NH_3 decreased up to approximately 6.3% in the presence of emerged islands.

The imported seawater was set to contained zero ammonium concentration, leading to a tremendous decrease of unionized ammonia concentration in the Sea as average level of ammonium were being exported out of the Sea. During the peak of summer 2006, NH_3 decreased by approximately 49.3% in the presence of seawater canals, and by 68.3% in the scenario where tributary rivers were treated in addition to seawater import/export implementation.

In the most robust scenario, the simulation showed that the decrease of NH_3 became even larger from June 2007. Nonetheless, for two years of simulation, it is shown that the Salton Sea's unionized ammonia level was still above the critical level of 0.05 mg/L in all scenarios.

Chlorophyll *a*

The chlorophyll *a* concentration in spring season is highest throughout the year, therefore the maximum values in spring season (4/1/2007 – 6/30/2007) were chosen to represent algal productivity in all four scenarios (Figure 47). In spring 2007, the chlorophyll *a* concentration in the status quo reached to the range of 400-450 µg/L near central basin, and the concentration in the south basin was up to 1.25 times higher than that in the north basin (Fig.47a). In the presence of islands, it is shown that high algal productivity was localized in the south basin at a lower range of 350- 400 µg/L (Fig. 47b). The results were expected since main nutrients sources were from New and

Alamo River from the south end, and that the presence of islands interfered nutrients transportation toward north basin, therefore lowering algal production in general.

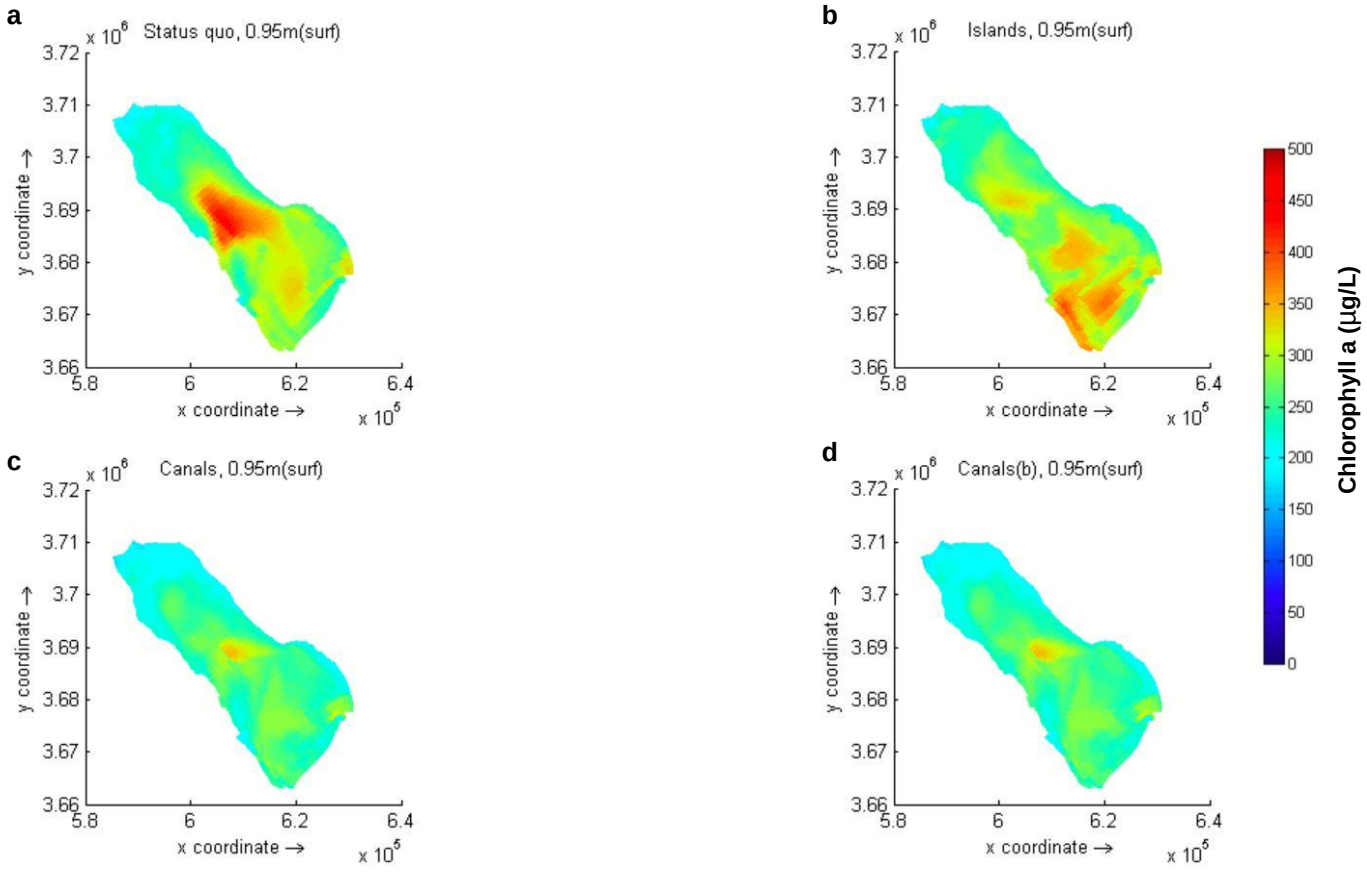

Figure 47. Maximum chlorophyll *a* concentration in a) the status quo condition, and in mitigation scenarios including b) islands, c) seawater canals, and d) treated tributary inflows with canals from 4/1/2007 to 6/30/2007.

At the end of the two-year simulation the level of ammonium in the canals scenario was one half of that in the status quo, and the level of nitrate in the canals scenario was about 36% of that in the status quo (data not shown). As the results, the maximum chlorophyll *a* concentration during Spring in 2007 in the canal scenarios were lower at the range of 200-300 µg/L with only central basin had higher Chl *a* concentration up to approximately 350 ug/L (Fig.47c).

In the scenario where inflows nutrient concentrations were reduced by 90%, the ammonium, nitrate and orthophosphate concentrations were 16%, 4.5% and 17% of that in the status quo, respectively by August 2007. Nonetheless, the simulation results showed that maximum Chl *a* concentration in Spring 2007 were identical to that in the canals implementation without tributary treatment scenario. The reason is due to the growth constraints within the BLOOM module is set to maximize the total net growth; if the actual biomass is lower than the threshold biomass concentration of an algal species at the beginning of a timestep, threshold (minimum) level would be used. By reducing the timestep from 6 hours to 1 hour in BLOOM, the algal biomasses between the two canals scenarios were started to diverge in June 2007; the chlorophyll *a* concentrations decreased by 9% in the canal scenario with treated inflows (data not shown) in summer 2007.

Total bottom shear stress

The comparison of total bottom shear stress in the status quo condition and in the presence of emerged islands in the south basin is shown in Figure 48. The figures present the maximum values throughout the Sea in September 2005 during which the first storm occurred. Even though the emerged islands were consisted of five separate rigid sheets extended from the bottom to above the surface of the Sea with surface areas ranging from 2 to 2.5 mi^2, the simulation showed that the general region covered by the emerged islands had low bottom shear stress at the range of 0.02 to 0.04 N/m^2 (Figure 48b). The effects of reduced wind fetch were also shown near the eastern shorelines.

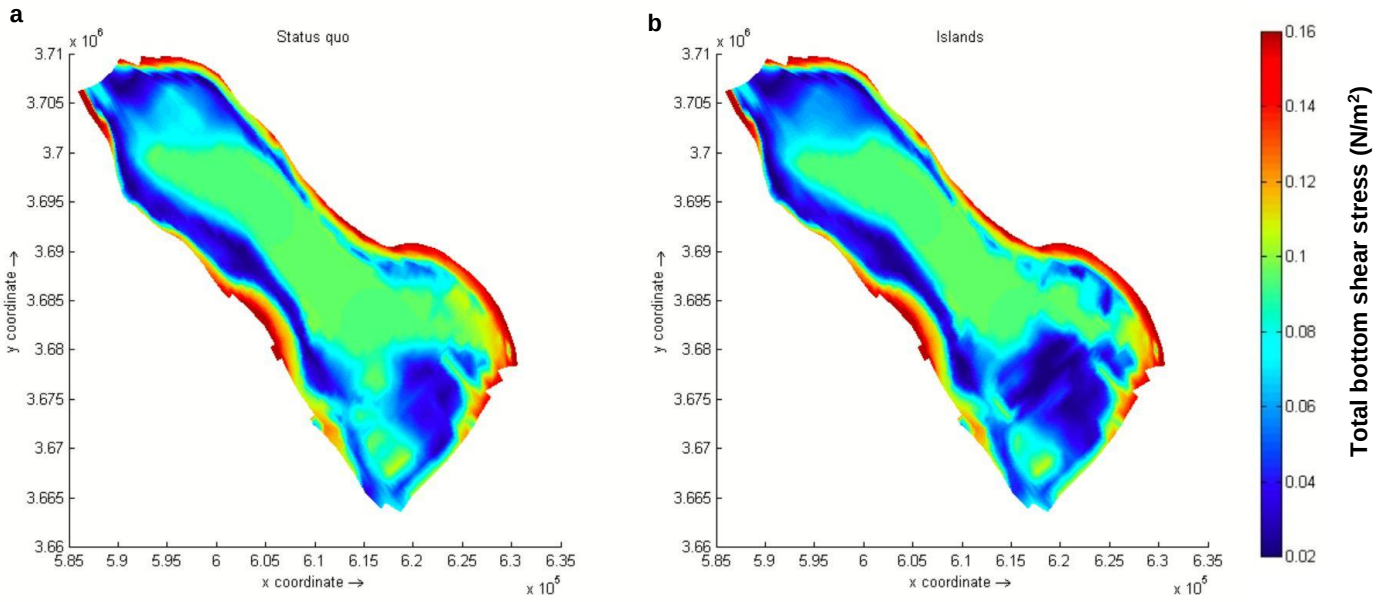

Figure 48. Maximum total bottom shear stress in a) the status quo condition, and b) in the presence of islands from 9/1/2005 to 9/30/2005.

The critical bottom shear stress is 0.0625 N/m^2 estimated using the representative sediment size of 25 µm in the Salton Sea (Chung et al. 2008). Below this critical threshold the constraint conditions used in the resuspension formulation in Delf3D-WAQ would carry out the shear stress limitation function as zero, resulting no resuspension activity (Equ.3.3.31). The results confirmed the orthophosphate concentrations decline in the presence of islands, and indicated that area covered by the islands are shielded from bottom shear stress exceeding above the critical level, which in the long term could enhance burial effects that lead to orthophosphate decrease in the water column.

Salinity

The salinity in the status quo and in the two mitigation strategies are compared in Figure 49. Distinct discrepancy in salinities in the two-year simulations between the seawater import/export scenario and without introducing external less saline water were resolved well by the FLOW module. The starting salinity on September 1, 2005 was 46 ppt, and was steadily decreased to the range of 38 to 39 ppt by August 8, 2007. The results were fairly consistent with the mass balance estimation, which indicated that salinity would start to stabilize at 38 ppt in 2.47 years.

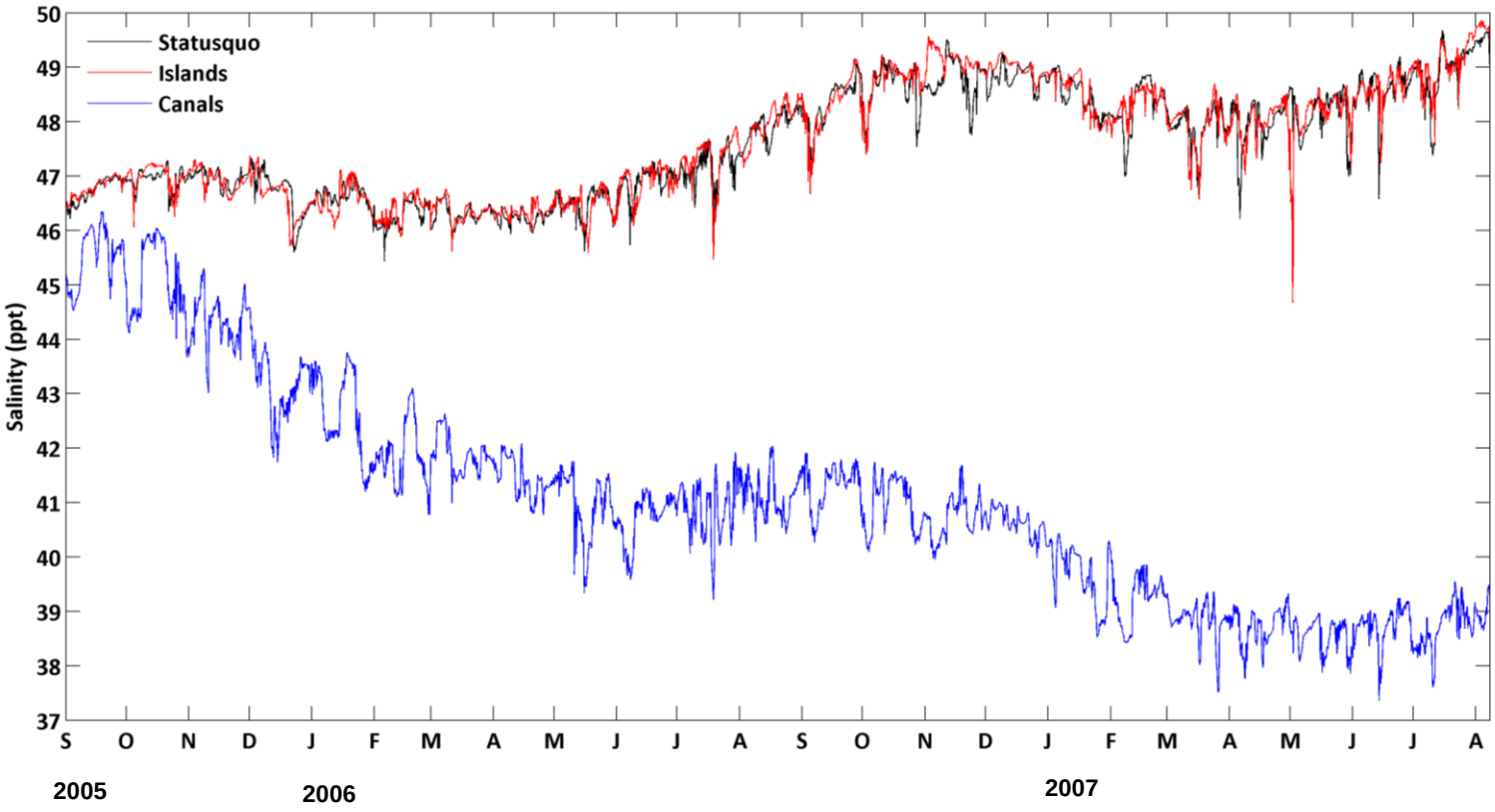

Figure 49. Salinity progression in the status quo and in the mitigation scenarios from 9/1/2005 to 8/8/2007.

The fluctuation appeared in the salinity progression was corresponded to water level fluctuation, which was directly associated with seasonal variation of tributary river flow rates. Figure 49 also showed that salinity would not be affected by the presence of islands in the southern basin.

Chapter 5. Conclusions and Future directions

5.1 Summary and conclusion

In this study three Delf3D modules -Delft3D FLOW, Delft3D WAVE and Delft3D WAQ- within the Delft3D modeling suite were utilized to investigate the water quality dynamics of the Salton Sea in the status quo and mitigation scenarios. Datasets from two different field measurement campaigns conducted by previous studies were used for calibration and validation in each individual module.

The FLOW module was calibrated against the simulation results conducted by UC Davis modeling team based on the data measured during 10/9/1997 to 10/24/1997. The FLOW module was calibrated using the spatially interpolated wind fields defined by five CIMIS stations around the periphery of the Salton Sea, and was able to resolve horizontal velocity that agreed well with the simulation outcome by the other numerical model. The parameters including horizontal eddy viscosity, vertical eddy viscosity, and manning's n as roughness coefficients were determined based on this calibration task.

The WAVE module was calibrated and validated based on the dataset collected by Chung from 8/8/2005 to 9/17/2005. The measured data included currents and waves, water temperature, turbidity. The field measurements in 2005 in the Salton Sea were the latest complete dataset that allowed simultaneous hydrodynamics and water quality variables calibration/validation tasks. As the results, the simulation conditions in this work were based on and extended from the same time period as in Chung's work.

Using the wind field created by the meteorological data obtained solely from the station (CIMIS #128) located near the southeastern shore of the Sea, the wave and

currents results simulated by the WAVE module were in good agreement with the measured data. The wave heights, current velocity and bottom shear stress were all in rather good fit to the observed values.

Deriving the hydrodynamic information from the FLOW and WAVE modules the WAQ module was able to generate suspended sediment concentration at a reasonable range as compared to the measured data. Later on, the WAQ module was calibrated and validated against the dataset collected quarterly by the Bureau of Reclamation for the water quality variables of interest, including dissolved oxygen, orthophosphate, unionized ammonia, and chlorophyll *a*.

Simulation output for the DO concentration during validation period showed that DO concentration throughout the water column were in the reasonable range as the measured data. Due to vertical grid limitation, the DO concentrations were simulated in 0.95 m below the surface, leading to general underestimation on the surface level except in the month of July. Nonetheless, the DO concentration in the bottom layer matched with the measured values fairly well.

Seasonal fluctuations of unionized ammonia were resolved well and within reasonable range by The WAQ module, and simulated results from the central south basin showed better agreement with the measured values than the central north basin.

The processes (sorption, precipitation, autolysis, and mineralization) for orthophosphate computation involved various uncertainties and assumptions that resulted in over estimation for PO_4 in general. Nonetheless, the simulated results showed that the sediment resuspension flux was corresponded to wind velocity

magnitudes and is the main factor that determines the orthophosphate concentrations in the water column. This phenomenon was consistent with the findings of previous studies. Lastly, the simulation of agal productivity resolved seasonal trend for chlorophyll *a* concentration that followed the measured trends rather well, with the exception of under estimation in mid-February, 2007.

The presence of emerged islands has two purposes, 1) to interfere inflows that contained high nutrient concentrations and suspended sediments from transporting norward to the entire Sea, and 2) to reduce wind fetch, thereby reducing the bottom shear stress that affect wind-induced sediment resuspension activities. The effects on DO and NH_3 were considered modest as the results showed less than 40% increase of DO due to less biological oxygen demand substances being suspended by wind-induced currents. Naturally, little DO improvements led to approximately 6.3 % decreased NH_3 during the summer season.

On the other hand, the presence of islands reduced PO_4 by 18 % during the first storm, and by 31 % in the second compared to the status quo. Orthophosphate concentrations remained about 5% lower (<0.06 mg/L) than that in the status quo condition from September 2006 til August 2007. Furthermore, simulation showed that high algal productivity was localized in the south basin where chlorophyll *a* concentrations were at a lower range of 350- 400 µg/L compared to 400-500 µg/L in the status quo from 4/1/2007 to 6/30/2007.

Having imported aerated, nutrients-free seawater at 225 m^3/s from southwestern shore, and exporting lake water at 215.5 m^3/s in the northwestern shore, the DO concentration decreased less than 50% throughout the water column from 7/1/2006 to

9/30/2006. The PO_4 concentrations in the north basin experienced larger decline than in the south basin (14% and 8.3%, respectively) during the first storm in September 2005). As time progressed the decline percentage were roughly consistent throughout the Sea, remaining at approximately 5 to 8 % decrease of PO_4 compared to the status quo.

To the contrary of the modest decline of PO_4 in the Sea, unionized ammonia NH_3 decreased by approximately 49.3% during the peak of summer 2006 and continue declining as time progressed.

As expected, the maximum chlorophyll *a* concentration during Spring in 2007 in the canal scenarios were lower than the status quo and the emerged island scenarios, chlorophyll *a* concentrations were at the range of 250-300 µg/L and appeared to be scattered in the Sea with only central basin had higher Chl *a* concentration up to approximately 350 ug/L.

In the scenario where nutrients in the tributary rivers were reduced by 90% in addition to seawater canals implementation, the results showed drastic decline of PO_4 concentrations starting from March 2006, leading to PO_4 concentrations as low as 0.01 mg/L by August 7, 2007 in the Salton Sea. In addition, unionized ammonia was decreased by 68.3%. The chlorophyll *a* concentration and DO are the products of algal productivity, which is computed by optimization technique in the BLOOM module. The growth and mortality constraints prevent a single algae species be removed within a single timestep and maximize the total net growth. Therefore, simulations showed that chlorophyll *a* and DO concentrations were almost identical compared to that in the canals implementation without treated inflows.

Finally, the seawater import/export scenario showed a rather promising results for salinity reduction. The simulation showed that it would take two years for salinity to drop from 46 ppt to 38-39 ppt, which is consistent with the mass balance calculation that estimated salinity would start to stabilize at 38 ppt in 2.47 years.

5.2 Future directions

The calibration and validation for the FLOW/WAVE modules were based on two less than two months of field measurements taken in 1999 and 2005, respectively from two previous studies conducted by Cook (2000) and Chung et al. (2009). The WAQ module were calibrated/validated using the dataset collected quarterly by the Bureau of Reclamation. The model could be tailored to current hydrodynamic conditions should there be current monitoring campaign for critical parameters such as wave height, current velocity. It has been established that sediment adsorption is critical to orthophosphate internal loading in the water column. Therefore, a more intensive, long-term monitoring program (monthly or bi-weekly) in the tributary rivers and at every 1-2 m depth for north, center and south basins in the Sea would help estimate the orthophosphate load in the sediments of the Sea more precisely, thereby producing more reliable results for long-term nutrient reduction simulation.

The two-year simulation timeframe carried out in this study is also the longest water quality simulation of the Salton Sea existed so far. While FLOW module is capable of resolving water level decline due to high evaporation rate in the Salton Sea, the WAQ module would tend to overestimate the water quality variables due to the water loss by evaporation. The issue could be solved by excluding non-local sink term

of evaporation in the continuity equation. Nonetheless, this highlights the limitation of WAQ module on handling fast decline water level in aquatic system like the Salton Sea. In addition, the maximum threshold for salinity calculation in FLOW is 50 ppt. As the results, in order to run simulation on current Salton Sea (74.25 ppt as of January 2020) an equation of state for hypersaline water needs to be integrated into existing Deflt3D-FLOW to accurately characterize the spatial-temporal changes in density structure that affect temperature and salinity simulation directly.

In this work the sediment-water interaction is modelled by the simplified S1/S2 approach, where the sediment layers are subject to resuspension, burial and digging processes of the settled substances that are mineralized. Since the sediment layers share the same computational grid for the overlying water, mineralization that takes place in the sediment layers would lead to instantaneous oxygen consumption in the entire water column. Future work should consider using D-Water Quality software with extended functionalities that allow users to create a separate computational grid for the active sediment layer. In addition, having a “deep” sediment boundary layer allows a more comprehensive simulation of sediment diagenesis that involved redox reactions of sulphate, dissolved sulphide, particulate sulphide, apatite-phosphate, vivianite-phosphate, methane as the processes primarily formed in deeper sediment layers and exchange among sediment layers by means of bioturbation.

References

Amorocho, J., and DeVries J.J. 1980. “A New Evaluation of the Wind Stress Coefficient over Water Surfaces.” *J.Geophys.Res.* 85(C1): 433–42.

Anderson, M.A., L. Whiteaker, E. Wakefield, and C. Amrhein. 2008. “Properties and Distribution of Sediment in the Salton Sea , California : An Assessment of Predictive Models.” *Hydrobiologia* 694: 97–110.

Barnum, Douglas A. et al. 2017. “State of the Salton Sea : A Science and Monitoring Meeting of Scientists for the Salton Sea.” *USGS-Science for a changing world*: 1–22.

Byron, Earl R, and Harry M Ohlendorf. 2007. “Diffusive Flux of Selenium between Lake Sediment and Overlying Water: Assessing Restoration Alternatives for the Salton Sea.” *Lake And Reservoir Management* 23(5): 630–36.

California Department of Public Health. “California Breathing.” https://www.cdph.ca.gov/Programs/CCDPHP/DEODC/EHIB/CPE/Pages/CaliforniaBreathingCountyAsthmaProfiles.aspx.

California Department of Water Resources. 2013. *Salton Sea Species Conservation Habitat Project- Final Environmental Impact Statement/Environmental Impact Report*. Santa Barbara.

Chung, Eu Gene, A Bombardelli, and S Geoffrey Schladow. 2009a. “Sediment Resuspension in a Shallow Lake.” *Water Resources Research* 45(January): 1–18.

Chung, Eu Gene, Fabián A Bombardelli, and S Geoffrey Schladow. 2009b. “Modeling Linkages between Sediment Resuspension and Water Quality in a Shallow , Eutrophic , Wind-Exposed Lake.” *Ecological Modelling* 220: 1251–65.

Chung, Eu Gene, S. Geoffrey Schladow, Joaquim Perez-Losada, and Dale M. Robertson. 2008. “A Linked Hydrodynamic and Water Quality Model for the Salton Sea.” *Hydrobiologia* (604).

Cohn, Jeffrey P. 2000. “Saving the Salton Sea.” *BioScience* 50(4): 295. http://www.jstor.org/stable/1313703.

Cook, Christopher B., Gerald T. Orlob, and David W. Huston. 2002. “Simulation of Wind-Driven Circulation in the Salton Sea: Implications for Indigenous Ecosystems.” *Hydrobiologia* 473: 59–75.

Cook, Christopher Bruce. 2000. “Internal Dynamics of a Terminal Basin Lake : A Numerical Model for Management of the Salton Sea.”

Deltares. 2014a. “D-Water Qaulity: Process Library Description-Technical Reference Manual.”

Deltares. 2014b. “Delft3D-FLOW User Manual: Simulation of Multi-Dimensional Hydrodynamic Flows and Transport Phenomena,Including Sediments.”

Deltares. 2019. “Delft3D-WAVE User Manual: Simulation of Short-Crested Wave with SWAN.”

Dissanayake, Pushpa, Hilmar Hofmann, and Frank Peeters. 2019. “Comparison of Results from Two 3D Hydrodynamic Models with Field Data: Internal Seiches and Horizontal Currents.” *Inland Waters* 9(2): 239–60. https://doi.org/10.1080/20442041.2019.1580079.

Frie, Alexander L., Justin H. Dingle, Samantha C. Ying, and Roya Bahreini. 2017. “The Effect of a Receding Saline Lake (The Salton Sea) on Airborne Particulate Matter Composition.” *Environmental Science & Technology*.

Friend, M. 2002. “Avian Disease at the Salton Sea.” *Hydrobiologia* 473(1–3): 293–306.

Garcia, M.H., and G. Parker. 1991. “Entrainment of Bed Sediment into Suspension.” *J.Hydraul.Eng.* 117: 414–35.

Garcia, M, and G Parker. 1993. “Experiments On the Entrainment OF Sediment into Suspension by a Dense Bottom Current.” *Journal Of Geophysical Research-Oceans* 98(C3): 4793–4807.

Glenn, Edward P, Michael J Cohen, Jason I Morrison, and Carlos Valde. 1999. “Science and Policy Dilemmas in the Management of Agricultural Waste Waters: The Case of the Salton Sea, CA, USA.” 2: 413–23.

Gowland, J.E. et al. 2007. “Organic-Rich Fine Sediments in Florida.Part II.Resuspension in a Lake.”

Hawley, N., and B.M. Lesht. 1992. “Sediment Resuspension in Lake St-Clair.” *Limnol. Oceanogr.* 37: 1720–37.

Holdren, G Chris, and Andrew Montaño. 2002. “Chemical and Physical Characteristics of the Salton Sea , California.” *Hydrobiologia* (473): 1–21.

Huston, D.W. 2000. “Application of a Wind Field Analysis to a Three-Dimensional Hydrodynamic Model of the Salton Sea, California.” University of Calif., Davis.

Imperial Irrigation District. 2015. “Draft-Salton Sea Restoration and Renewable Energy Initiative Framework.”

Kaçikoç, Meltem, and Mehmet Beyhan. 2014. “Hydrodynamic and Water Quality Modeling of Lake Eğirdir.” *Clean - Soil, Air, Water* 42(11): 1573–82.

Li, Zhijie, Qiuwen Chen, and Qiang Xu. 2015. “Modeling Algae Dynamics in Meiliang Bay of Taihu Lake and Parameter Sensitivity Analysis.” *Journal of Hydro-Environment Research* 9(2): 216–25. http://dx.doi.org/10.1016/j.jher.2014.10.001.

Little Hoover Commission. 2015. “Averting Disaster: Action Now for the Salton Sea.” (228): 1–52. http://www.lhc.ca.gov/studies/228/Report228.pdf.

Lorey, David E. 2002. *Global Environmental Challenges of the Twenty-First Century: Resources, Consumption, and Sustainable Solutions*. Rowman & Littlefield Publishers.

Marti-cardona, Belen, T.E. Steissberg, S Geoffrey Schladow, and S.J. Hook. 2008. “Relating Fish Kills to Upwellings and Wind Patterns in the Salton Sea Relating Fish Kills to Upwellings and Wind Patterns in the Salton Sea.” *Hydrobiologia* 604: 85–95.

McCombs, Matthew P., Ryan P. Mulligan, Leon Boegman, and Yerubandi R. Rao. 2014. “Modeling Surface Waves and Wind-Driven Circulation in Eastern Lake Ontario during Winter Storms.” *Journal of Great Lakes Research* 40(S3): 130–42. http://dx.doi.org/10.1016/j.jglr.2014.02.009.

Mei, C.C., S.J. Fan, and K.R. Jin. 1997. “Resuspension and Transport of Fine Sediments by Waves.” *J.Geophys.Res.-Oceans* 102: 15807–21.

Mian, M.H., and E.K. Yanful. 2004. “Analysis of Wind-Driven Resuspension of Metal Mine Sludge in Tailings Pond.” *J.Environ. Eng. Sci* 3: 119–35.

Parker, G. 2004. “1D Sediment Transport Morphodynamics with Applications to Rivers and Turbidity Currents.” *Natl.Cent. for Earth Surf.Dyn.*

Parker, G., C.M. Toro-Escobar, M.A. Ramey, and S. Beck. 2003. “The Effect of Floodwater Extraction on the Morphology of Mountain Streams.” *J.Hydraul.Eng.* 129: 885–95.

Redlands Institue. 2002. *Salton Sea Atlas*. Esri Press.

Rueda, Francisco, Javier Vidal, and Geoffrey Schladow. 2009. “Modeling the Effect of Size Reduction on the Stratification of a Large Wind-Driven Lake Using an Uncertainty-Based Approach.” *Water Resources Research* 45.

Salton Sea Authority. 2016. *Salton Sea Funding and Feasibility Action Plan Benchmark 7: Project Summary*. http://saltonseaauthority.org/wp-content/uploads/2017/02/SS-Benchmark-7_5-11-16r.pdf.

Sanford, L.P., and J.P. Halka. 1993. “Assessing the Paradigm of Mutually Exclusive Erosion and Deposition of Mud, with Examples from Upper Chesapeak Bay.” *Mar.Geol.* 114: 37–57.

Sanford, L.P., and J.P.Y. Maa. 2001. “A Unified Erosion Formulation for Fine Sediments.” *Mar.Geol.* 179: 9–23.

Schroeder, R.A., W.H. Orem, and Y.K. Kharaka. 2002. “Chemical Evolution of the Salton Sea, California: Nutrient and Selenium Dynamics.” *Hydrobiologia* 473(1): 23–45. https://doi.org/10.1023/A:1016557012305.

Shields, A.F. 1936. “Anwendung Der Aehnlichkeitsmechanik Und Der Turbulenzforschung Auf Die Geschiebebewegung.” Mitt. Preuss Ver. Anst.(Application of similarity principles and turbulence research to bed-load movement, translation by W.P.Ott and J.C. van Uchelen, Publ. 167, Hydrodyn. Lab.,Calif. Inst. of Technol.,Pasadena, Calif.,1939.).

Singer, Eugene. “Ancient Lake Cahuilla.” http://www.sci.sdsu.edu/salton/AncientLakeCahuilla.html.

Somlyody, L. 1986. “Wind Induced Sediment Resuspension in Shallow Lakes.” *Water Qaulity Modelling in the Inland Natural Environment. BHRA, The Fluid Engineering Centre*: 287–98.

Tayor, P. A., and R.J. Lee. 1984. “Simple Guidelines of Estimating Wind Speed Variation Due to Small Scale Topographic Features.” *Climatol.Bull.* 18(2): 3–32.

Vogl, R.A., S.C. Beadle, R.N. Henry, and D.S. Lipton. 1999. *Environmental Reconnaissance of the Salton Sea: Sediment Contaminants Riverside and Imperial Counties, California*.

Vogl, Richard A, and Ryan N Henry. 2002. “Characteristics and Contaminants of the Salton Sea Sediments.” *Hydrobiologia* 473: 47–54.

Wahl, Bernd, and Frank Peeters. 2014. “Effect of Climatic Changes on Stratification and Deep-Water Renewal in Lake Constance Assessed by Sensitivity Studies with a 3D Hydrodynamic Model.” *Limnology and Oceanography* 59(3): 1035–52.

Watts, James M., Swan, Brandon K., Tiffany Mary Ann, Hurlbert Stuart H. 2001. “Thermal, Mixing, and Oxygen Regimes of the Salton Sea, California, 1997-1999.Pdf.” *Hydrobiologia* 466: 159–76.

Xu, Elvis Genbo, Cindy Bui, Cassandra Lamerdin, and Daniel Schlenk. 2016. “Spatial and Temporal Assessment of Environmental Contaminants in Water, Sediments and Fish of the Salton Sea and Its Two Primary Tributaries, California, USA, from 2002 to 2012.” *Science of the Total Environment*.